NASA
Technical
Paper
2855

December 1988

Aerodynamic Pressures and Heating Rates on Surfaces Between Split Elevons at Mach 6.6

L. Roane Hunt

NASA

NASA
Technical
Paper
2855

1988

Aerodynamic Pressures and Heating Rates on Surfaces Between Split Elevons at Mach 6.6

L. Roane Hunt
Langley Research Center
Hampton, Virginia

National Aeronautics
and Space Administration

**Scientific and Technical
Information Division**

Summary

An aerothermal study was performed in the Langley 8-Foot High-Temperature Tunnel at a Mach number of 6.6 to define the pressures and heating rates on the surfaces between split elevons similar to those used on the Space Shuttle. A 1/3-scale model representing the Shuttle wing-elevon junction was extensively instrumented to measure the detailed pressure and heating-rate distributions within the chordwise gap between elevons and on the windward surfaces of the wing and elevons. Tests were performed with both laminar and turbulent boundary layers on the wing surface upstream of the elevons. The flow in the chordwise gap between the elevons was characterized by flow separation at the gap entrance and flow reattachment at a depth inversely proportional to the gap width. The gap pressure and heating rate increased significantly with a decrease in elevon gap width, and maximum gap heating rate was proportional to the maximum gap pressure. Correlation of the present results indicates that the gap heating was directly proportional to the elevon windward surface pressure and was not dependent upon whether the boundary layer on the windward elevon surface was laminar or turbulent.

Introduction

Maneuverable reentry vehicles, such as the Space Shuttle, require wing-elevon control surfaces that can tolerate the severe aerothermal loads of hypersonic flight. The Space Shuttle has split elevons on each wing as described in reference 1. The flow environment over the elevons is not amenable to analytical prediction because of the inherent complexity produced by variable-deflection angles, shock interactions, flow leakage past hinge-cove seals, and crossflow around lateral edges of the elevons. Thus far, the efforts by computational fluid analysts have not produced a flow model to handle the complex flow field entering and passing through the gap between elevons. For convenience, the primary design and correlation approach has been to relate gap heating to elevon windward-surface heating; however, for this approach, an unreasonable link is assumed between the boundary layers of the two surfaces because a new boundary layer is formed on the elevon sidewalls. The simplest flow model for the present problem is channel flow between the elevons with entrance conditions derived from local flow on the elevon windward surface. For either the case of a simple channel flow model or a more complex computational flow model, experimental and flight data are required to validate the analysis.

The split elevons of the Shuttle are separated by a stub which serves as a structural fairing and an end seal for the hinge cove. An early design included narrow chordwise gaps between the stub and each elevon, and the heating within these gaps was of great concern. The stub design was eventually changed to eliminate these gaps; however, an experimental study (ref. 2) indicated that the magnitude of the heating in these gaps was benign. As a result of the new stub design, the greatest concern was the heat load within the larger chordwise gap between the elevons. Based on the assumption that elevon sidewall heating would be about equal to elevon windward-surface heating, the original design used the Shuttle silica-tile thermal protection system in the gap. However, late in the fabrication process, thermal analysis based on small-scale, laminar-flow test results indicated that the area between the elevons would encounter temperatures of 3660°R (ref. 3); these temperatures were too great for the tiles to survive. This analysis used laminar data that indicated that sidewall heating could be as high as 1.36 times the windward-surface heating and extrapolated these results to include the turbulent portion of the trajectory in predicting temperatures above the design. Contrary to this conclusion, results from reference 2 indicated a corresponding heating ratio of about 0.36 for the turbulent condition. Conservatism led to installation of an ablative material on the elevon sidewalls, which was replaced after each of the first five flights. An assessment of the results of the first four flights revealed that the aerothermal environment between the elevons was less severe than the conservative estimate; therefore, the original tile design was installed on one elevon sidewall (including instrumented tiles) for flight five. Since the elevon sidewall temperatures of flight five (ref. 4) were less than the tile design limit, the original tile design was reinstated for subsequent flights and the results were good except for localized damage that was probably due to gap-filler and tile irregularities. (See ref. 3.)

Although the original tile design has survived each flight with only localized damage, the actual flow between the elevons is not known adequately to assess this damage or to improve the design. Therefore, the test model of reference 2 was modified to approximate a 1/3-scale model of the full elevon at the stub and to include sufficient instrumentation to provide detailed heating distributions on the elevon sidewalls. The elevon chordwise length was 24 in., and the gap width between elevons was varied from 1 to 3 in. The windward longitudinal edge of the elevons adjacent to the gap was replaceable to provide variation in edge radius along the

chordwise-gap entrance. Tests were performed in the Langley 8-Foot High-Temperature Tunnel with both laminar and turbulent boundary layers on the wing section ahead of the elevons. These tests were made at a Mach number of 6.6, a unit Reynolds number range from 0.37×10^6 to 1.46×10^6, and a total temperature of about 3500°R. The model wing angle of attack was varied from 0° to 10°, and the elevon deflection angles were varied from 0° to 20°. This paper presents the detailed pressure and heating distributions on the windward surfaces of the wind and elevon and on the elevon sidewalls for the various test conditions and geometry variations. Also, limited correlations of maximum elevon sidewall heating rate with windward elevon pressure are presented.

Symbols

c_p	specific heat at constant pressure, Btu/lbm-°R
L	elevon chord length, in. (fig. 1(c))
M	Mach number
N_{Pr}	Prandtl number
N_{Re}	Reynolds number based on characteristic distance x from leading edge
N_{Ru}	unit Reynolds number, per foot
N_{St}	Stanton number
p	pressure, psia
q	dynamic presure, psi
$\dot{q}$	heat transfer rate, Btu/ft^2-sec
R	windward longitudinal edge radius of elevons adjacent to chordwise gap, in.
T	temperature, °R
t	time, sec
V	velocity, ft/sec
W	stub width, in. (fig. 1(a))
x, y, z	Cartesian coordinates, in. (fig. 1(a))
x', y', z'	Cartesian coordinate system for lower and upper elevons (figs. 3(b) and 3(c), respectively)
α	wing angle of attack, deg (fig. 1(a))
γ	ratio of specific heats
δ	elevon deflection angle, deg (fig. 1(a)); velocity boundary-layer thickness, in.
μ	absolute viscosity, lbm/ft-sec
ρ	density, lbm/ft^3

Subscripts:

aw	adiabatic wall
c	combustor
e	boundary-layer edge
L	windward elevon surface
ℓ	lower elevon
max	maximum in elevon chordwise gap
t	total
u	upper elevon
W	wing surface
w	wall
∞	test-chamber free stream

Superscript:

*	Eckert's reference temperature

Abbreviations:

BL	boundary-layer rake (table I)
PB	elevon leeside and base pressure (table I)
PL	lower elevon windward pressure (table I)
PLS	lower elevon sidewall pressure (table I)
PS	static pressure (table V)
PT	pitot pressure (table V)
PU	upper elevon windward pressure (table I)
PUS	upper elevon sidewall pressure (table I)
PW	wing windward pressure (table I)
QL	lower elevon windward heating rate (table II)

QLS	lower elevon sidewall heating rate (table II)
QU	upper elevon windward heating rate (table II)
QUS	upper elevon sidewall heating rate (table II)
QW	wing windward heating rate (table II)

Apparatus and Tests

Model

The wing-elevon model shown in figure 1 was tested in the Langley 8-Foot High-Temperature Tunnel (8′ HTT). The model consisted of a wing section and two elevons separated by a stub. The wing windward surface was flat and the leeward surface was curved in a circular arc. Two solid brass leading edges were used: one was blunt with a radius of 0.38 in. to obtain a laminar boundary layer, and the other was sharp with flow trips to obtain a turbulent boundary layer. The flow trips consisted of a row of 0.19-in-diameter spheres spaced 0.75 in. apart and located 5 in. from the leading edge like those described in reference 5. The rest of the model was fabricated with 0.5-in-thick steel walls to provide structural strength and heat-sink characteristics to ensure that thermal distortions would not occur during the 10-sec aerothermal exposures. The wing section was 52 in. wide, and the length from the leading edge to the elevon hinge was 79 in. The total width of the elevon section between elevon fences was 39 in., and the elevon fences extended 19 in. forward of the hinge axis. The elevons were designed to fit three different stub widths of 1 in., 2 in., and 3 in. by adding appropriate shim plates between the elevons and elevon fences when the thinner stubs were used. The upper and lower elevons were 18 in. wide and 24 in. from the hinge axis to the trailing edge. The hinge axis was located 3 in. below the wing windward surface. (See fig. 1(c).) The elevon chordwise cross section was tapered to approximate the Shuttle elevons. The windward surface of the elevons was flat and was aligned with the wing at zero deflection angle, and the leeward surface was tapered 17.5° to a trailing-edge thickness of 1.7 in. With the 2-in. stub installed, the elevon configuration was approximately a 1/3-scale model of the Shuttle elevon configuration.

Photographs of the model installed in the wind tunnel are presented in figure 2. The model was mounted vertically on the center diamond-shaped support, on which it was rotated to a predetermined angle of attack and fixed before each run. The upper elevon is removed in figure 2(b) to show the hinge-section interior. The stub and elevon shim adjustments were made with the elevons removed. The hinge-section interior was sealed from the external flow with a tight metal-to-metal fit at the ends of the elevon and with silicone rubber seals between the elevon and the windward and leeward wing surfaces. The elevons were rotated individually and bolted to their respective fences at the predetermined test angles. More of the elevon and stub details are visible in figure 2(c), such as the 3-in. stub radius about the hinge axis and the replaceable edge strip along the elevon chordwise gap, which provides two edge radii of 0.0 and 0.25 in.

Instrumentation

The model was instrumented to determine the detailed pressure and heating-rate distributions on the elevon sidewalls that form the chordwise gap between the elevons and on the windward wing and elevon surfaces. A total of 29 pressure orifices and 77 Gardon heat-flux gages were installed on the model surfaces. The geometric coordinates of each instrument location are presented in tables I and II. The two Cartesian coordinate systems used in tables I and II are illustrated in figure 1 for the overall model (unprimed coordinates) and in figure 3 for the elevons (primed coordinates). The unprimed coordinates (fig. 1(a)) originate at the wing leading edge, the flat windward surface of the wing, and the horizontal centerline through the chordwise gap between elevons. The unprimed coordinates for the elevon instruments are based on a fixed elevon gap width W of 2 in. and an elevon deflection angle of 0°. The windward wing and elevon instrumentation, selected for longitudinal plots to be used later, are shown in figure 3(a) and include the wing centerline and the midspan of each elevon. The primed coordinates for the lower and upper elevons are illustrated in figures 3(b) and 3(c), respectively. The primed coordinates originate at the elevon hinge axis, the elevon windward surfaces, and the gap edge with y' positive away from the horizontal centerline for each elevon. As shown in figure 3(b), the lower elevon was densely instrumented on the windward and sidewall surfaces with pressure orifices and heat-flux gages. Thirty-five heat-flux gages were located on the sidewall, primarily in rows normal to the windward surface at the same values of x' as the gages on the windward surface. Minimal pressure orifices and heat gages were located on the upper elevon, as shown in figure 3(c). Elevon pressures were measured on the leeward surfaces and trailing-edge base surfaces of both elevons.

The surface-pressure orifices were installed using stainless-steel tubes mounted through the model wall and flush with the outer surface. The tubes, 2 to 4 ft long and 0.060 in. in diameter, were attached to individual electromechanical pressure transducers located inside the elevons and the wing section of the model. The Gardon heat-flux gages were the heat-sink type with a 0.005-in-thick chromel disk mounted flush with the model surface and bonded to a nickel body. The gage body was threaded and installed in the thick model walls as shown in figure 4(a). The gaps around the disks were minimized by the close fit between the gage shaft and the installation hole. Any surface recesses around the disk were filled with a ceramic compound to provide a flush surface installation.

Boundary-layer instrumentation consisted of two fixed survey-rake locations ahead of the upper elevon as shown in figure 3(c). The pitot-pressure tubes were 72 in. from the wing leading edge, and the spanwise locations were 2 in. and 15 in. from the model centerline. The installation details of the boundary-layer rake are presented in figure 4(b). The rake consisted of 14 pitot-pressure tubes and one static-pressure orifice 0.992 in. above the wing surface on the sidewall of the rake. The heights of the pitot tubes above the surface ranged up to 2.5 in. as indicated in the figure. The rakes were used to characterize the boundary layer ahead of the elevons for each test condition.

Facility

The Langley 8-Foot High-Temperature Tunnel (8′ HTT), shown schematically in figure 5, is a large blowdown tunnel that simulates aerodynamic heating and pressure loading for a nominal Mach number of 7 at altitudes between 80 000 and 120 000 ft. The high energy needed for temperature simulation is obtained by burning a mixture of methane and air under pressure in the combustor and expanding the products of combustion through a conical-contoured nozzle into the open-jet test chamber. The flow enters a supersonic diffuser where it is pumped by an air ejector through a mixing tube and exhausted to the atmosphere through a subsonic diffuser. The tunnel operates at total temperatures from 2400°R to 3600°R, free-stream dynamic pressures from 250 to 1800 psf, and free-stream unit Reynolds numbers from 0.3×10^6 to 2.2×10^6 per foot, and it has a maximum run time of 120 sec.

The model is stored in the pod below the test stream to protect it from adverse tunnel start-up loads. Once the desired flow conditions are established, the model is inserted into the test stream on a hydraulically actuated elevator. Insertion time is typically 1.5 sec. More detailed information about the tunnel can be found in reference 5.

Test Conditions and Procedure

The model was tested with the various elevon geometric configurations listed in table III. Two leading edges were used to obtain laminar and turbulent boundary layers on the wing surface ahead of the elevons. In general, the blunt leading edge provides laminar flow for small angles of attack and low free-stream unit Reynolds numbers, but the blunt-leading-edge bow shock produces an entropy layer in the flow field on the wing surface with a reduced Mach number at the edge of the boundary layer. The entropy layer complicates the comparison of the turbulent flow produced with the sharp leading edge with an attached oblique shock and no entropy layer. Flow trips were used with the sharp leading edge to ensure an even transition across the wing to a turbulent boundary layer. For each leading-edge condition, the wing angle of attack α (fig. 1) and the elevon deflection angle δ (fig. 1) were varied to characterize the effects on the gap flow between the split elevons. Also, the gap width between the elevons and the elevon corner radius at the gap entrance was varied for $\alpha = 5°$ and $\delta = 10°$. Additional characterizations were made for the sharp leading edge, including a variation in free-stream Reynolds number and a variation of the upper elevon deflection angle while the lower elevon deflection angle was fixed at 10°.

Flow parameters for each test are presented in table IV. In table IV(a), the total temperature and combustor pressure are listed along with selected free-stream flow properties calculated from tunnel surveys and from gas properties presented in reference 6. The model was tested primarily at a nominal total temperature and pressure of 3300°R and 350 psia, respectively, to produce a free-stream Mach number of 6.6 and unit Reynolds number of 0.37×10^6 per foot. Tests 22, 23, and 24 were made at off-nominal conditions with increased combustor pressures to provide Reynolds numbers of 0.588×10^6, 0.866×10^6, and 1.46×10^6 per foot. Since the model temperature was maintained at the ambient condition prior to model insertion into the test stream, the ratio of wall temperature to total temperature was about 0.16 for this study. Pertinent calculated wing and elevon surface flow conditions are listed in tables IV(b) and IV(c), respectively, including calculated surface pressures and aerodynamic heating parameters. The wing and elevon surface pressures were determined from oblique shock relationships (ref. 7) and from the local ratio of

specific heats γ for the combustion-products test medium (ref. 6).

Data Reduction and Analysis

Model pressures, heating rates, and tunnel data were recorded on magnetic tape at a rate of 20 samples per sec using the on-site 8′ HTT computer. The magnetic tapes were then sent to the Langley Central Digital Data Recording Subsystem for processing of the information to engineering units. Model pressure values were selected from the pressure histories after steady pressures were established on the surface and in the orifice tubes connecting the transducers. The pressure gages and the data recording system have been shown to operate with an error of less than 0.25 percent of full-scale range. The actual absolute error when the gage is operating at the bottom of its scale can be intolerable unless the output is adjusted for the lower range pressures. This was conveniently done in the present test by adjusting all model gages, prior to model injection when all pressure orifices are subjected to the same low pressure, to match a reference precision gage in the test chamber outside the flow adjacent to the model. As a result, the error is limited to the effects of gage nonlinearity for the range between the reference and test pressures, and the maximum absolute error is less than 0.5 percent. The same approach was used with the boundary-layer probes; both static- and pitot-pressure measurements, with their respective errors, produce a possible error in Mach number of less than 1.5 percent.

The heating rates were selected from the data after the model reached the centerline of the tunnel at the same time the pressure measurements were selected. The model-surface temperature rise was negligible, because the model structure was designed with large heat-sink capacity. Since the temperature rise was less than 50°R and the local adiabatic wall temperature was over 3000°R, the heating rates were not corrected for surface temperature rise. The heat-sink Gardon gage has proven to be durable and consistent in its signal repeatability for the severe aerothermal environment of the 8′ HTT. The gage body was threaded, as shown in figure 4(a), for installation adjustment flush with the outer surface of the model. However, the outer 0.125 in. of the gage was machined down to 0.248 in. in diameter for a close fit with the instrument hole in the model outer surface. Also, any recesses around the gage penetrations were filled with ceramic material to obtain a flush surface installation. The primary source of Gardon gage error is in the calibration method. The gage calibration difficulties are inherent because the calibration facility uses a radiant heat source which is subject to errors in the reference gage and to possible inconsistencies in the special surface coatings used to regulate radiant absorptivity. These gages, which have multiple calibration histories, have been analyzed, and the total error band based on the calibration repeatability was ±7 percent. This is within the scatter range of the present data, and the best indication of the overall accuracy of these Gardon gages is from the wing heating rates of the present study, where the flow is known to be either laminar or turbulent.

The experimental heating-rate data of this study are converted to Stanton number based on the free-stream flow conditions given in table IV(a). Stanton number is defined by the following expression:

$$N_{\mathrm{St},\infty} = \dot{q}/(T_t - T_w)(\rho V c)_\infty \tag{1}$$

where T_t and $(\rho V c)_\infty$ are given in table IV(a). The theoretical flat-plate heating rates were obtained from the following equations in reference 8 for laminar and turbulent boundary layers:

$$N^*_{\mathrm{St}} = (0.332)(N^*_{\mathrm{Pr}})^{-2/3}(N^*_{\mathrm{Re}})^{-1/2} \tag{2}$$

$$N^*_{\mathrm{St}} = (0.030)(N^*_{\mathrm{Pr}})^{-2/5}(N^*_{\mathrm{Re}})^{-1/5} \tag{3}$$

The asterisk signifies that the gas properties were evaluated at Eckert's reference temperature T^* where

$$T^* = (0.22)T_{aw} + (0.28)T_e + (0.50)T_w \tag{4}$$

The adiabatic wall temperature T_{aw} is calculated with the following equation:

$$T_{\mathrm{aw}} = T_e + (T_t - T_e)(N^*_{\mathrm{Pr}})^r \tag{5}$$

where r is 1/2 or 1/3 for laminar or turbulent boundary-layer flow, respectively. For these relationships, the surface heating rate is related to the reference-temperature Stanton numbers by the equation

$$N^*_{\mathrm{St}} = \dot{q}/(T_{aw} - T_w)(\rho V c)^* \tag{6}$$

Values for T_{aw}, T^*, and $(\rho V c)^*$ based on calculated local pressures for the wing and elevon surfaces are given in tables IV(b) and IV(c), respectively. Also, the unit Reynolds number $(\rho V/\mu)^*$ listed in these tables was used to calculate local N^*_{Re} values as follows:

$$N^*_{\mathrm{Re}} = (\rho V/\mu)^* x \tag{7}$$

These relationships were used to compare the present experimental results with analytical predictions.

The boundary-layer Mach number profiles were obtained from the measured pitot and static pressures from the fixed rakes upstream of the elevon gap. The Mach number was calculated from the ratio of static pressure to pitot pressure using the Rayleigh pitot formula (ref. 7) and assuming an inviscid, calorically perfect gas. The analytical procedures for the present study were the same as those used in reference 9 which were applied to a similar configuration on a flat plate with the same two leading-edge conditions. In reference 10, the boundary-layer code from reference 11 predicted the laminar and turbulent Mach number profile for the blunt leading edge, but the code underpredicted the turbulent boundary-layer thickness for the sharp leading edge. The deviation of the predicted boundary-layer thickness from the experimental results increased with distance from the leading edge of the model. (See ref. 9.) Therefore, for the present test, the more difficult boundary-layer condition of the blunt-leading-edge configuration was predicted using reference 11, and the turbulent boundary layer for the sharp leading edge was predicted by the procedures presented in reference 9. The turbulent boundary-layer thickness was determined by the empirical relation (from ref. 12)

$$\delta/x \approx 0.37 N_{\mathrm{Re}}^{-1/5} \tag{8}$$

The predicted turbulent Mach number profile was obtained using the classical 1/7-power-law flat-plate velocity profile given as

$$\frac{V}{V_e} = \left(\frac{z}{\delta}\right)^{1/7} \tag{9}$$

in reference 13, and the Crocco relationship between velocity and temperature is expressed as

$$\frac{V}{V_e} = \frac{T_t - T_w}{T_{t,e} - T_w} \tag{10}$$

in reference 14. From equations (9) and (10) and from basic isentropic relationships, the Mach number can then be calculated using the expression

$$M = \left[\frac{\lambda M_e^2}{\left(1 + \frac{\gamma - 1}{2} M_e^2\right) - \left(\lambda \frac{\gamma - 1}{2} M_e^2\right)}\right]^{1/2} \tag{11}$$

where

$$\lambda = \frac{(z/\delta)^{2/7}}{T_t/T_{t,e}} \tag{12}$$

The total temperature variation in the boundary layer is expressed in terms of known variables as

$$\frac{T_t}{T_{t,e}} = \left(\frac{z}{\delta}\right)^{1/7} \left(1 - \frac{T_w}{T_{t,e}}\right) + \frac{T_w}{T_{t,e}} \tag{13}$$

Results and Discussion

The primary focus of the present study is to define sidewall pressure and heating-rate distributions in the chordwise gap between elevons for both laminar and turbulent boundary-layer flow on the windward surfaces of the wing and elevon. Therefore, typical boundary-layer Mach number profiles are presented for one longitudinal wing station just ahead of the elevons to further characterize the external boundary-layer flow conditions. Also, detailed pressure and heating-rate distributions for the windward surfaces of the model are presented to indicate the characteristics of both types of flow. Theoretical predictions of the external flow effects are presented to verify the general flow conditions of the windward surfaces. Next, the elevon gap-pressure and heating-rate distributions are presented for the various wing and elevon angles. Some empirical relationships are then given to suggest what parameters are affecting the gap flow and how the experimental data of the present study might be extrapolated to flight conditions. Finally, limited surface pressure and surface heating-rate comparisons are presented to indicate the effects of the variations of gap width, elevon corner radius, Reynolds number, and differential elevon deflection angles.

The results of this study consist of model pressure and model heating rates. The model surface and boundary-layer rake pressures, listed in table V, are normalized by the free-stream static pressure given in table IV(a). The heating-rate data are presented in table VI as Stanton numbers based on free-stream total temperature and on $(\rho V c)_\infty$ which are also given in table IV(a).

Wing Boundary-Layer Profiles

Mach number profiles obtained from the pitot-pressure rake were used to characterize the boundary-layer flow on the wing section of the model upstream of the elevon gap. The static and pitot pressures are presented in table V. The profile was 72 in. from the leading edge and 7 in. upstream of the elevon hinge axis. The local measured static pressure on the rake was used for the Mach number calculation for all runs except those affected by flow separation upstream of the deflected elevons. The equivalent attached boundary-layer-flow static pressure was used for the calculation when separation occurred.

The experimental profiles presented were obtained from the probe (BL1) located 15 in. from the model centerline, as indicated in table I. Probe BL2, located 2 in. from the centerline, was also used for one test (test 1), and the profiles from the two probes agreed. Probe BL2 was not installed for the remaining tests because its presence, directly upstream of the chordwise gap between the elevons, affected flow in the gap.

Blunt leading edge without flow trips. The experimental Mach number profiles for the blunt-leading-edge flow condition with various wing and elevon angles are presented in figure 6. The present results agree with the laminar boundary-layer predictions of reference 11 and extend beyond the boundary-layer edge into the entropy-gradient region that is produced by the curved bow shock associated with the blunt leading edge. Most of the profiles were not affected by the elevon deflections, since the rake was 7 in. upstream of the elevons. However, the flow separation did affect the profile for $\delta = 20°$ in figure 6(a) with greatly reduced Mach numbers near the wing surface. At $\alpha = 10°$ (fig. 6(c)), the laminar theory did not agree as well with the data because of boundary-layer transition, which was expected for the larger angles of attack. As shown in reference 10, the turbulent Mach number profile is similar to and undistinguishable from the measured entropy-layer profile. Therefore, the onset of transition would cause only slight variations in the profile. Overall, the flow on the wing for $\alpha = 0°$ and 5° produces laminar flow, and significant flow separation occurs only at the larger elevon deflection angles.

Sharp leading edge with flow trips. The corresponding Mach number profiles for the sharp leading edge with flow trips are presented in figure 7 for $\alpha = 0°$, 5°, and 10°. In general, the experimental results were not compared with the turbulent predictions of reference 11 because that approach greatly underpredicts the boundary-layer thickness for the present model (ref. 9). Therefore, the turbulent boundary-layer thickness was predicted using equation (8), and the Mach number profile was predicted using equation (11). For $\alpha = 0°$ (fig. 7(a)), the Mach number profile is fuller than the turbulent prediction, which is consistent with a less developed turbulent or transitional boundary layer. (See ref. 14.) Also, the experimental results fall between the turbulent prediction from equation (11) and laminar predictions of reference 11 to indicate transitional flow. The effort to trip the flow was successful for $\alpha = 5°$ and 10°, where both the boundary-layer thickness and Mach number profile were adequately predicted by equation (11). Also, there was no indication of flow separation resulting from elevon deflections.

Windward-Surface-Pressure and Heating-Rate Distributions

The windward surfaces of the wing and elevon were sufficiently instrumented to characterize the external boundary-layer flow on the wing and elevon. The wing centerline and elevon midspan instrumentation (fig. 3(a)), was selected for longitudinal distribution plots. The experimental pressure and heating-rate distributions are compared with theoretical predictions to establish that data magnitudes and trends are correct. These comparisons also indicate the locations of laminar, transitional, and turbulent flow regions and the locations of flow separation regions. For each longitudinal distribution, corresponding lateral pressure and heating-rate distributions at the elevon midchord location are presented for each test condition.

Blunt leading edge without flow trips. The longitudinal and lateral pressure and heating-rate distributions are presented in figure 8 for the blunt leading-edge conditions at angles of attack of 0°, 5°, and 10° for elevon deflection angles of 0°, 5°, 10°, and 20°. For $\alpha = 0°$ and $\delta = 0°$ (fig. 8(a)), the longitudinal pressure distribution beyond about $x = 31.5$ in. was constant and agreed with the inviscid predictions of the oblique-shock relations given in reference 7. At $x = 13.5$ in., the pressure was significantly higher, and the Blast-Wave Theory of reference 15 predicted the increased pressure caused by the curved bow shock of the blunt leading edge. The pressure increase ahead of the elevon for elevon deflections of 10° and 20° indicates flow separation which was noted previously by the boundary-layer profiles for $\delta = 20°$ (fig. 6(a)). The corresponding elevon pressure also increased above the predicted pressure for no entropy layer and no flow separation.

The corresponding longitudinal heating-rate distribution on the wing agreed with the laminar prediction from equation (2). For $\delta = 10°$, the heating decreased in the separation region consistent with classic laminar-flow separation. However, for $\delta = 20°$, the heating in the separated flow region increased; this increase indicated the same transitional flow behavior observed under similar conditions in reference 16. The heating rate at the trailing edge of the elevon at $\delta = 20°$ increased above the predicted heating for attached flow; this increase is consistent with the pressure data, because the flow is more effectively compressed when separation occurs. The two predicted heating-rate curves for each elevon angle were obtained by assuming two different characteristic lengths with virtual origins at the wing leading

edge ($x = 0$) and at the elevon hinge axis ($x' = 0$). The experimental results should fall between these assumptions, because using x assumes a continuous boundary-layer growth from the wing to the elevon, and using x' assumes a boundary-layer discontinuity at the hinge axis with a new start from a boundary-layer thickness of zero.

Apparently, the results for $\alpha = 0°$ (fig. 8(a)) were further complicated by flow blockage of model free-stream flow interference, which produced increased model base pressures. For the blunt-leading-edge tests, the elevon base pressure (PB79 and PB80 in table V) was significantly higher than that for the sharp-leading-edge tests. For $\alpha = 0°$ with the blunt leading edge, the flow blockage was so severe that the windward elevon surface pressures and heating rates were affected. The longitudinal pressure and heating rate (fig. 8(a)) increased toward the trailing edge of the elevon, and the lateral pressure and heating rate (fig. 8(a)) increased with distance from the elevon gap edge; this increase indicated that a conical compression shock impinged on the outer corners of the elevon trailing edge. Although much of the external flow at $\alpha = 0°$ was laminar, the flow blockage effects on the elevon gap data eliminated this test condition from further comparisons.

Although the elevon base pressure was also elevated for the larger angles of attack, the windward pressure and heating-rate distributions on the elevons did not indicate significant flow blockage effects. For $\alpha = 5°$ (fig. 8(b)), the longitudinal-pressure and heating-rate distributions agreed with inviscid and laminar predictions, respectively; the elevon pressure data and heating-rate data approach the predicted levels for turbulent flow as the elevon deflections increase. For $\delta = 10°$, laminar-flow separation occurred ahead of the elevon, and caused slightly increased pressure and decreased heating. The pressure on the elevon did not increase above the predicted level for inviscid flow. Also, the elevon heating approached the predicted turbulent heating level for $\delta = 10°$. The results for $\alpha = 10°$ (fig. 8(c)) were similar, but flow transition occurred on the wing at about $x = 50$ in., which caused increased heating ahead of the elevon. Flow transition was also indicated in the boundary-layer profile in figure 6(c). The lateral pressure and heating-rate distributions for $\alpha = 5°$ and $\alpha = 10°$ were relatively flat and decreased toward the elevon edge at the chordwise gap.

The longitudinal heating-rate distributions on the wing and elevon with $\delta = 0°$ are correlated in figure 9 in the form of Stanton number and Reynolds number based on Eckert's reference temperature and are compared with the laminar and turbulent theory of equations (2) and (3), respectively. Clearly, the desired laminar flow does not occur at the elevons for α greater than 5°. Also, when the elevons were deflected, transition occurred on the elevon surface. Therefore, the 5° angle-of-attack condition was the best for laminar flow, but laminar flow over the entire model length was achieved only with an elevon deflection angle of 0°.

Sharp leading edge with flow trips. The sharp-leading-edge configuration with flow trips was used to obtain turbulent boundary-layer-flow conditions. The longitudinal and lateral pressure and heating-rate distributions are presented in figure 10 for $\alpha =$ 0°, 5°, and 10° for elevon deflection angles of 0°, 5°, and 10°. The pressure data agreed with the predicted inviscid levels (ref. 7) on the wing and elevons, which indicated negligible flow separation and flow blockage effects. For $\alpha = 0°$ (fig. 10(a)), the flow trips were ineffective in providing fully turbulent flow at the elevons, and transition began at about $x = 43.5$ in. The transitional flow was also indicated in the boundary-layer profile in figure 7(a) discussed previously. Fully turbulent flow was obtained on the wing at $x = 40$ in. and 13 in. for $\alpha = 5°$ and 10°, respectively. (See figs. 10(b) and 10(c).) The experimental heating results for the elevon surfaces for all deflection angles agreed with the predicted levels. Also, the lateral distributions were relatively flat, and there was some decrease near the elevon edge at the chordwise gap.

The longitudinal heating-rate results for the sharp leading edge on the wing and elevon at $\delta = 0°$ are correlated in figure 11 and indicate the relative effectiveness of the flow trips at the various angles of attack. Although both 5° and 10° angles of attack were sufficient to produce turbulent boundary layer at the elevons, $\alpha = 5°$ was chosen because it was consistent with the laminar condition discussed previously. Therefore, all remaining parametric comparisons are made for $\alpha = 5°$ with various elevon deflection angles.

Elevon Gap Pressures and Heating Rates

Blunt leading edge without flow trips. The lateral pressure and heating-rate distributions at the elevon midchord location for both windward and gap surfaces are presented in figure 12 for $\alpha = 5°$. The normalized surface pressures and heating rates are plotted against the distance from the elevon edge y' for the windward surface and against the normal depth into the chordwise gap z' for the elevon sidewall. The pressures are normalized by values from PL49 at $y' = 8.05$ in., and the heating rates are normalized by values from QL49 at $y' = 9.05$ in. The inset illustrates the locations on the windward and

sidewall elevon surfaces included in these comparison plots.

The purpose of this plot (fig. 12) is to characterize the lateral surface pressure and heating-rate distributions around the elevon edge and into the chordwise gap with respect to the windward reference values. The windward-pressure data and corresponding heating-rate data on the elevon were previously presented in figure 8(b). The gap pressures and heating rates typically increased with distance z' into the gap to a maximum and then decreased. The normalization of the gap pressure distributions for the various elevon deflection angles in figure 12 converges at a maximum of about $p/p_L = 0.23$. However, the corresponding normalized heating-rate distributions did not correlate, and the maximum values of $\dot{q}/\dot{q}_L$ decreased from 1.1 to 0.28 with an increase in δ from 0° to 10°. The original intent was to characterize gap flow effects for laminar boundary layers on the windward surfaces of the wing and elevons, but as shown in figure 8(b), the elevon windward flow varied from laminar to turbulent as δ increased from 0° to 10°. For the only laminar case in figure 12, the maximum gap heating was at about the same level as the heating on the elevon windward surface, which was expected in the original Shuttle design. At $\delta = 10°$, where the normalizing value of $\dot{q}_L$ was turbulent, the maximum value of $\dot{q}/\dot{q}_L$ was reduced to the level of previous turbulent results in reference 2.

In figure 13, the normalized gap heating distributions are presented for each of the five chordwise stations as shown on the inset. The gap heating at each station was normalized by the corresponding windward elevon value at the midspan location. Generally, the data trends from $x' = 8$ in. to 20 in. were similar to those shown in figure 12 and indicate the range of an established characteristic gap flow. As indicated in figure 14, the maximum pressures and heating rates generally increased as a function of x'/L. The value of $\dot{q}_{max}/\dot{q}_L$ for the laminar case ($\delta = 0°$) increased to 1.3 near the trailing edge ($x'/L = 0.83$), which agrees with the 1.36 value (discussed previously and taken from ref. 3) from the small-scale laminar tests made prior to the first Shuttle flight.

Sharp leading edge with flow trips. The lateral pressure and heating-rate distributions across the windward elevon surface and into the gap at the midchord location are presented in figure 15. The windward-surface boundary layers were turbulent for all elevon deflection angles as shown in figure 10(b). Pressure and heating-rate trends with z' for the sharp-leading-edge flow condition were similar to those previously discussed for the blunt-leading-edge flow condition. (Compare fig. 15 with fig. 12 for $\delta = 10°$.) In figure 15, the normalized pressures and heating rates at the midchord location for $\delta = 0°$ are greater than those for $\delta = 5°$ and 10°, which have approximately the same values. The increased pressure and heating rate are probably coupled at $\delta = 0°$, but the cause is unknown. Normalized heating-rate distributions at the various elevon stations are presented in figure 16. In the forward portion of the elevon gap, the heating profiles for $\delta = 5°$ and 10° tend to group together; but at $x' = 20$ in., the profiles for $\delta = 0°$ and 10° seem to agree. This variation suggests that the complex flow pattern in the elevon gap was sensitive to elevon deflection angle. Generally, the profiles of figure 16 show increasing gap heating rates with increasing x' toward the elevon trailing edge. Plots of p_{max}/p_L and $\dot{q}_{max}/\dot{q}_L$ as a function of x'/L are presented in figure 17. These trends, increasing gap pressures and heating rates with x'/L, are similar to the blunt-leading-edge results for $\delta = 10°$ in figure 14.

Maximum gap heating correlations. In the previous discussion, the maximum normalized gap heating was shown to vary with the corresponding normalized gap pressure. The maximum gap heating is plotted as a function of maximum pressure in figure 18 for the turbulent test results to show this variation. This plot shows a definite trend, but there is some data scatter, which probably indicates a lack of precision in determining maximum values at the various longitudinal stations because the gap pressure data were limited at some stations to a single value. However, a correlation shows that the maximum gap heating is a logarithmic function of the corresponding gap pressure. The correlation plot in figure 18 is based on the data obtained with the sharp wing leading edge and a gap width of 2 in. Also, the data cover the entire range of δ tested for $\alpha = 5°$ and 10°. The hand curve fit for the results is as follows:

$$\dot{q}_{max}/\dot{q}_L = (p_{max}/p_L)^{0.65} \qquad (14)$$

This correlation is important to the overall understanding of the gap flow but has limited value in predicting aerothermal loads for a given flight condition unless p_{max} can be determined. Actually, a correlation of gap pressure and heating with free-stream parameters is more desirable for predicting flight conditions.

The basic need for a suitable design criteria to predict the aerothermal loads in the chordwise gap between elevons was discussed previously. The original design parameter of $\dot{q}_{max}/\dot{q}_L = 1$ was increased to 1.36, based on small-scale laminar tests of the Shuttle orbiter. The Shuttle elevon thermal protection

system (TPS) was overdesigned when the same value was used for the turbulent flight condition. (See ref. 3.) Because the turbulent test results of reference 2 indicated that $\dot{q}_{max}/\dot{q}_L$ was much less than 1, the present study was designed to compare laminar and turbulent results directly. In the present study, a laminar boundary layer was obtained on the wing, but not on the deflected elevon. Therefore, it was impossible to compare a complete set of laminar external flow data with turbulent flow data; but the laminar-transitional data is compared with the turbulent flow data in figure 19 to provide a limited comparison.

In figure 19(a), the maximum gap heating at the midchord position normalized to the windward-surface elevon heating ($\dot{q}_{max}/\dot{q}_L$) is plotted against the corresponding windward-surface elevon pressure for both blunt and sharp wing leading edges. These comparisons represent laminar-transitional and turbulent cases, respectively. Wing angles of attack of 5° and 10° and all the elevon deflection angles are included for a fixed gap width of 2 in. and sharp elevon edges. The reference values of $\dot{q}_{max}/\dot{q}_L = 1.36$ from the previous laminar studies and the present turbulent level of $\dot{q}_{max}/\dot{q}_L = 0.25$ are given as upper and lower boundaries. In the present correlation, $\dot{q}_{max}$ is related to values of $\dot{q}_L$ and p_L, because these quantities can be calculated for the various flight conditions. As p_L increased, $\dot{q}_{max}/\dot{q}_L$ for both blunt and sharp leading edges converged at the 0.25 level where the local elevon windward-surface flow was known to be turbulent. Thus, the present turbulent level was established for the gap width of 2 in. At the lower elevon pressures, the $\dot{q}_{max}/\dot{q}_L$ values show more scatter; but the laminar-transitional values for the blunt leading edge (circular symbols) approach the indicated reference laminar boundary. In fact, the data point nearest the laminar level corresponded to the test condition closest to laminar flow with the wing angle of attack at 5° and no elevon deflection. (See fig. 8(b).) Although a complete set of laminar data was not obtained, the present data suggest different $\dot{q}_{max}/\dot{q}_L$ Shuttle design values for laminar and turbulent elevon flow. Actually, a more important conclusion is that the maximum gap heating is independent of the external boundary-layer condition.

A similar comparison is presented in figure 19(b) using the same data values, but here the dimensional quantity of $\dot{q}_{max}$ is plotted against p_L. For the fixed gap width, the maximum gap heating was directly proportional to the elevon windward-surface pressure, which is independent of elevon boundary-layer condition. The curve through the sharp-leading-edge data (square symbols) is hand-fitted with a logarithmic slope of 0.8, this slope suggests that there is turbulent gap flow between elevons. Some of the blunt-leading-edge data (circular symbols) were close to the solid curve at pressures above 0.4 psia, but deviated below the curve with decreasing pressure. The logarithmic slope of the blunt-leading-edge data is 1.0, which indicates transitional gap flow. Although the external boundary-layer condition does not directly affect the gap heating, the gap heating is dependent upon whether the gap flow between the elevons is laminar, transitional, or turbulent.

Effects of Chordwise Gap Width and Gap-Entrance-Edge Radius

The previous elevon gap pressure and heating-rate data have been presented only for a gap width W of 2 in. and with sharp gap-entrance edges. Special tests were made with $W = 1$ in. and 3 in. to determine the effect of gap width, and corresponding tests were made at the same gap widths with a cylindrical gap-entrance edge of 0.25-in. radius. The results are presented in figure 20 in similar form to those previously discussed. These results are for the turbulent flow case for α and δ values of 5° and 10°, respectively. The gap width and edge radius variations do not affect the external flow as indicated in the elevon windward-pressure and heating-rate distributions shown in figure 20. However, the gap pressure and heating distributions are significantly affected by the gap width where the pressure and heating near the gap entrance ($z' \approx 0.5$) varied inversely with gap width. Generally, the depths into the gap where the maximum pressure and heating rate occurred varied inversely with the gap width. As the gap width is decreased by a factor of 3 in figure 20(a), the pressure and corresponding heating near the gap entrance increases by a factor of about 4. Similarly, for the entrance-edge radius of 0.25 in., the gap-entrance pressure and heating increased by about a factor of 3. The effect of gap-edge radius on the pressure and heating was small and limited to the gap-entrance region ($z' < 2$ in.). Further comparison of these same tests (fig. 21) shows the gap heating distributions at the five longitudinal stations. The comparison of figures 21(a) and 21(b) again shows only minor differences in gap heating between the sharp and cylindrical edge radii. Overall, the gap width had the more obvious effect on the gap flow characteristics at the various stations and caused the peak heating to occur closer to the gap entrance ($z' = 0$) as the width was decreased.

Normalized maximum gap pressures and heating rates for the various gap widths and the edge radii are presented in figure 22 as a function of the longitudinal distance from the elevon hinge location. This figure summarizes the results from figures 20

and 21, where the gap flow was primarily affected by the gap width. In general, the data trends of figure 22 show clearly that the maximum gap heating increases directly with maximum gap pressure for the entire chordwise gap length for each of the gap widths presented. In fact, the direct relationship between gap pressure and heating is shown by the correlation plot presented in figure 23. Although the gap-flow characteristics varied for the various gap widths, the same correlation curve, from figure 18, fits the data trend. In figure 24, the maximum gap heating variation with gap width for the present study is compared with previous results of reference 2, which had a much smaller range of gap width. The model geometry of reference 2 differed from the present model in that the elevon length was only 18 in. and the elevons were not tapered but had a trailing-edge thickness of 12 in. Another difference was that the model of reference 2 did not have a constant chordwise gap width, because the forward portion of the gap ($x'/L < 0.3$) was 1 in. less than the downstream portion where the reference data were obtained. However, both sets of data at $x'/L = 0.67$ indicate that $\dot{q}_{max}/\dot{q}_L$ varies inversely with the gap width, and the geometric differences in the gap for the two cases did not affect this trend.

Further correlation and application of the present data are dependent upon the hypothetical flow model for the flow between the elevons. The most elementary assumption would be that of channel flow, but for the present configuration, one side of the channel is open and exposed directly to the kinetic energy of the free-stream flow. The questions that need to be addressed for the present study are to what extent did the gap flow behave as channel flow and to what extent was it influenced by the open side. A channel-flow model would assume that a finite mass flow of gases with fixed energy levels enters the channel; the flow would then develop over a definite "entrance length," and would continue as fully developed channel flow between the elevon sidewalls. If channel flow did not exist between elevons, the three-dimensional flow that turns into the gap would simply develop classical boundary layers along each sidewall completely independent of each other. In this regard, the present results give definite evidence of a channel entrance from figure 20, where the gap pressure increased with decreasing gap width; this increase indicates an interdependence of the sidewall pressure on the opposite wall location, and it follows that gap heating increases with gap pressure.

It can be concluded from the present results that the flow between elevons is channel flow to some extent and that the mass flow between elevons is a function of the windward elevon pressure as correlated in figure 19(b). Although this conclusion is important for general understanding, it does not make the correlation or analysis simple. In fact, the channel flow created by the gap between elevons is complicated by additional factors, including an oblique entrance angle that complicates the definition of the entrance parameters. Therefore, any analysis of this problem is made with the assumption that channel flow must define the entrance-flow parameters from a solution of the viscous and inviscid external flow at the forward edge of the elevons. Definition of the entrance-flow parameters continues to be the most difficult part of the analytical solution to the problem.

Effect of Reynolds Number

In the present study, most of the tests were made at the lowest possible Reynolds number for the 8′ HTT. However, three tests were made at graduated levels to provide a range of free-stream unit Reynolds numbers from 0.382×10^6 to 1.46×10^6 per foot. The sharp leading edge with flow trips was used to obtain turbulent boundary layers, and the wing angle of attack and the elevon deflection angle were 5° and 10°, respectively. The Mach number profiles for the various Reynolds numbers are presented in figure 25 with z normalized by the corresponding boundary-layer thickness. The experimental turbulent profiles are correlated with the turbulent theory (eq. (11)) for the entire Reynolds number range. The largest variance of the experimental Mach numbers from the theoretical curve occurs near the surface at values of z/δ less than about 0.2, and this variance is probably caused by flow interference of the flow trips at the wing leading edge. Overall, the comparisons indicate that a turbulent boundary layer is being produced on the wing for the sharp-leading-edge configuration with flow trips and $\alpha = 5°$ for all Reynolds numbers tested.

The pressure and heat-transfer data for the windward surfaces of the wing and elevon are presented in figure 26. The windward pressures, which are normalized to the free-stream pressure, agree with the predicted inviscid wing pressure and level off just above the predicted inviscid level near the trailing edge of the elevon. The corresponding heating data are presented in the form of Stanton number based on reference temperature and the local flow properties at the edge of the boundary layer. As discussed previously, the flow on the forward section of the wing (circular symbols) was transitional for the lowest Reynolds number condition; but the heating for the higher Reynolds number conditions correlated with the turbulent theory for the entire length of the wing surface. The heating data for the

deflected elevon surface are not included, but the heating on the elevon trailing edge agreed with theory as previously shown in figure 10(b).

The lateral pressure and heating-rate distributions across the elevon midchord station and into the chordwise gap are presented in figure 27 for the same unit Reynolds number range. The normalized pressure and heating distributions were similar for all Reynolds numbers; this similarity indicates that there was no appreciable variance from the general flow pattern. For the same tests, the heating distributions into the gap at the five chordwise stations are presented in figure 28. From $x' = 8$ to $x' = 20$, the maximum heating rate occurs at about $z' = 1.5$ in. for the entire range of Reynolds numbers tested, and the overall gap-flow pattern for the entire length is similar.

Some gap-pressure variation did occur at $z' \approx 0.5$ in figure 27 where the gap pressure was inversely proportional to Reynolds number. Apparently, the gap pressure was influenced by a corresponding variation in the base pressure of the elevon trailing edge. The measured elevon base pressure, designated PB79, is presented in table V, and the corresponding $PB79/p_L$ levels are indicated in the figure at $y' = 0$ and $z' = 0$. The value of $PB79/p_L$ also varied inversely with Reynolds number. This influence of the base pressure on the elevon sidewall pressure at $z' \approx 0.5$ in. indicates that there was a region of flow separation at the gap entrance along the forward edge of the elevons. This influence also indicates that the line of maximum pressure and heating rate at about $z' = 1.5$ in. in figure 28 was the flow reattachment line beyond the flow separation region. Generally, the separation region decreased with gap width as shown in figures 20 and 21, where the maximum pressure and heating rates associated with flow reattachment occurred near the gap entrance ($z' \approx 0$) for $W = 1$ in. Although the magnitude of the pressure in the separation region was affected by variation in base pressure of the trailing edge, the gap flow characteristics downstream from the gap entrance were not affected for the range of Reynolds number of the present study.

Effect of Differential Elevon Angles

Two tests were made at the baseline turbulent condition with the elevons deflected at different angles to provide a limited indication of possible effects of the asymmetric flow on the aerothermal loads in the elevon gap. The longitudinal windward elevon pressure and heating-rate data (fig. 29) was obtained for the tests where the lower elevon was fixed at $\delta = 10°$ and the upper elevon was deflected 0°, 10°, and 20°. The wing angle of attack was 5°, and the width between elevons was 1 in. The windward-pressure and heating-rate data of each elevon agreed with that predicted for each deflection angle. The open symbols indicate the fixed lower elevon data and the solid symbols indicate the corresponding data of the upper elevon at $\delta = 0°$, 10°, and 20°. The elevon pressure for $\delta = 20°$ leveled out at the predicted inviscid pressure, and the heating trend on the elevon agreed with the theory when a new boundary layer formed at the elevon hinge axis ($x' = 0$).

The normalized lateral pressure and heating-rate distributions at the lower elevon midchord locations for both windward and gap sidewall surfaces are presented in figure 30. The pressures and heating rates are normalized with the midspan windward surface values and plotted against the distance from the elevon edge y' and z'. (See fig. 3(b).) As the upper elevon deflection angle was varied from 0° to 20°, the windward pressure and heating of the lower elevon was increased near the edge ($y' \approx 1$ in.) to a maximum of 20° for the upper elevon deflection. This increase in pressure and heating was caused by crossflow from the elevon windward surface with the greater elevon deflection onto that with lesser elevon deflection. When the upper elevon was deflected greater or less than the fixed lower elevon, the gap-pressure and heating-rate distributions were affected in a manner similar to the maximum pressure and heating rates farther into the chordwise gap. The highest gap pressure and heating occurred when the elevon angles were equal, probably because of the greater flow interaction associated with the channel flow between the elevon sidewalls. When the elevon angles were different, the side flow was less dependent of the opposite wall, and the pressure and heating were less severe.

In figure 31, the heating distributions into the gap for each of the five longitudinal locations along the lower elevon are presented. As the upper elevon deflection was varied, the profiles indicate that the complex flow pattern was affected along the entire length of the elevon, but the resulting magnitudes were of the same order as those of the baseline condition for which the elevon deflections were equal. In fact, the maximum gap pressures and heating rates with differential elevon angles presented in figure 32 show the magnitudes to be about equal to or less than those (square symbols) of the equal elevon deflection of 10°.

Concluding Remarks

An aerothermal study was performed in the Langley 8-Foot High-Temperature Tunnel at a Mach number of 6.6 to define the pressures and heating rates on the surfaces between split elevons similar to

those used on the Space Shuttle. The model was a 1/3-scale representation of the Shuttle wing-elevon junction with an elevon chord length of 24 in. and a variable distance between elevons from 1 to 3 in. The model was extensively instrumented to measure the detailed pressure and heating-rate distributions within the chordwise gap between elevons and on the windward surfaces of the wing and elevons. Tests were performed with wing angles of attack of 0° to 10° and elevon deflections of 0° to 20° and with both laminar and turbulent boundary layers on the wing surface upstream of the elevons.

The results of both the laminar and turbulent flow conditions agreed with the theoretical predictions of wing windward-surface pressures, windward-surface heating rates, and boundary-layer profiles. For the laminar case, boundary-layer transition occurred on the deflected elevon surface and flow separation occurred ahead of the elevons for the larger deflection angles. The same elevon deflections did not cause significant flow separation for the turbulent case, and turbulent heating levels were predicted by theory. The flow in the chordwise gap between the elevons was characterized by flow separation at the gap entrance and flow reattachment at a depth into the gap inversely proportional to the gap width. The gap entrance radius did not affect the gap-flow characteristics. The gap pressure and heating rate increased significantly with decreased elevon gap width, and the maximum gap heating rate was proportional to the maximum gap pressure. Although differential elevon deflections affected the gap-flow characteristics, the maximum gap heating level was not significantly increased. Correlation of the present results indicated that the gap heating was directly proportional to the elevon windward-surface pressure and was not dependent upon whether the boundary layer on the windward elevon surface was laminar or turbulent.

NASA Langley Research Center
Hampton, VA 23665-5225
October 19, 1988

References

1. Strouhal, George; and Tillian, Donald J.: Testing the Shuttle Heat-Protection Armor. *Astronaut. & Aeronaut.*, vol. 14, no. 1, Jan. 1976, pp. 57–65.
2. Hunt, L. Roane: *Aerothermal Environment in Chordwise Gaps Between Split Elevons at Mach 6.8.* NASA TP-1783, 1980.
3. Curry, Donald M.; Tillian, Donald J.: Space Shuttle Orbiter Thermal Protection System Flight Experiences. *Advances in TPS and Structures for Space Transportation Systems,* H. Neale Kelly and James E. Gardner, compilers, NASA CP-2315, 1984, pp. 139–163.
4. Wieting, Allan R.; Walsh, Joanne L.; and Bey, Kim S.: Aerothermal Environment in Control Surface Gaps in Hypersonic Flow—An Overview. AIAA-83-1483, June 1983.
5. Deveikis, William D.; and Hunt, L. Roane: *Loading and Heating of a Large Flat Plate at Mach 7 in the Langley 8-Foot High-Temperature Structures Tunnel.* NASA TN D-7275, 1973.
6. Leyhe, E. W.; and Howell, R. R.: *Calculation Procedure for Thermodynamic, Transport, and Flow Properties of the Combustion Products of a Hydrocarbon Fuel Mixture Burned in Air With Results for Ethylene-Air and Methane-Air Mixtures.* NASA TN D-914, 1962.
7. Ames Research Staff: *Equations, Tables, and Charts for Compressible Flow.* NACA Rep. 1135, 1953. (Supersedes NACA TN 1428.)
8. Kays, W. M.; and Crawford, M. E.: *Convective Heat and Mass Transfer,* Second ed. McGraw-Hill, Inc., c.1980.
9. Glass, Christopher E.; and Hunt, L. Roane: *Aerothermal Tests of Quilted Dome Models on a Flat Plate at a Mach Number of 6.5.* NASA TP-2804, 1988.
10. Glass, Christopher E.; and Hunt, L. Roane: *Aerothermal Tests of Spherical Dome Protuberances on a Flat Plate at a Mach Number of 6.5.* NASA TP-2631, 1986.
11. Harris, Julius E.; and Blanchard, Doris K.: *Computer Program for Solving Laminar, Transitional, or Turbulent Compressible Boundary-Layer Equations for Two-Dimensional and Axisymmetric Flow.* NASA TM-83207, 1982.
12. White, Frank M.: *Viscous Fluid Flow.* McGraw-Hill, Inc., c.1974, p. 493.
13. Schlichting, Hermann (J. Kestin, transl.): *Boundary-Layer Theory,* Seventh ed. McGraw-Hill Book Co., c.1979, p. 637.
14. Bushnell, Dennis M.; Johnson, Charles B.; Harvey, William D.; and Feller, William V.: *Comparison of Prediction Methods and Studies of Relaxation in Hypersonic Turbulent Nozzle-Wall Boundary Layers.* NASA TN D-5433, 1969.
15. Lukasiewicz, J.: Blast-Hypersonic Flow Analogy—Theory and Application. *American Rocket Soc. J.*, vol. 32, no. 9, Sept. 1962, pp. 1341–1346.
16. Deveikis, William D.: *Effects of Flow Separation and Cove Leakage on Pressure and Heat-Transfer Distributions Along a Wing-Cove-Elevon Configuration at Mach 6.9.* NASA TP-2127, 1983.

Table I. Locations of Model Pressure Orifices

Name	x, in.	y, in.	x', in.	y', in.	z', in.
Wing section					
PW1	13.50	−2.00			
PW4	31.50	↓			
PW9	49.50	↓			
PW12	67.50	↓			
PW19	75.05	9.00			
PW24	75.05	−9.00			
Lower elevon windward surface					
PL27	82.00	9.05	3.00	8.05	0.00
PL29	82.00	1.85	3.00	.85	↓
PL48	90.00	14.05	11.00	13.05	↓
PL49	↓	9.05	↓	8.05	↓
PL51	↓	3.71	↓	2.71	↓
PL60	↓	1.85	↓	.85	↓
PL69	98.00	14.05	19.00	13.05	↓
PL70	98.00	9.05	19.00	8.05	↓
PL77	98.00	1.85	19.00	.85	↓
Upper elevon windward surface					
PU33	82.00	−9.05	3.00	8.05	0.00
PU59	90.00	−9.05	11.00	8.05	.00
PU76	98.00	−9.05	19.00	8.05	.00
Lower elevon sidewall					
PLS31	82.40	1.00	3.40	0.00	1.040
PLS41	86.40	↓	7.40	↓	2.500
PLS52	90.00	↓	11.00	↓	.500
PLS54	90.40	↓	11.40	↓	1.900
PLS56	90.40	↓	11.40	↓	3.900
PLS73	98.40	↓	11.40	↓	1.119
Upper elevon sidewall					
PUS58	90.00	−1.00	11.00	0.00	3.400
Elevon leeward and base surfaces					
PB81	90.00	3.00	11.00	2.00	5.500
PB82	90.00	−3.00	11.00	2.00	5.500
PB79	103.00	2.00	24.00	1.00	1.000
PB80	103.00	−5.00	24.00	4.00	1.000
Boundary-layer rake					
BL1	72.00	−15.00			
BL2	72.00	−2.00			

Table II. Locations of Model Heat-Flux Gages

Name	x, in.	y, in.	x', in.	y', in.	z', in.
Wing section					
QW1	13.50	2.00			
QW2	19.50	↓			
QW3	25.50				
QW4	31.50				
QW5	37.50				
QW6	43.50	10.00			
QW7	43.50	2.00			
QW8	43.50	−10.00			
QW10	55.50	2.00			
QW11	60.45	2.00			
QW12	66.50	2.00			
QW13	68.50	10.00			
QW14	68.50	−10.00			
QW15	74.05	10.00			
QW16	74.05	2.00			
QW17	76.05	18.05			
QW18	↓	14.55			
QW19		10.00			
QW20		6.50			
QW21		2.50			
QW22		−2.00			
QW23		−6.00			
QW24		−10.00			
Lower elevon windward surface					
QL26	83.00	15.05	4.00	14.05	0.00
QL27	83.00	10.05	↓	9.05	↓
QL28	83.00	4.71		3.71	
QL29	83.76	2.15		1.15	
QL37	87.00	10.05	8.00	9.05	
QL48	91.00	15.05	12.00	14.05	
QL49	↓	10.05	↓	9.05	
QL50		7.90		6.90	
QL51		4.71		3.71	
QL60	91.80	2.15	12.80	1.15	
QL63	95.00	10.05	16.00	9.05	
QL69	99.00	15.05	20.00	14.05	
QL70	99.00	10.05	20.00	9.05	
QL71	99.00	4.71	20.00	3.71	
QL77	99.80	2.15	20.80	1.15	
Upper elevon windward surface					
QU33	83.00	−10.05	4.00	9.05	0.00
QU59	91.00	−10.05	12.00	9.05	.00
QU76	99.00	−10.05	20.00	9.05	.00

Table II. Concluded

Name	x, in.	y, in.	x', in.	y', in.	z', in.
Lower elevon sidewall					
QLS25	81.00	1.00	2.00	0.00	0.535
QLS30	83.00	↓	4.00	↓	.659
QLS31	83.00	↓	4.00	↓	1.263
QLS32	83.00	↓	4.00	↓	2.139
QLS34	85.00	↓	6.00	↓	1.012
QLS35	85.00	↓	6.00	↓	1.991
QLS36	85.00	↓	6.00	↓	3.539
QLS38	87.00	↓	8.00	↓	.688
QLS39	↓	↓	↓	↓	1.364
QLS40	↓	↓	↓	↓	2.038
QLS41	↓	↓	↓	↓	2.719
QLS42	↓	↓	↓	↓	3.420
QLS43	↓	↓	↓	↓	4.939
QLS44	↓	↓	↓	↓	6.340
QLS45	88.40	↓	9.40	↓	5.900
QLS46	89.00	↓	10.00	↓	1.717
QLS47	89.00	↓	10.00	↓	3.447
QLS52	91.00	↓	12.00	↓	.500
QLS53	↓	↓	↓	↓	1.038
QLS54	↓	↓	↓	↓	2.070
QLS55	↓	↓	↓	↓	3.110
QLS56	↓	↓	↓	↓	4.175
QLS57	↓	↓	↓	↓	5.000
QLS61	92.20	↓	13.20	↓	4.200
QLS62	93.00	↓	14.00	↓	2.422
QLS64	95.00	↓	16.00	↓	.500
QLS65	↓	↓	↓	↓	1.388
QLS66	↓	↓	↓	↓	2.775
QLS67	↓	↓	↓	↓	3.740
QLS68	97.00	↓	18.00	↓	3.080
QLS72	99.00	↓	20.00	↓	.500
QLS73	↓	↓	↓	↓	1.119
QLS74	↓	↓	↓	↓	1.738
QLS75	↓	↓	↓	↓	2.420
QLS78	102.25	↓	23.25	↓	.500
Upper elevon sidewall					
QUS58	91.00	−1.00	12.00	0.00	3.900

Table III. Model Configuration

Test	W, in.	R, in.	α, deg	δ_ℓ, deg	δ_u, deg
Blunt leading edge without flow trips					
1	2	0.00	0	0	0
2	↓	↓	0	10	10
3			0	20	20
4			5	0	0
5			5	5	5
6			5	10	10
7			10	0	0
8			10	5	5
9			10	10	10
10	1	.00	5	10	10
11	3	.00	5	10	10
12	1	.25	5	10	10
13	2	.25	5	10	10
14	3	.25	5	10	10
Sharp leading edge with flow trips					
15	2	0.00	0	0	0
16	↓	↓	0	10	10
17			5	0	0
18			5	5	5
19			5	10	10
20			10	0	0
21			10	10	10
22	2	.00	5	10	10
23	2	.00	5	10	10
24	2	.00	5	10	10
25	1	.00	5	10	10
26	3	.00	5	10	10
27	1	.25	5	10	10
28	2	.25	5	10	10
29	3	.25	5	10	10
30	1	.00	5	10	0
31	1	.00	5	10	20

Table IV. Test Flow Parameters

(a) Free stream

Test	T_t, °R	$p_{t,c}$, psia	$p_{t,\infty}$, psia	p_∞, psia	M_∞	q_∞, psi	$(\rho V/\mu)_\infty$, per foot	$(\rho V c)_\infty$, Btu/ft^2-sec-°R
Blunt leading edge without flow trips								
1	3263	618	331	0.0764	6.56	2.27	0.355E+06	0.834
2	3268	624	336	.0771	6.57	2.30	.358E+06	.842
3	3368	624	376	.0767	6.66	2.35	.354E+06	.843
4	3335	623	362	.0767	6.63	2.33	.355E+06	.841
5	3325	648	372	.0799	6.62	2.42	.369E+06	.875
6	3173	640	312	.0794	6.48	2.30	.373E+06	.862
7	3239	624	326	.0772	6.54	2.28	.360E+06	.842
8	3371	623	377	.0766	6.66	2.35	.353E+06	.842
9	3197	640	320	.0793	6.50	2.32	.371E+06	.863
10	3232	660	342	.0817	6.53	2.41	.381E+06	.890
11	3278	660	360	.0815	6.58	2.44	.379E+06	.890
12	3194	664	331	.0823	6.50	2.40	.385E+06	.895
13	3258	622	332	.0769	6.56	2.28	.358E+06	.839
14	3234	625	325	.0773	6.54	2.28	.361E+06	.843
Sharp leading edge with flow trips								
15	3292	624	345	0.0770	6.59	2.31	0.357E+06	0.842
16	3271	619	335	.0765	6.57	2.28	.355E+06	.835
17	3408	627	396	.0770	6.70	2.39	.354E+06	.847
18	3260	621	332	.0768	6.56	2.28	.357E+06	.838
19	3258	664	354	.0821	6.56	2.44	.382E+06	.896
20	3312	621	352	.0766	6.61	2.31	.355E+06	.838
21	3297	626	349	.0772	6.59	2.32	.358E+06	.845
22	3262	1023	548	.1264	6.56	3.76	.588E+06	1.380
23	3306	1516	853	.1870	6.60	5.63	.866E+06	2.046
24	3157	2507	1200	.3110	6.47	8.99	.146E+07	3.378
25	3317	619	352	.0763	6.61	2.31	.353E+06	.836
26	3320	654	374	.0806	6.62	2.44	.373E+06	.883
27	3297	622	346	.0768	6.59	2.31	.356E+06	.839
28	3309	623	352	.0768	6.61	2.32	.356E+06	.841
29	3343	625	366	.0770	6.64	2.34	.355E+06	.844
30	3304	622	349	.0767	6.60	2.31	.355E+06	.839
31	3293	617	342	.0762	6.59	2.29	.353E+06	.833

Table IV. Continued

(b) Wing surface

Test	α, deg	p_W, psia	$T_{aw,W}$, °R	T^*_W, °R	$(\rho V c)^*_W$, Btu/ft^2-sec-°R	$(\rho V/\mu)^*_W$, per foot
Blunt leading edge without flow trips						
1	0	0.0764	3012	1047	0.349	0.673E+05
2	0	.0771	3016	1048	.353	.678E+05
3	0	.0767	3108	1071	.353	.666E+05
4	5	.1636	3087	1094	.722	.134E+06
5	5	.1700	3078	1092	.750	.139E+06
6	5	.1665	2938	1057	.729	.139E+06
7	10	.3079	3010	1112	1.280	.234E+06
8	10	.3123	3133	1145	1.306	.232E+06
9	10	.3142	2972	1102	1.304	.240E+06
10	5	.1723	2992	1070	.757	.143E+06
11	5	.1728	3035	1081	.761	.142E+06
12	5	.1730	2957	1061	.758	.144E+06
13	5	.1626	3016	1076	.716	.134E+06
14	5	.1632	2994	1071	.717	.135E+06
Sharp leading edge with flow trips						
15	0	0.0770	3039	1054	0.353	0.676E+05
16	0	.0765	3019	1049	.350	.673E+05
17	5	.1652	3154	1111	.732	.134E+06
18	5	.1624	3018	1077	.715	.134E+06
19	5	.1736	3016	1076	.764	.143E+06
20	10	.3091	3078	1130	1.290	.232E+06
21	10	.3111	3064	1126	1.297	.234E+06
22	5	.2675	3020	1077	1.177	.221E+06
23	5	.3974	3060	1088	1.752	.326E+06
24	5	.6516	2923	1053	2.852	.546E+06
25	5	.1624	3071	1090	.716	.133E+06
26	5	.1716	3073	1091	.757	.141E+06
27	5	.1630	3052	1086	.718	.134E+06
28	5	.1633	3063	1088	.720	.134E+06
29	5	.1641	3094	1096	.725	.134E+06
30	5	.1630	3059	1087	.719	.134E+06
31	5	.1616	3048	1085	.712	.133E+06

Table IV. Concluded

(c) Elevon surface

Test	δ, deg	p_L, psia	$T_{aw,L}$, °R	T_L^*, °R	$(\rho V c)_L^*$, Btu/ft^2-sec-°R	$(\rho V/\mu)_L^*$, per foot
Blunt leading edge without flow trips						
1	0	0.0764	3012	1047	0.349	0.673E+05
2	10	.3090	3037	1119	1.287	.233E+06
3	20	.8229	3170	1281	2.885	.463E+06
4	0	.1636	3087	1094	.722	.134E+06
5	5	.3332	3088	1125	1.408	.254E+06
6	10	.5734	2959	1127	2.270	.409E+06
7	0	.3079	3010	1112	1.280	.234E+06
8	5	.5646	3143	1180	2.252	.390E+06
9	10	.9424	2994	1178	3.520	.610E+06
10	10	.5980	3013	1142	2.373	.423E+06
11	10	.6032	3056	1154	2.399	.423E+06
12	10	.5973	2978	1132	2.366	.425E+06
13	10	.5663	3038	1149	2.250	.399E+06
14	10	.5665	3015	1143	2.248	.400E+06
Sharp leading edge with flow trips						
15	0	0.0770	3039	1054	0.353	0.676E+05
16	10	.3066	3040	1120	1.277	.232E+06
17	0	.1652	3154	1111	.732	.134E+06
18	5	.3167	3027	1109	1.334	.244E+06
19	10	.6046	3038	1149	2.402	.426E+06
20	0	.3091	3078	1130	1.290	.232E+06
21	10	.9425	3087	1205	3.533	.600E+06
22	10	.9321	3041	1150	3.705	.656E+06
23	10	1.3928	3082	1162	5.547	.973E+06
24	10	2.2392	2944	1123	8.857	.160E+07
25	10	.5699	3092	1165	2.271	.398E+06
26	10	.6024	3095	1165	2.401	.420E+06
27	10	.5705	3074	1159	2.271	.399E+06
28	10	.5727	3085	1163	2.281	.400E+06
29	10	.5782	3117	1171	2.307	.420E+06
30	0	.1630	3059	1087	.719	.134E+06
31	20	1.3970	3109	1291	4.678	.746E+06

Table V. Model Pressure Data

$[p/p_\infty]$

Test	PW1	PW4	PW9	PW12	PW19	PW24	PL27	PL29	PL48	PL49	PL51	PL60	PL69	PL70	PL77
Blunt leading edge without flow trips															
1	1.531	1.073	1.073	1.008	1.047	1.021	1.047	0.929	1.427	1.086	0.955	0.903	1.950	1.191	1.034
2	1.686	1.245	1.180	1.206	1.453	1.414	1.738	1.543	5.486	3.009	2.607	2.322	8.340	4.903	3.165
3	1.578	1.265	1.343	1.799	1.877	1.995	2.738	2.595	16.037	7.093	6.206	5.567	29.531	20.196	11.825
4	2.608	2.177	2.073	2.099	2.112	2.099	2.151	1.864	2.177	2.099	1.930	1.643	2.151	2.125	1.786
5	2.691	2.290	2.178	2.178	2.240	2.253	3.029	2.666	3.705	3.479	3.254	2.791	3.980	3.930	3.279
6	2.783	2.355	2.305	2.355	2.809	2.771	3.841	3.501	6.637	6.209	5.768	4.798	7.594	7.607	6.209
7	4.417	4.028	3.860	3.899	3.899	3.925	3.964	3.446	4.093	3.886	3.549	2.992	4.275	4.067	3.329
8	4.399	3.903	3.760	3.799	3.812	3.825	5.496	4.674	6.919	6.436	5.927	5.013	9.308	7.219	5.901
9	4.414	4.048	3.859	3.909	4.048	4.111	7.907	6.734	12.043	11.173	10.441	8.928	14.981	12.648	10.378
10	2.509	2.081	1.995	2.069	2.460	2.448	3.452	2.999	6.108	5.618	5.226	4.700	7.087	6.891	6.255
11	2.564	2.110	2.123	2.037	2.442	2.466	3.534	3.166	6.209	5.718	5.288	4.417	7.129	7.104	5.558
12	2.625	2.151	2.041	2.066	2.454	2.467	3.439	3.026	6.015	5.553	5.155	4.617	7.679	6.829	6.112
13	2.822	2.406	2.341	2.406	2.835	2.783	3.927	3.563	6.723	6.229	5.735	4.824	7.503	7.399	6.060
14	2.561	2.122	2.018	2.070	2.458	2.432	3.674	3.299	6.339	5.873	5.408	4.502	7.154	7.050	5.524
Sharp leading edge with flow trips															
15	1.078	1.000	1.013	1.026	1.026	1.039	1.026	0.948	1.169	1.065	0.948	0.909	1.169	1.091	0.883
16	1.124	1.072	1.098	1.137	1.373	1.399	2.601	1.974	4.510	4.144	3.987	3.516	4.588	4.392	3.608
17	2.364	2.208	2.117	2.273	2.221	2.234	2.208	2.117	2.403	2.195	2.143	1.753	2.403	2.286	1.844
18	2.305	2.174	2.070	2.253	2.227	2.174	3.555	3.242	4.844	4.154	4.036	3.359	5.313	4.570	3.555
19	2.290	2.156	2.071	2.205	2.156	2.168	5.542	4.957	7.771	7.296	7.320	6.151	7.820	7.795	6.261
20	4.413	4.164	3.838	4.099	4.008	4.047	4.034	3.708	4.334	3.982	3.851	3.146	4.465	4.295	3.394
21	4.249	4.041	3.718	3.964	3.925	3.912	9.650	8.484	13.977	12.202	11.891	9.922	17.694	13.692	10.492
22	2.366	2.278	2.168	2.373	2.278	2.334	6.005	5.309	8.101	7.729	7.824	6.653	8.220	8.220	6.669
23	2.342	2.235	2.091	2.289	2.257	2.262	5.925	5.273	8.000	7.652	7.765	6.610	8.080	8.096	6.508
24	2.203	2.103	1.920	2.151	2.122	2.145	6.003	5.238	7.559	7.174	7.280	6.318	7.614	7.595	6.100
25	2.346	2.189	2.110	2.267	2.215	2.228	5.570	4.928	7.864	7.339	7.313	6.461	7.995	7.811	7.300
26	2.295	2.159	2.072	2.233	2.159	2.196	5.608	4.975	8.052	7.481	7.457	6.303	8.139	8.015	6.328
27	2.305	2.174	2.096	2.253	2.174	2.201	5.664	5.078	8.112	7.500	7.422	6.419	8.333	8.060	7.161
28	2.357	2.214	2.122	2.279	2.214	2.240	5.547	4.961	7.839	7.292	7.253	6.068	7.930	7.839	6.094
29	2.260	2.078	2.065	2.169	2.156	2.143	5.649	4.896	9.377	7.571	7.377	6.117	11.351	8.649	6.143
30	2.269	2.138	2.047	2.177	2.151	2.138	5.476	4.850	7.705	7.197	7.158	5.971	7.797	7.679	5.945
31	2.283	2.165	2.073	2.244	2.152	2.178	5.499	4.948	7.559	7.073	7.231	7.638	8.793	7.546	6.982

Table V. Continued

$[p/p_\infty]$

Test	PU33	PU59	PU76	PLS31	PLS41	PLS52	PLS54	PLS56	PLS73	PUS58	PB81	PB82	PB79	PB80
Blunt leading edge without flow trips														
1	1.047	1.113	1.126	0.406	0.406	0.432	0.432	0.458	0.602	0.510	0.423	0.428	0.665	0.670
2	1.777	2.944	4.073	.584	.493	.610	.687	.830	1.064	.558	.451	.507	.774	.826
3	2.842	6.923	17.040	1.734	1.213	1.525	1.551	1.239	3.716	1.134	.652	.821	1.682	1.636
4	2.164	2.177	2.099	.326	.274	.456	.469	.222	.691	.274	.196	.192	.343	.408
5	3.004	3.630	3.842	.526	.451	.726	.826	.375	1.252	.451	.272	.287	.438	.492
6	3.929	6.385	7.380	.743	.705	.957	1.310	.579	2.053	.693	.406	.419	.553	.608
7	4.003	4.041	3.977	.505	.479	.777	.868	.350	1.218	.440	.196	.192	.417	.519
8	5.666	6.684	7.611	.679	.640	1.044	1.319	.470	2.010	.587	.185	.202	.439	.496
9	8.083	11.387	12.295	.895	.996	1.425	2.043	.643	3.581	.794	.148	.159	.353	.433
10	3.574	5.985	6.989	.734	.465	1.640	.845	.526	1.493	.526	.137	.158	.306	.351
11	3.816	6.196	7.288	.466	.393	.528	.871	.454	1.031	.552	.180	.193	.364	.402
12	3.572	5.930	6.926	.778	.547	1.871	1.154	.535	2.236	.668	.153	.170	.390	.416
13	4.044	6.554	7.386	.832	.806	1.235	1.391	.663	2.133	.767	.427	.462	.635	.679
14	3.959	6.210	7.167	.453	.375	.362	.750	.479	.970	.556	.157	.177	.358	.401
Sharp leading edge with flow trips														
15	1.065	1.169	1.078	0.494	0.169	0.195	0.195	0.169	0.299	0.221	0.162	0.126	0.274	0.297
16	2.536	4.248	4.353	.758	.288	.379	.471	.196	1.268	.275	.158	.175	.292	.325
17	2.247	2.299	2.325	.286	.234	.429	.442	.234	.701	.286	.164	.156	.299	.377
18	3.633	4.401	4.492	.365	.299	.547	.716	.273	1.211	.352	.143	.141	.298	.372
19	5.579	7.576	7.820	.426	.390	.743	1.206	.353	2.363	.426	.078	.095	.274	.337
20	4.047	4.413	4.125	.352	.287	.679	.770	.261	1.240	.326	.110	.108	.292	.375
21	9.521	12.487	12.681	.699	.725	1.321	2.176	.570	4.041	.725	.104	.120	.321	.385
22	5.965	8.188	8.481	.427	.396	.704	1.297	.348	2.658	.435	.081	.094	.180	.229
23	5.979	7.866	8.091	.385	.358	.599	1.251	.326	2.706	.417	.076	.090	.162	.196
24	5.942	7.781	7.977	.232	.199	.405	1.109	.177	2.482	.283	.094	.095	.104	.128
25	5.609	7.720	8.100	.511	.498	2.280	.957	.498	1.927	.603	.128	.136	.316	.368
26	5.707	8.077	8.065	.422	.323	.583	.645	.323	1.030	.360	.125	.141	.297	.318
27	5.573	7.565	7.852	.534	.482	2.214	1.276	.495	2.891	.638	.122	.126	.299	.355
28	5.664	7.813	7.956	.521	.482	.898	1.302	.430	2.578	.534	.159	.171	.371	.387
29	5.506	7.766	7.766	.403	.338	.844	.584	.286	.948	.325	.110	.105	.301	.314
30	2.112	2.203	2.216	.404	.417	.756	1.565	.378	.900	.326	.087	.064	.265	.335
31	13.740	19.068	19.488	.551	.459	.630	1.260	.512	1.732	1.129	.104	.131	.331	.382

Table V. Concluded

$[p/p_\infty]$

Test	PS	PT1	PT2	PT3	PT4	PT5	PT6	PT7	PT8	PT9	PT10	PT11	PT12	PT13	PT14
Blunt leading edge without flow trips															
1	1.039	1.419	2.102	3.486	5.026	6.558	10.746	12.446	14.041	15.084	15.726	16.678	18.839	23.781	29.215
2	1.244	1.512	1.977	2.975	2.064	5.573	9.709	12.519	14.240	15.671	16.042	16.930	19.021	23.927	29.595
3	1.794	1.847	2.302	2.373	2.430	2.540	2.965	4.657	5.492	7.536	8.917	11.374	14.656	20.256	26.356
4	1.969	3.274	5.605	9.477	13.875	17.087	20.030	24.729	27.352	31.791	34.512	40.949	50.416	65.733	76.932
5	2.095	3.562	5.801	9.116	13.160	16.337	20.826	24.472	26.417	29.982	32.746	38.073	46.851	62.731	73.980
6	2.252	3.547	5.372	8.601	12.650	16.107	20.500	24.511	26.693	30.574	32.712	37.986	47.048	63.462	76.033
7	3.759	9.934	17.390	23.645	30.034	35.025	43.460	48.206	56.074	67.035	73.927	86.913	104.999	126.772	138.561
8	3.735	9.228	16.586	22.903	29.225	34.051	42.516	46.986	54.514	65.753	72.436	85.838	103.854	126.319	136.926
9	3.677	10.985	20.079	25.072	31.111	35.796	42.900	48.397	55.980	67.666	74.356	88.050	105.300	126.555	136.406
10	1.973	3.151	4.984	8.510	12.673	15.994	16.721	23.978	25.880	29.635	32.211	37.650	46.263	62.514	74.902
11	1.960	3.480	5.715	9.013	13.265	16.396	17.864	24.226	26.409	30.098	32.348	37.509	46.188	62.596	75.263
12	1.972	3.373	5.306	8.714	12.916	16.748	18.118	24.117	26.222	30.219	32.104	37.340	46.200	62.461	74.357
13	2.295	3.427	5.222	8.571	12.523	15.750	20.079	24.269	26.549	30.676	33.300	38.723	47.347	63.684	75.437
14	1.965	3.514	5.984	9.609	13.609	16.704	20.757	25.213	27.175	31.590	34.690	40.567	49.543	64.881	75.801
Sharp leading edge with flow trips															
15	1.088	2.390	6.157	9.318	13.079	16.971		36.687	45.409	52.768	54.481	57.256	58.099	58.387	59.251
16	1.188	2.318	4.633	7.148	11.369	16.063		42.239	50.214	56.359	57.708	59.044	58.308	58.869	59.818
17	2.244	10.309	28.283	32.201	33.774	37.206		49.123	57.871	69.577	76.970	89.665	100.345	104.969	104.488
18	2.217	10.349	27.262	31.163	32.698	35.818		49.052	57.135	68.201	74.845	86.940	97.241	101.266	102.579
19	2.177	10.424	26.945	30.973	32.505	35.776		48.837	57.040	68.207	73.745	88.491	98.592	101.879	102.797
20	4.034	21.338	45.261	51.087	52.997	58.409		78.273	90.607	108.298	118.961	136.281	147.577	154.129	156.903
21	3.863	20.383	43.412	48.604	50.525	55.587		75.361	87.845	105.126	115.373	132.823	144.237	150.249	153.266
22	2.299	12.745	28.647	32.447	33.759	37.396		52.079	61.453	74.863	83.975	98.851	107.315	109.517	110.168
23	2.194	13.433	28.405	32.039	33.187	37.198		52.985	62.929	76.579	85.680	98.504	103.133	104.496	105.093
24	2.193	14.379	30.975	33.054	34.869	39.254		56.390	67.340	80.788	89.745	100.442	103.885	105.123	105.609
25	2.239	10.215	28.147	32.495	34.066	37.206		50.582	58.908	71.089	78.933	91.539	101.404	105.007	15.515
26	2.228	10.287	27.965	32.165	33.712	36.813		50.439	58.847	70.323	78.263	92.239	102.146	104.825	106.443
27	2.215	10.191	27.556	31.620	33.000	35.965		49.900	57.415	68.357	75.736	87.831	97.512	100.780	102.023
28	2.254	10.642	28.392	32.526	33.951	37.491		51.152	58.725	70.303	77.405	90.072	100.573	104.193	105.203
29	2.165	9.658	26.918	31.016	32.516	35.622		48.013	55.818	67.118	74.551	87.179	98.345	102.578	103.508
30	2.169	9.647	27.094	31.245	32.704	35.724		48.040	56.166	67.193	74.536	86.434	96.098	99.837	101.278
31	2.181	10.125	27.791	32.087	33.720	37.138		50.521	59.054	69.371	76.593	88.445	98.261	102.033	103.104

Table VI. Model Heat Transfer Data

$[N_{St,\infty} \times 10^3]$

Test	QW1	QW2	QW3	QW4	QW5	QW6	QW7	QW8	QW10	QW11	QW12	QW13	QW14
Blunt leading edge without flow trips													
1	0.600	0.468	0.329	0.341	0.266	0.372	0.266	0.313	0.248	0.235	0.226	0.232	0.222
2	.579	.448	.341	.344	.279	.371	.279	.314	.260	.240	.220	.226	.189
3	.590	.456	.332	.337	.271	.352	.284	.322	.258	.242	.281	.289	.281
4	.844	.680	.523	.490	.383	.561	.394	.482	.370	.348	.333	.382	.371
5	.771	.629	.473	.480	.381	.501	.392	.488	.375	.359	.348	.362	.369
6	.745	.617	.460	.486	.384	.525	.396	.480	.383	.365	.364	.379	.371
7	1.120	.942	.725	.711	.564	.876	.622	.804	.705	.742	.814	.993	.985
8	1.092	.945	.730	.737	.583	.811	.603	.712	.619	.630	.684	.790	.868
9	1.054	.891	.672	.697	.543	.835	.577	.743	.620	.645	.707	.902	.924
10	.758	.619	.442	.460	.363	.486	.371	.457	.349	.331	.307	.364	.358
11	.746	.637	.450	.471	.367	.553	.384	.459	.367	.355	.344	.388	.362
12	.768	.636	.474	.475	.376	.521	.386	.474	.376	.365	.360	.383	.392
13	.777	.645	.473	.491	.385	.524	.404	.482	.383	.373	.361	.407	.392
14	.775	.601	.496	.500	.397	.528	.401	.475	.383	.365	.351	.386	.384
Sharp leading edge with flow trips													
15	0.583	0.452	0.350	0.367	0.285	0.494	0.315	0.389	0.320	0.320	0.340	0.457	0.403
16	.623	.484	.372	.390	.305	.567	.342	.429	.370	.384	.408	.506	.463
17	1.508	1.547	1.514	1.857	1.624	2.360	1.827	2.046	1.918	1.847	1.830	1.792	1.757
18	1.637	1.618	1.593	1.901	1.634	2.427	1.815	1.964	1.842	1.775	1.764	1.782	1.679
19	1.709	1.735	1.665	1.899	1.622	2.130	1.748	1.934	1.773	1.705	1.677	1.647	1.643
20	4.125	3.928	3.263	3.314	2.679	3.631	2.812	3.097	2.827	2.730	2.695	2.710	2.567
21	3.894	3.720	3.055	3.149	2.535	3.433	2.675	2.930	2.693	2.603	2.571	2.560	2.449
22	2.153	2.060	1.754	1.828	1.496	2.072	1.604	1.838	1.641	1.589	1.570	1.545	1.546
23	1.867	1.837	1.564	1.620	1.329	1.850	1.412	1.622	1.462	1.420	1.401	1.385	1.378
24	1.659	1.669	1.415	1.482	1.218	1.714	1.298	1.534	1.364	1.331	1.336	1.291	1.304
25	1.586	1.567	1.558	1.984	1.715	2.455	1.923	2.063	1.959	1.887	1.851	1.885	1.740
26	1.672	1.820	1.806	2.085	1.738	2.389	1.875	2.097	1.865	1.809	1.781	1.790	1.768
27	1.570	1.555	1.506	1.807	1.575	2.402	1.785	1.970	1.856	1.792	1.772	1.788	1.698
28	1.534	1.559	1.575	1.923	1.671	2.380	1.871	1.991	1.906	1.844	1.821	1.840	1.709
29	1.499	1.545	1.487	1.846	1.603	2.287	1.802	1.946	1.892	1.829	1.810	1.807	1.684
30	1.536	1.509	1.481	1.863	1.631	2.358	1.825	1.915	1.882	1.812	1.808	1.826	1.655
31	1.586	1.627	1.535	1.855	1.597	2.313	1.797	1.953	1.860	1.797	1.786	1.804	1.676

Table VI. Continued

$[N_{St,\infty} \times 10^3]$

Test	QW15	QW16	QW17	QW18	QW19	QW20	QW21	QW22	QW23	QW24	QL26	QL27	QL28
Blunt leading edge without flow trips													
1	0.232	0.198	0.384		0.198	0.203	0.196	0.449	0.185	0.216	0.229	0.164	0.159
2	.110	.084	.368	0.184	.104	.108	.097	.085	.091	.091	.786	.546	.473
3	.461	.504	1.003	.692	.479	.545	.600	.573	.541	.533	4.187	1.852	1.825
4	.371	.318	.458		.317	.334	.326	.306	.325	.368	.344	.326	.287
5	.344	.330	.544		.249	.273	.320	.307	.290	.332	.504	.387	.359
6	.157	.160	.292		.138	.156	.143	.145	.160	.172	1.909	1.670	1.539
7	1.096	.904	1.365		.967	.958	.973	.976	.989	1.178	1.396	1.091	.931
8	.877	.753	1.274		.739	.764	.814	.803	.863	1.060	2.232	1.662	1.480
9	.954	.740	1.326		.764	.751	.739	.717	.790	1.010	5.134	4.110	3.675
10	.164	.123	.298	.191	.132	.126	.125	.128	.142	.159	1.617	1.413	1.317
11	.214	.202	.371	.234	.166	.171	.177	.160	.165	.184	1.584	1.444	1.396
12	.208	.195	.352	.233	.171	.182	.192	.188	.200	.237	1.791	1.560	1.466
13	.182	.184	.317	.194	.150	.160	.166	.179	.201	.223	1.631	1.427	1.329
14	.203	.196	.336	.209	.155	.153	.162	.174	.169	.198	1.701	1.518	1.385
Sharp leading edge with flow trips													
15	0.478	0.361	0.558	0.507	0.413	0.402	0.381	0.368	0.396	0.443	0.593	0.476	0.404
16	.453	.346	.605	.483	.353	.340	.364	.360	.346	.402	2.648	2.067	1.670
17	1.784	1.731	1.594	1.644	1.525	1.664	1.788	1.719	1.713	1.827	1.738	1.639	1.589
18	1.774	1.665	1.599	1.658	1.516	1.638	1.725	1.654	1.622	1.752	3.040	2.828	2.721
19	1.639	1.594	1.444	1.497	1.387	1.518	1.645	1.601	1.595	1.720	4.324	3.869	3.880
20	2.694	2.574	2.401	2.481	2.273	2.487	2.649	2.533	2.509	2.691	2.832	2.487	2.503
21	2.541	2.438	2.281	2.345	2.144	2.357	2.512	2.416	2.407	2.568	6.881	5.782	5.948
22	1.534	1.506	1.295	1.383	1.304	1.437	1.550	1.500	1.511	1.634	4.303	3.698	3.807
23	1.386	1.334	1.152	1.236	1.165	1.284	1.385	1.338	1.350	1.438	4.172	3.353	3.484
24	1.284	1.260	1.111	1.147	1.089	1.208	1.305	1.272	1.282	1.351	4.501	3.301	3.527
25	1.875	1.770	1.708	1.748	1.604	1.738	1.820	1.731	1.692	1.818	5.211	4.661	4.482
26	1.768	1.699	1.652	1.661	1.509	1.643	1.753	1.696	1.695	1.838	5.027	4.443	4.320
27	1.763	1.679	1.619	1.658	1.512	1.648	1.731	1.661	1.638	1.764	5.142	4.644	4.404
28	1.831	1.725	1.692	1.727	1.563	1.694	1.776	1.680	1.653	1.776	4.979	4.431	4.317
29	1.806	1.705	1.626	1.685	1.534	1.667	1.765	1.684	1.654	1.765	5.013	4.478	4.304
30	1.816	1.705	1.675	1.711	1.561	1.675	1.763	1.675	1.624	1.735	5.013	4.451	4.290
31	1.798	1.687	1.681	1.708	1.533	1.648	1.736	1.657	1.632	1.758	4.861	4.339	4.124

Table VI. Continued

$[N_{St,\infty} \times 10^3]$

Test	QL29	QL37	QL48	QL49	QL50	QL51	QL60	QL63	QL69	QL70	QL71	QL77	QU33
Blunt leading edge without flow trips													
1	0.236	0.162	0.598	0.158	0.219	0.174	0.193	0.367	0.876	0.466	0.156	0.148	0.147
2	.591	.956	2.532	1.474	1.463	1.248	1.016	1.878	2.965	2.386	1.855	1.468	.511
3	2.249	3.524	11.361	5.153	4.620	4.397	4.065	7.642	12.418	15.653	7.428	6.042	1.905
4	.418	.308	.445	.342	.371	.351	.377	.386	.419	.349	.347	.340	.289
5	.557	.572	1.016	.837	.912	.691	.659	1.164	1.277	1.252	.994	.822	.432
6	1.759	3.004	4.014	4.084	3.740	3.413	2.985	3.711	3.979	4.287	4.036	3.498	2.044
7	1.177	1.234	1.768	1.491	1.514	1.255	1.143	1.641	1.893	1.787	1.485	1.345	1.394
8	1.895	2.315	3.687	3.318	3.059	2.613	2.377	3.501	5.135	3.993	3.327	2.871	2.409
9	4.305	5.513	7.167	7.594	6.085	5.823	5.356	6.034	7.505	7.411	6.676	5.795	5.338
10	1.517	2.619	3.451	3.582	3.286	3.068	2.689	3.282	3.539	3.733	3.542	3.231	1.900
11	1.618	2.678	3.636	3.765	3.477	3.267	2.693	3.426	3.944	4.165	3.846	3.133	1.834
12	1.588	2.728	3.822	3.929	3.504	3.189	2.693	3.542	4.070	4.069	3.879	3.356	1.990
13	1.499	2.679	3.792	3.805	3.613	3.260	2.668	3.580	4.062	4.262	4.038	3.282	1.831
14	1.582	2.503	3.375	3.522	3.423	3.040	2.583	3.403	3.597	3.941	3.632	3.128	1.915
Sharp leading edge with flow trips													
15	0.494	0.517	0.691	0.580	0.530	0.522	0.486	0.543	0.733	0.634	0.560	0.482	0.523
16	1.946	2.843	3.765	3.397	3.145	3.033	2.659	3.238	3.791	3.772	3.699	2.935	2.339
17	1.752	1.636	1.800	1.783	1.765	1.668	1.391	1.650	1.622	1.761	1.685	1.383	1.842
18	2.921	3.121	3.547	3.667	3.273	3.224	2.713	3.060	3.255	3.551	3.383	2.745	3.147
19	4.243	4.767	5.378	5.703	5.061	5.142	4.324	4.632	4.807	5.265	5.261	4.256	4.884
20	2.760	2.624	2.869	2.927	2.719	2.586	2.164	2.540	2.614	2.849	2.635	2.206	2.896
21	6.172	7.131	8.213	8.712	7.277	7.429	6.173	6.953	9.124	8.029	7.476	6.286	7.215
22	3.979	4.765	5.263	5.856	4.868	5.181	4.245	4.436	4.729	5.324	5.165	4.296	4.908
23	3.581	4.369	4.914	5.454	3.552	4.719	3.862	3.379	4.281	4.844	4.756	4.002	4.631
24	3.360	3.936	4.646	4.804	2.273	4.352	3.423	2.161	3.928	4.348	4.435	3.689	4.699
25	4.805	5.463	6.198	6.256	5.735	5.733	4.853	5.291	5.558	6.013	5.917	5.174	5.402
26	4.705	5.267	6.083	6.158	5.600	5.660	4.743	5.148	5.459	5.811	5.917	4.656	5.870
27	4.675	5.417	6.202	6.287	5.559	5.710	4.710	5.106	5.509	5.917	5.740	4.969	5.367
28	4.584	5.294	6.051	6.083	5.691	5.562	4.559	5.252	5.438	5.781	5.657	4.511	5.290
29	4.658	5.282	5.909	6.059	5.621	5.581	4.547	5.135	5.474	5.714	5.712	4.545	5.372
30	4.539	5.176	5.864	5.902	5.530	5.415	4.436	5.098	5.239	5.611	5.522	4.345	1.780
31	4.535	5.006	5.711	5.708	5.409	5.310	5.312	4.967	5.592	5.437	5.906	5.179	13.570

Table VI. Continued

$[N_{St,\infty} \times 10^3]$

Test	QU59	QU76	QLS25	QLS30	QLS31	QLS32	QLS34	QLS35	QLS36	QLS38	QLS39	QLS40	QLS41
Blunt leading edge without flow trips													
1	0.166	0.252	0.076	0.091	0.059	0.013	0.109	0.080	0.027	0.063	0.133	0.188	0.134
2	1.264	2.026	.163	.064	.096	.098	.132	.113	.096	.152	.263	.227	.170
3	5.291	12.605	1.127	.548	.667	.652	.630	.579	.500	.737	.816	.716	.631
4	.282	.371	.170	.170	.165	.054	.210	.181	.054	.164	.338	.271	.208
5	.819	1.228	.197	.222	.207	.094	.314	.253	.103	.240	.504	.396	.283
6	3.702	4.657	.360	.186	.179	.144	.443	.335	.126	.349	.851	.647	.445
7	1.574	2.084	.433	.440	.363	.163	.485	.362	.155	.395	.659	.508	.371
8	3.324	4.671	.515	.448	.415	.201	.572	.462	.198	.441	.866	.689	.506
9	6.231	8.120	.841	.659	.612	.304	.919	.746	.291	.717	1.521	1.160	.809
10	3.516	4.362	.463	.251	.247	.192	.665	.288	.162	1.194	.666	.406	.395
11	3.402	4.453	.368	.208	.175	.112	.391	.262	.122	.257	.431	.400	.330
12	3.636	4.419	.218	.377	.344	.192	.719	.380	.194	1.040	.721	.535	.463
13	3.491	4.299	.174	.266	.256	.143	.390	.329	.154	.354	.609	.553	.414
14	3.485	4.509	.180	.262	.243	.116	.362	.269	.140	.337	.387	.339	.292
Sharp leading edge with flow trips													
15	0.593	0.695	0.115	0.143	0.107	0.014	0.134	0.090	0.012	0.118	0.056	0.136	0.099
16	3.447	4.339	.312	.245	.197	.109	.291	.206	.094	.395	.352	.319	.253
17	1.738	1.773	.366	.525	.311	.046	.454	.232	.033	.421	7.700	.332	.247
18	3.272	3.465	.512	.666	.387	.121	.588	.304	.091	.516	.598	.445	.337
19	5.216	5.700	.747	.848	.523	.191	.781	.391	.147	.704	.779	.624	.468
20	2.645	2.799	.539	.731	.440	.157	.640	.329	.121	.520	.659	.499	.376
21	7.337	9.017	1.189	1.241	.793	.300	1.159	.617	.252	.922	1.320	1.046	.748
22	5.335	5.723	.688	.776	.463	.171	.720	.352	.135	.608	.732	.586	.433
23	4.875	4.993	.570	.697	.398	.142	.654	.306	.112	.521	.000	.523	.385
24	4.731	4.740	.495	.659	.351	.112	.630	.266	.085	.510	.636	.468	.334
25	5.594	6.029	.684	1.172	.740	.271	1.387	.530	.248	1.956	1.149	.704	.595
26	5.974	6.443	.836	.895	.588	.217	.817	.425	.147	.758	.738	.528	.379
27	5.467	5.965	.450	.901	.719	.289	1.297	.549	.241	1.596	1.137	.686	.562
28	5.567	5.920	.655	.741	.496	.187	.681	.373	.158	.729	.662	.589	.488
29	5.399	5.877	.688	.742	.506	.197	.692	.376	.131	.755	.626	.459	.340
30	1.598	1.759	.630	.922	.592	.239	.963	.617	.223	.765	1.382	.937	.567
31	11.494	12.060	.733	1.233	.686	.252	.946	.491	.249	1.129	.843	.707	.574

Table VI. Continued

$[N_{St,\infty} \times 10^3]$

Test	QLS42	QLS43	QLS44	QLS45	QLS46	QLS47	QLS52	QLS53	QLS54	QLS55	QLS56	QLS57	QLS61
Blunt leading edge without flow trips													
1	0.060		0.045	0.073	0.127	0.152	0.109	0.173	0.155		0.163	0.146	0.185
2	.126	0.104	.115	.154	.397	.169	.209	.504	.461		.159	.178	.186
3	.558	.452	.450	.526	1.065	.664	.962	1.482	1.351		.685	.612	.707
4	.144	.059	.028	.075	.346	.177	.161	.365	.350		.145	.128	.150
5	.189	.100	.055	.113	.494	.230	.236	.579	.516		.191	.162	.182
6	.296	.155	.086	.174	.960	.389	.432	1.162	1.030		.313	.246	.298
7	.257	.134	.091	.139	.633	.297	.378	.741	.653		.248	.206	.245
8	.351	.180	.124	.201	.922	.410	.498	1.105	1.013		.361	.306	.362
9	.546	.272	.181	.293	1.648	.651	.791	1.976	1.781		.537	.436	.515
10	.309	.185		.222	.590	.405	1.627	1.308	.768	0.599	.499	.366	.423
11	.256	.129		.131	.469	.405	.192	.337	.892	.717	.449	.273	.368
12	.349	.218	.146	.261	.779	.432	1.437	1.377	.939		.451	.378	.447
13	.283	.149	.098	.175	.893	.383	.375	.905	.976		.337	.293	.346
14	.234	.130	.070	.133	.405	.358	.333	.351	.665		.401	.280	.365
Sharp leading edge with flow trips													
15	0.063	0.026		0.076	0.188	0.078	0.118	0.222	0.210	0.110	0.076	0.087	0.077
16	.176	.088		.099	.442	.232	.449	.617	.616	.365	.220	.152	.172
17	.169	.030		.039	.521	.220	.417	.755	.576	.343	.225	.161	.179
18	.236	.097		.112	.725	.301	.494	1.008	.852	.476	.298	.199	.234
19	.322	.145		.163	1.060	.423	.650	1.423	1.326	.720	.411	.266	.334
20	.265	.116		.137	.809	.321	.529	1.093	.863	.487	.308	.211	.246
21	.507	.227		.228	1.791	.657	1.002	2.463	2.087	1.113	.632	.413	.503
22	.291	.129		.132	1.051	.392	.526	1.302	1.317	.695	.380	.242	.308
23	.255	.107		.106	.972	.358	.412	1.141	1.244	.647	.347	.221	.282
24	.219	.087		.084	.919	.325	.385	1.257	1.173	.586	.283	1.96	.250
25	.442	.223		.235	.973	.528	2.556	2.095	1.125	.884	.520	.393	.520
26	.256	.114		.125	.679	.324	.616	.789	.766	.559	.365	.275	.372
27	.429	.213		.217	1.051	.542	1.898	2.090	1.314	.864	.478	.375	.489
28	.362	.175		.181	.943	.462	.659	1.088	1.317	.765	.404	.285	.360
29	.238	.102		.123	.595	.296	.775	.772	.655	.501	.353	.282	.380
30	.432	.218		.219	1.646	.483	.596	.944	2.138	.834	.392	.307	.358
31	.431	.227		.249	.957	.558	.615	.925	1.483	.891	.530	.389	.482

Table VI. Concluded

$[N_{St,\infty} \times 10^3]$

Test	QLS62	QLS64	QLS65	QLS66	QLS67	QLS68	QLS72	QLS73	QLS74	QLS75	QLS78	QUS58
Blunt leading edge without flow trips												
1	0.144	0.137	0.212	0.168		0.269	0.046	0.221	0.239	0.288	0.162	0.193
2	.401	.292	.659	.431	0.273	.445	.124	.772	.788	.629	.384	.167
3	1.294	1.221	1.956	1.507	1.140	1.690	.576	2.632	2.606	2.283	1.831	.618
4	.299	.182	.431	.279	.194	.262	.065	.448	.435	.348	.196	.161
5	.419	.296	.698	.416	.252	.380	.121	.794	.729	.541	.366	.208
6	845	.613	1.532	.851	.409	.791	.293	1.829	1.700	1.214	.906	.367
7	.523	.455	.829	.510	.335	.482	.185	.951	.888	.664	.561	.281
8	.832	.669	1.389	.836	.532	.801	.299	1.676	1.539	1.149	.918	.393
9	1.426	1.180	2.590	1.408	.831	1.335	.591	3.267	2.807	1.968	1.782	.640
10	.793	1.842	1.034	.810	.677	.905	.816	1.557	1.083	1.063	1.986	.457
11	.940	.221	.744	.993	.641	.972	.131	.782	1.301	1.306	.387	.475
12	.818	1.477	1.317	.911	.722	.976	.613	1.790	1.428	1.192	1.814	.544
13	.794	.460	1.232	.827	.532	.809	.230	1.487	1.488	1.160	.782	.371
14	.849	.225	.576	.994	1.302	.999	.103	.606	1.109	1.234	.343	.454
Sharp leading edge with flow trips												
15	0.167	0.157	0.268	0.164	0.088	0.152	0.109	0.339	0.307	0.231	0.247	0.079
16	.590	.455	1.212	.613	.322	.585	.322	1.537	1.426	.960	.763	.225
17	.464	.465	.683	.443	.262	.393	.271	.820	.718	.547	.633	.218
18	.704	.622	1.159	.666	.383	.621	.368	1.367	1.269	.943	.881	.304
19	1.103	.938	2.067	1.048	.581	.953	.618	2.586	2.248	1.543	1.627	.424
20	.681	.629	1.048	.645	.375	.613	.367	1.330	1.177	.876	.855	.305
21	1.662	1.607	3.134	1.580	.883	1.483	1.022	3.890	3.191	2.274	2.530	.657
22	1.074	.846	2.076	1.021	.562	.932	.635	2.680	2.189	1.490	1.742	.400
23	1.004	.757	1.960	.945	.517	.852	.618	2.498	1.982	1.335	1.676	.371
24	.902	.881	1.754	.835	.459	.755	.729	2.060	1.633	1.141	1.584	.340
25	1.073	2.794	1.633	1.250	.920	1.308	1.882	2.344	1.816	1.669	2.834	.608
26	.754	.463	.774	1.099	.796	1.333	.282	1.087	1.965	1.861	.526	.407
27	1.145	1.953	1.983	1.293	.929	1.402	1.284	2.812	2.280	1.885	2.545	.565
28	1.144	.704	1.968	1.146	.671	1.104	.562	2.334	2.308	1.687	1.318	.432
29	.628	.599	.720	.902	.739	1.172	.238	.755	1.384	1.672	.489	.338
30	1.864	.558	1.053	1.994	.818	2.014	.371	.736	1.298	2.547	.555	.317
31	1.257	.542	2.324	1.198	.770	1.117	.342	1.953	2.429	1.635	.520	1.003

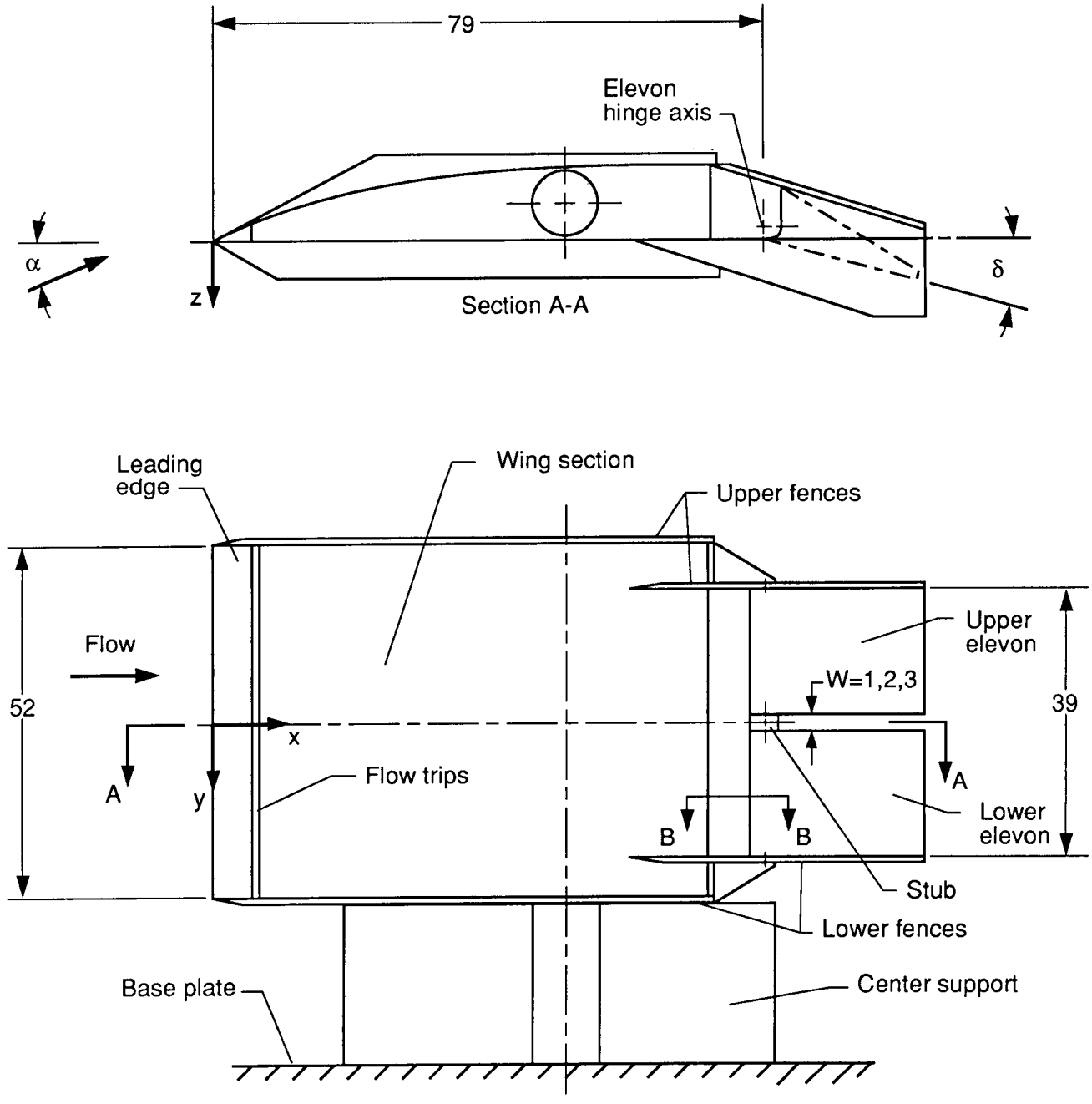

(a) Assembly.

Figure 1. Wing-elevon model. (All dimensions in inches.)

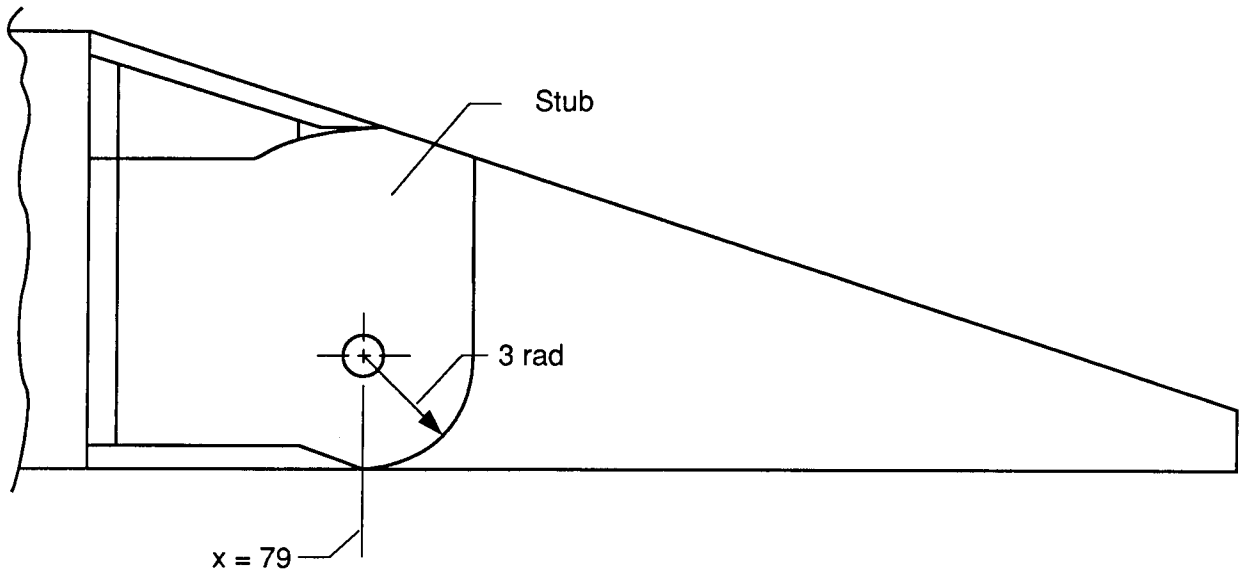

(b) Section AA at stub.

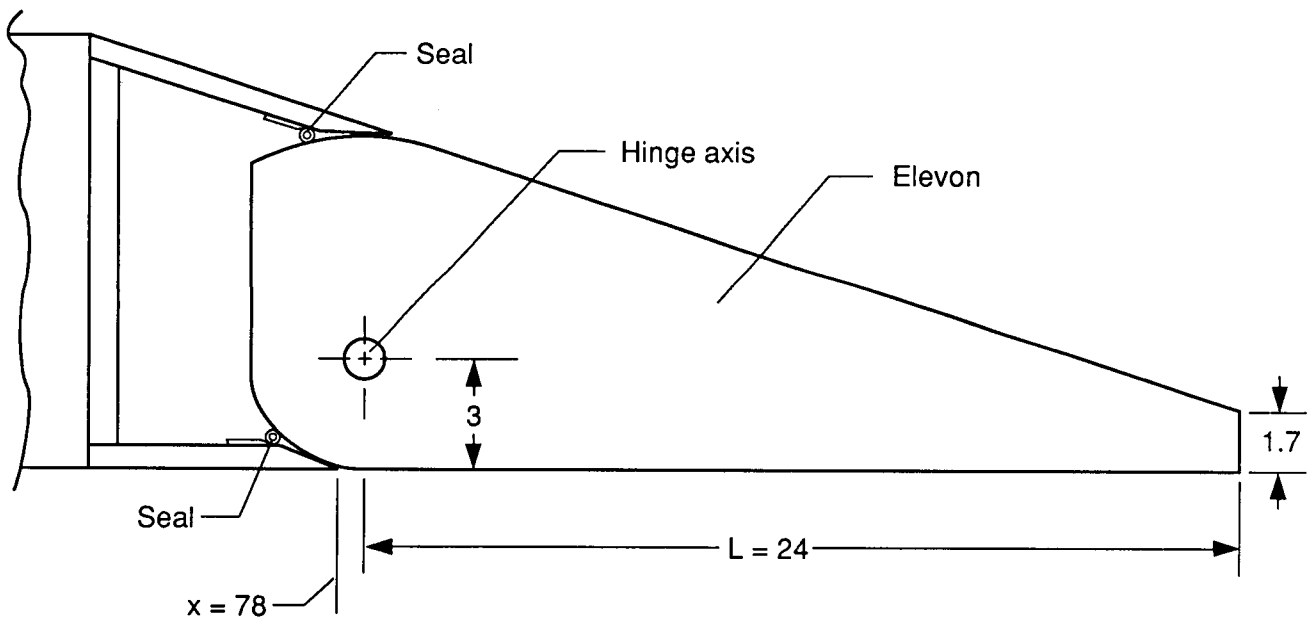

(c) Section BB at elevon midspan.

Figure 1. Concluded.

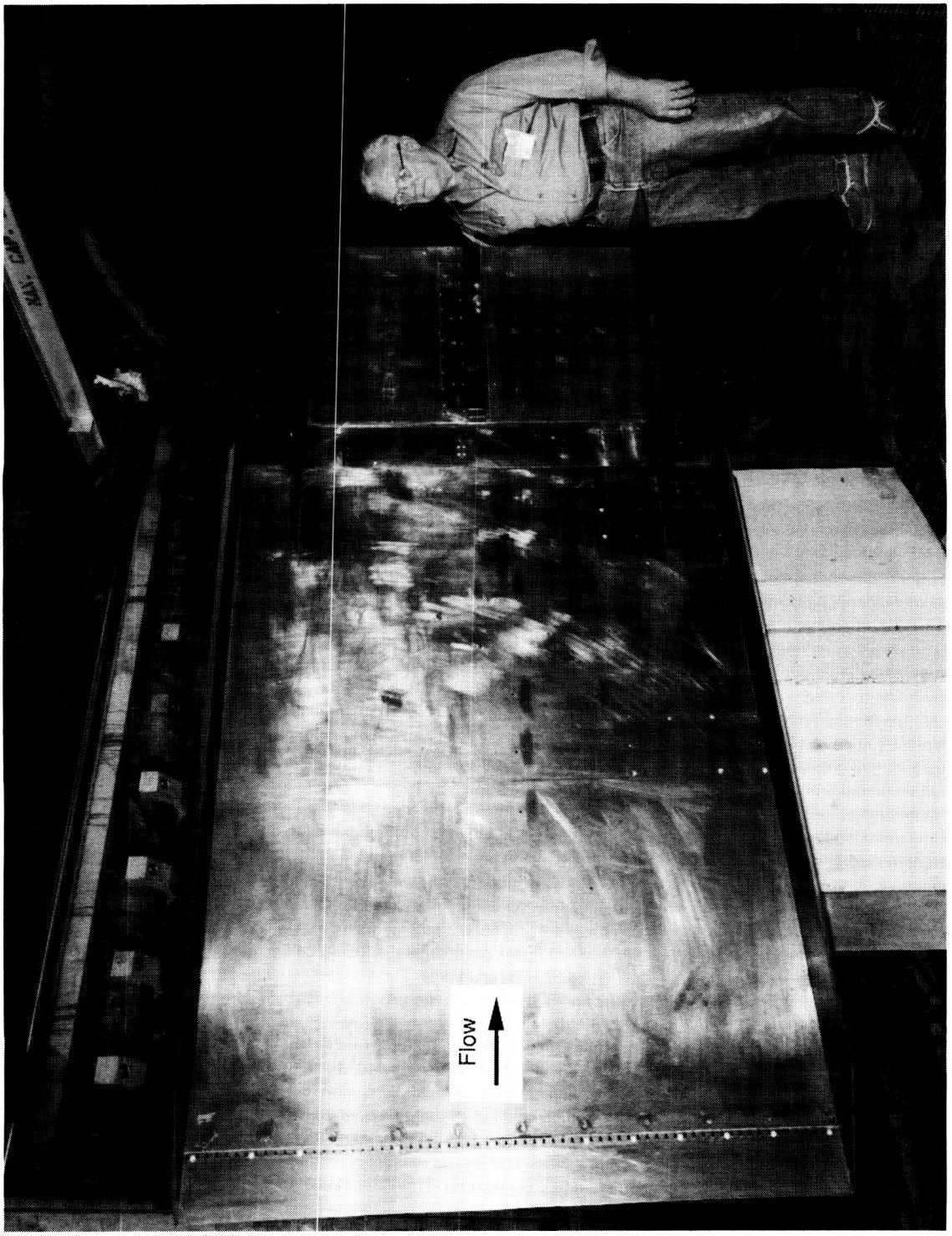

L-84-11,775

(a) Assembled.

Figure 2. Photographs of split elevon model.

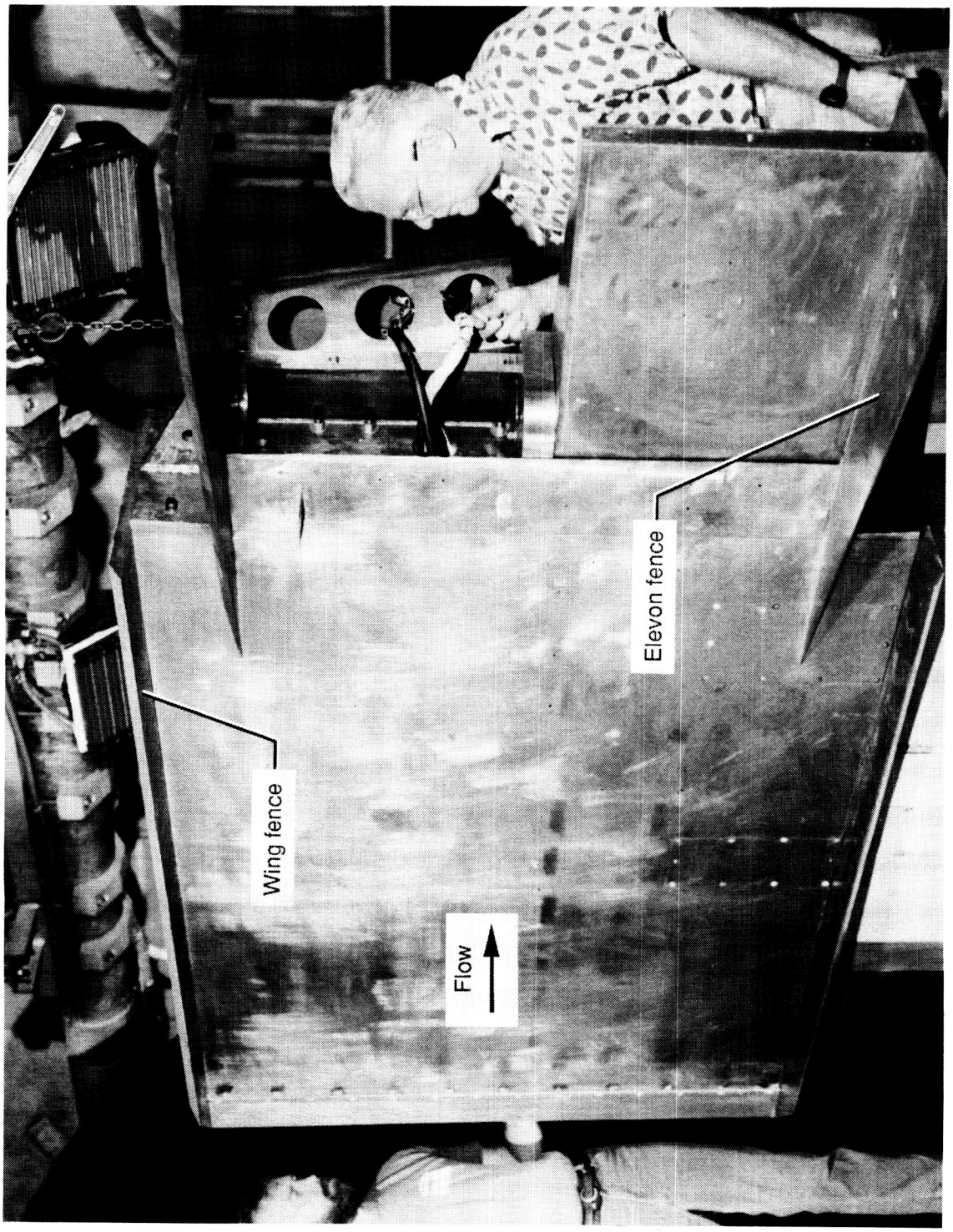

L-84-11,785

(b) Upper elevon removed.

Figure 2. Continued.

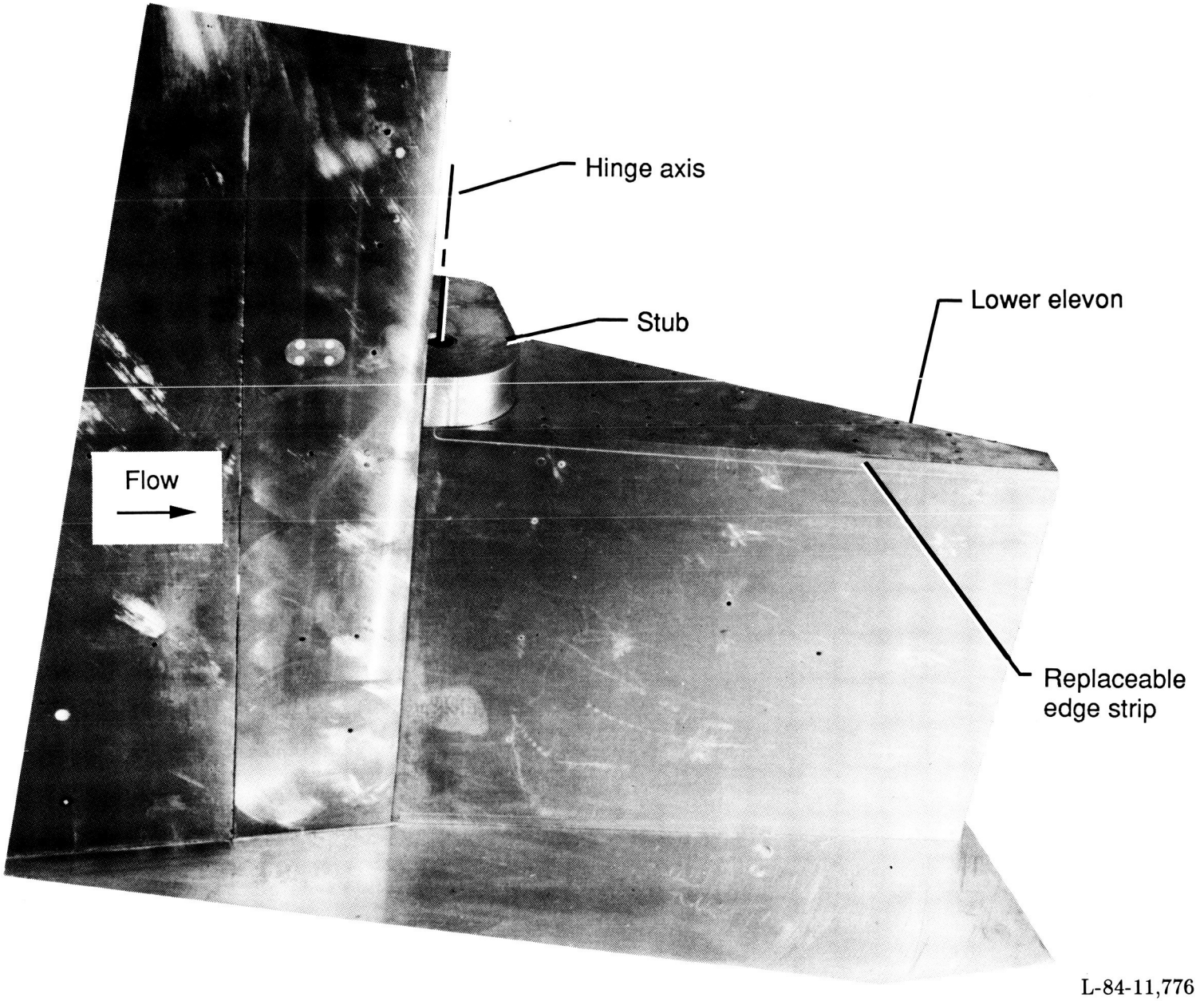

(c) Lower elevon.

Figure 2. Concluded.

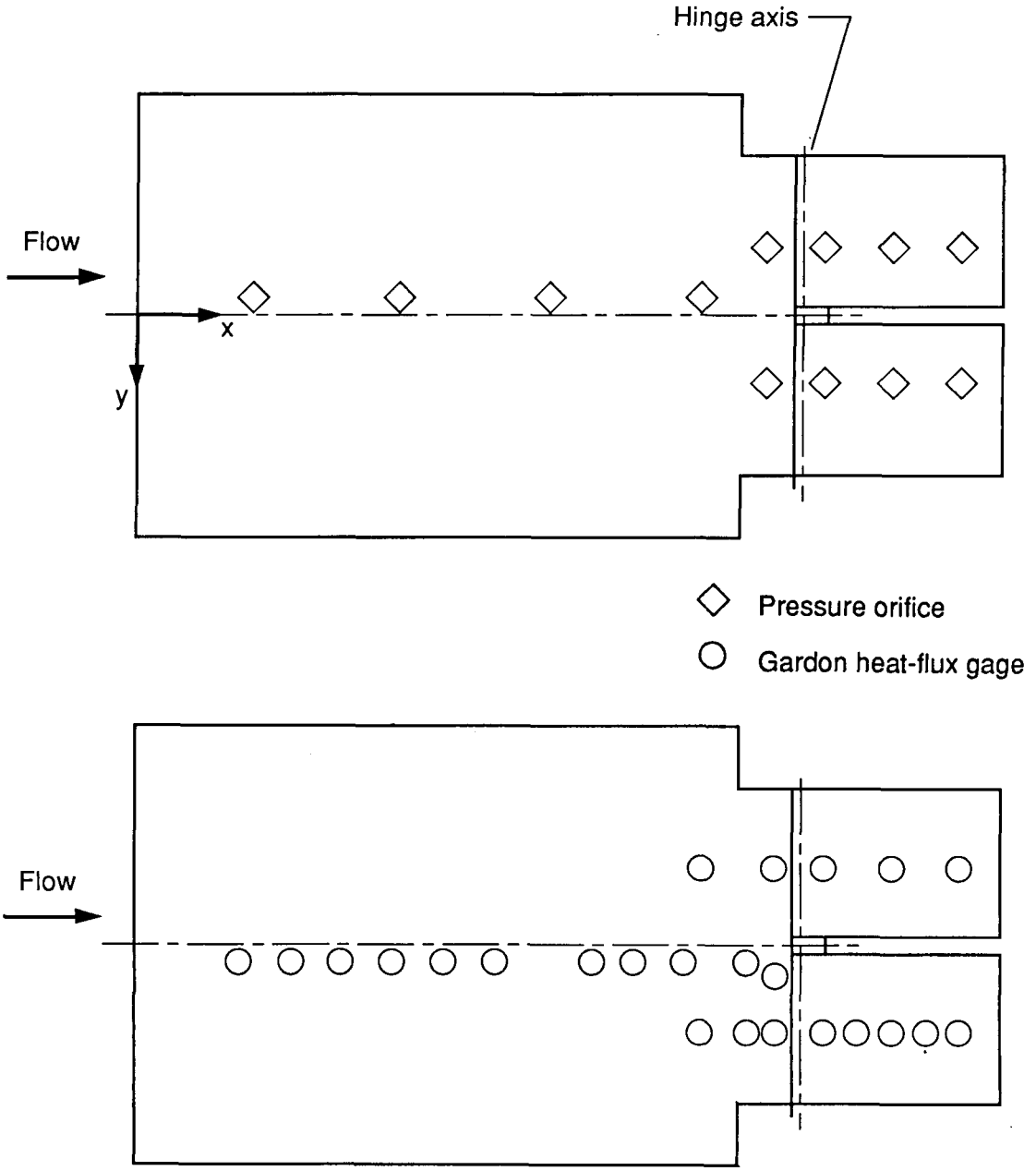

(a) Windward locations of longitudinal plots.

Figure 3. Locations of wing and elevon instrumentation.

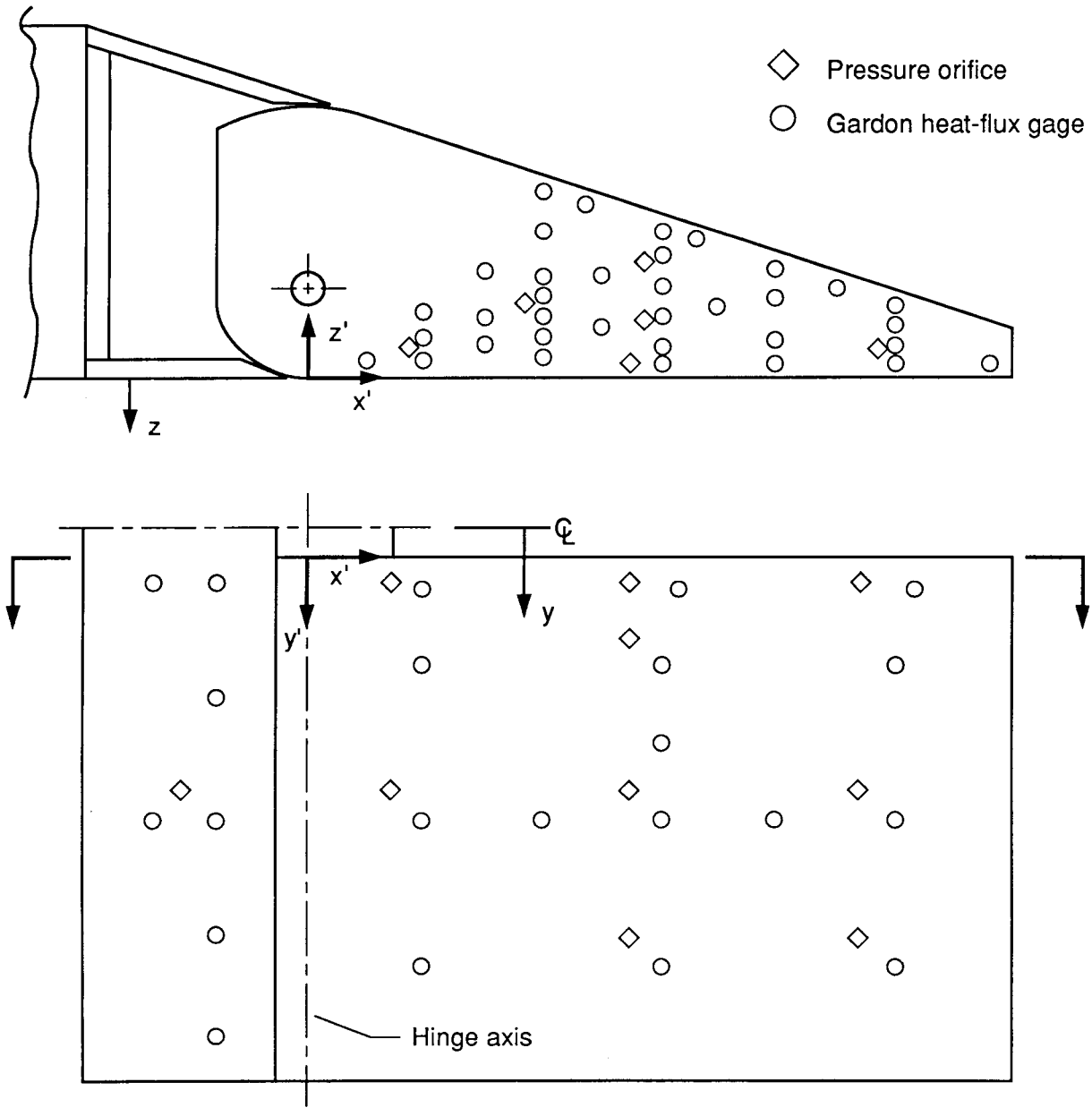

(b) Lower elevon.

Figure 3. Continued.

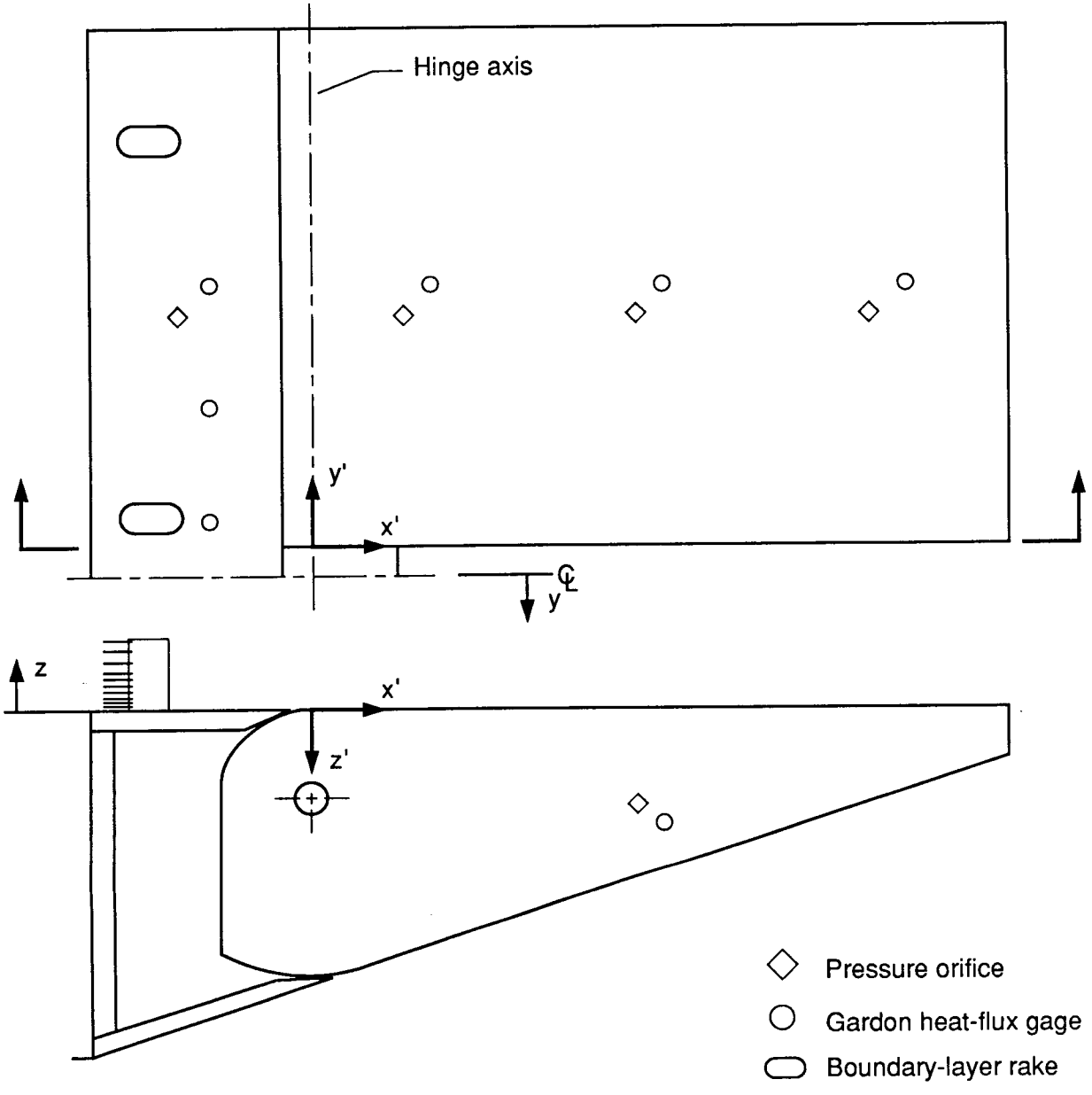

(c) Upper elevon.

Figure 3. Concluded.

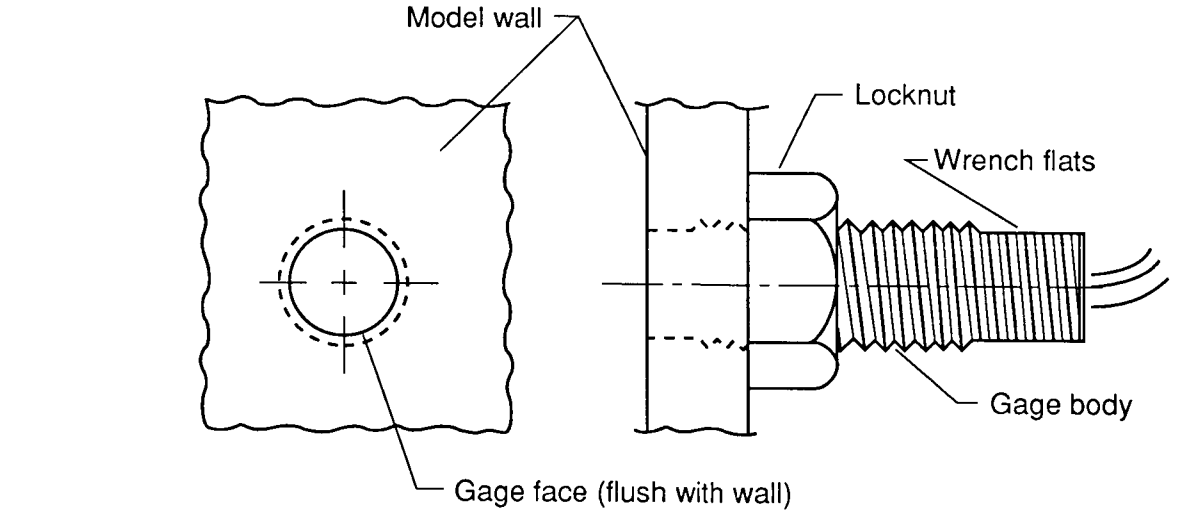

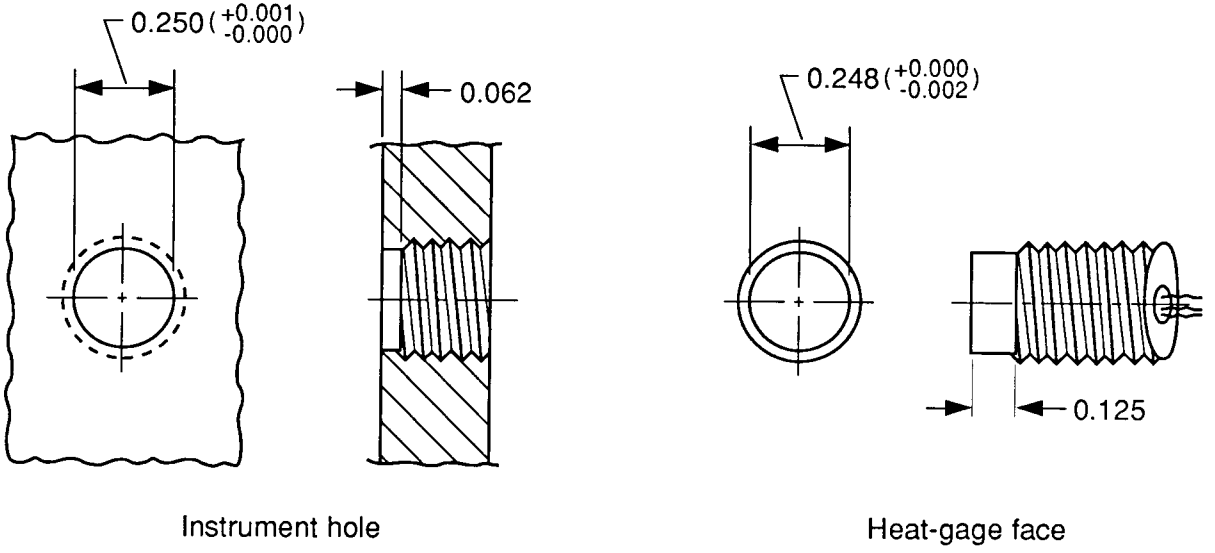

(a) Gardon gage.

Figure 4. Instrument installation details. (All dimensions in inches.)

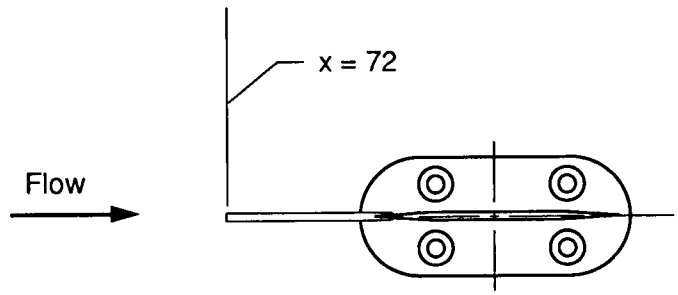

Probe	z, in.
1	0.032
2	.096
3	.160
4	.224
5	.288
6	.416
7	.544
8	.673
9	.800
10	.928
11	1.120
12	1.440
13	2.000
14	2.500

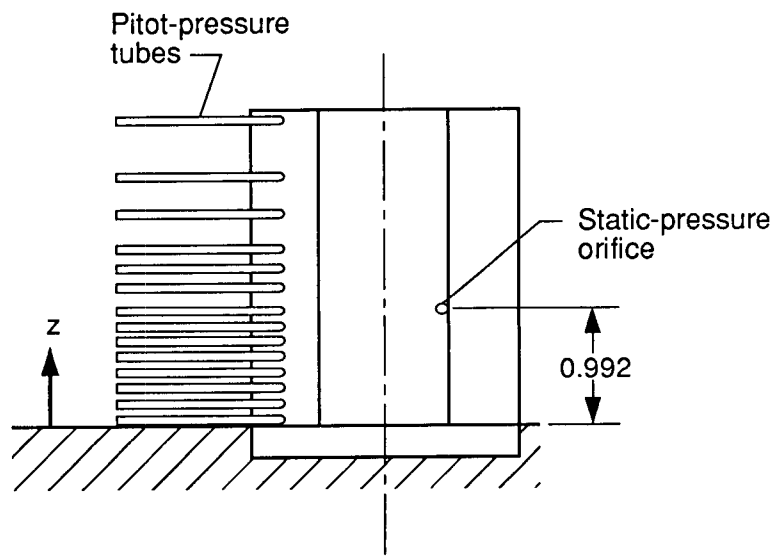

(b) Boundary-layer rake.

Figure 4. Concluded.

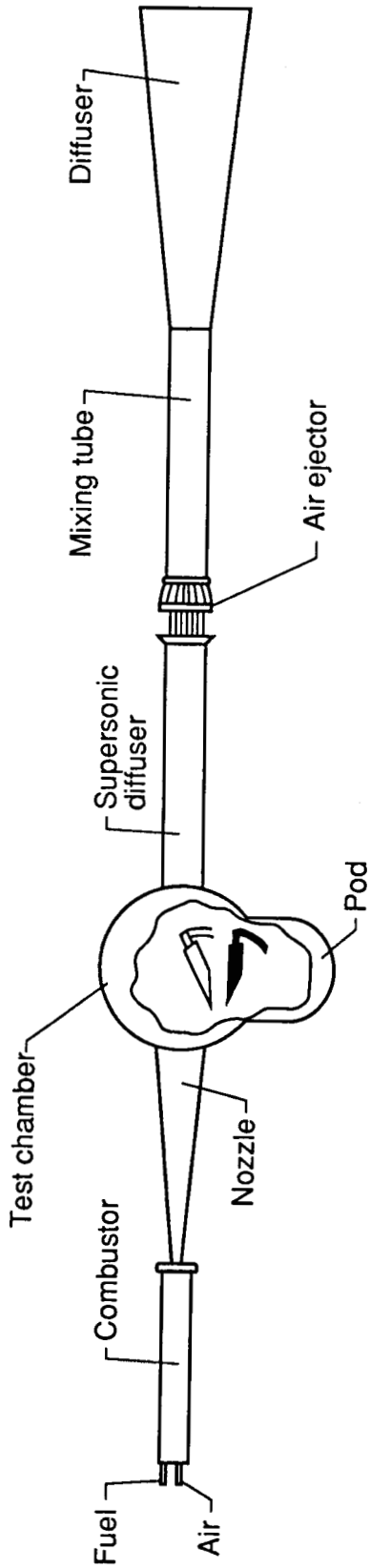

Figure 5. Langley 8-Foot High-Temperature Tunnel.

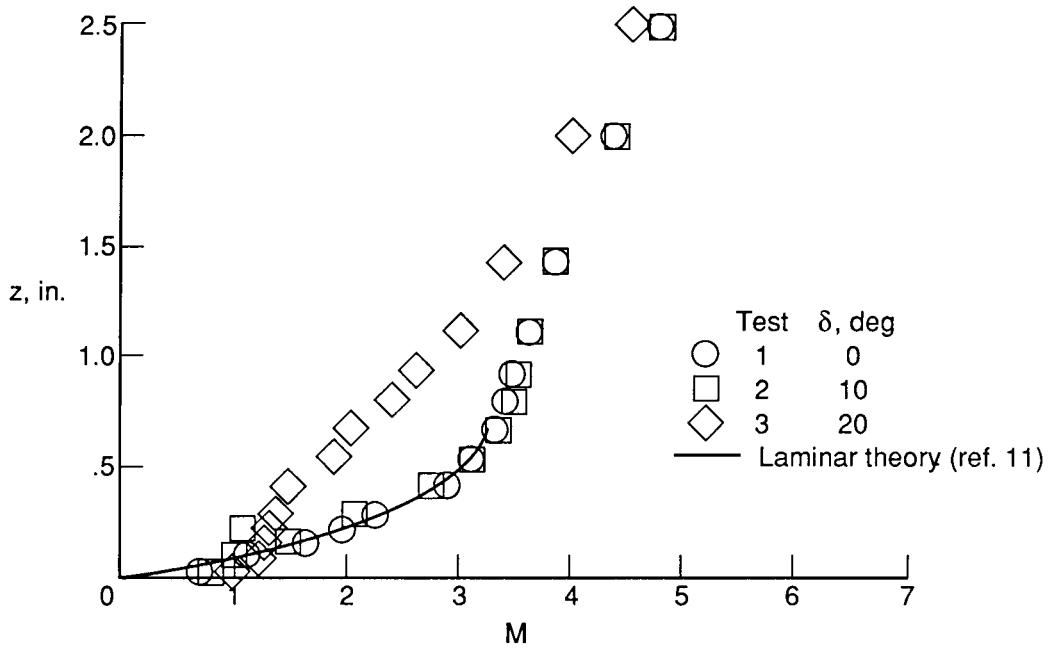

(a) $\alpha = 0°$.

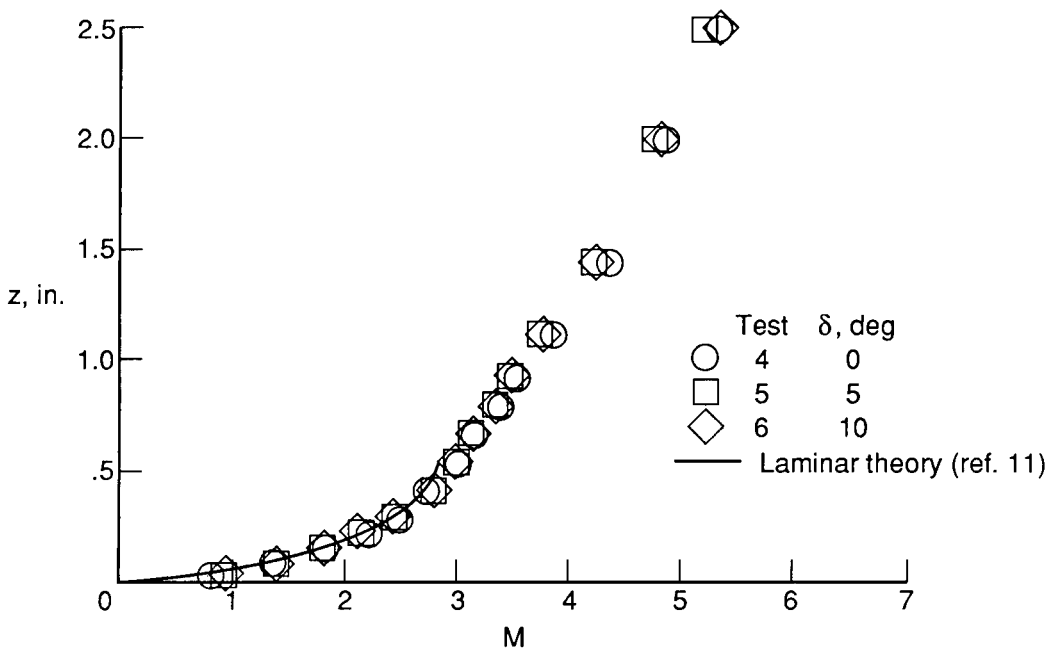

(b) $\alpha = 5°$.

Figure 6. Boundary-layer Mach number profiles for blunt leading edge without flow trips for various wing and elevon angles.

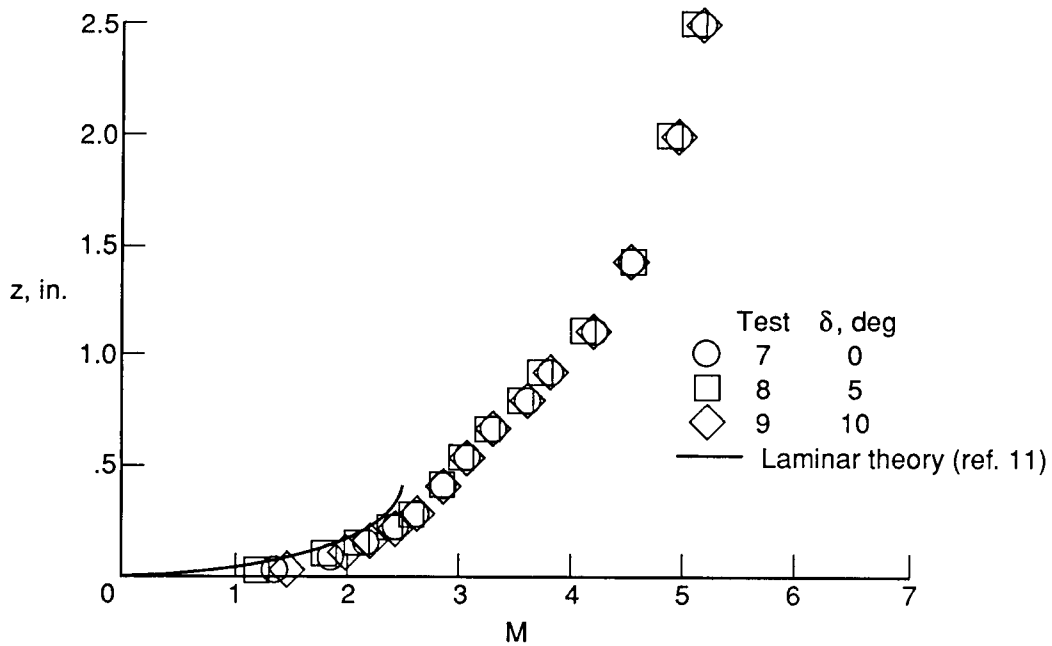

(c) $\alpha = 10°$.

Figure 6. Concluded.

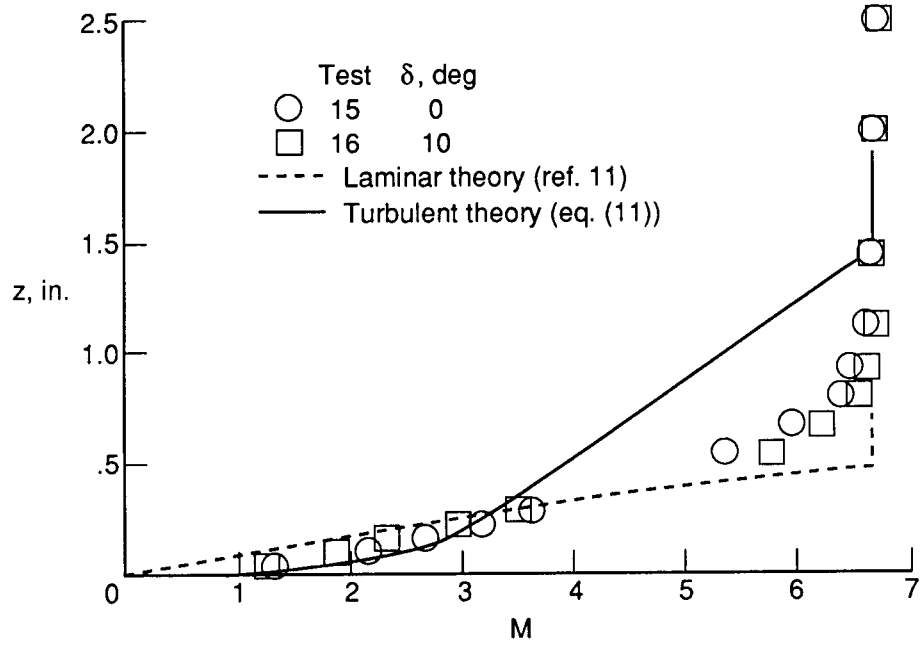

(a) $\alpha = 0°$.

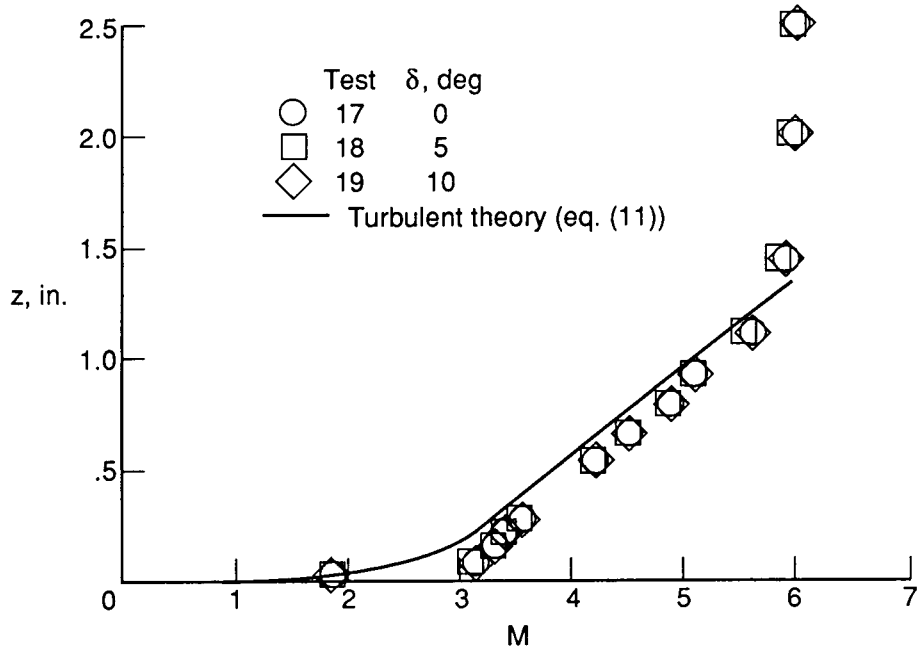

(b) $\alpha = 5°$.

Figure 7. Boundary-layer Mach number profiles for sharp leading edge with flow trips for various wing and elevon angles.

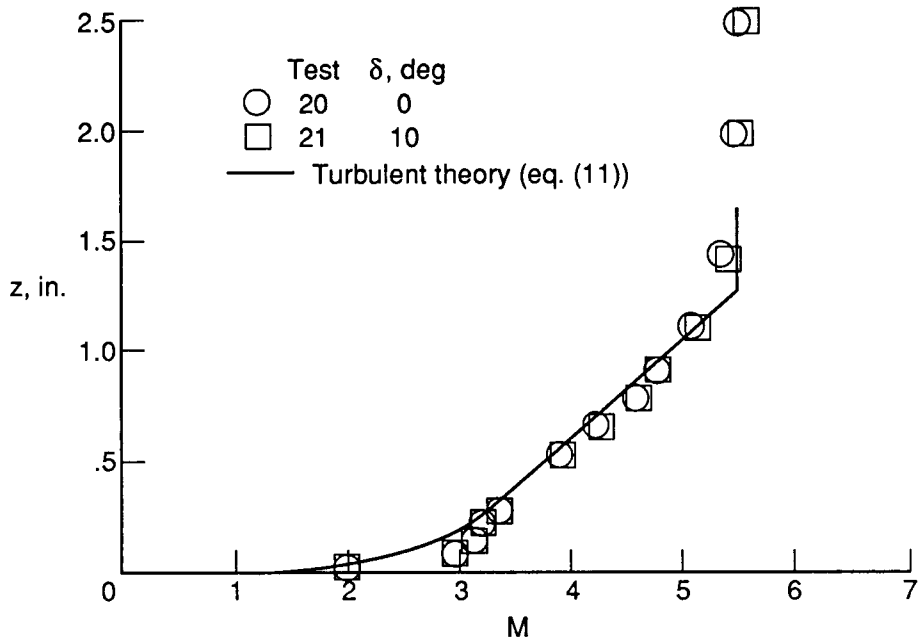

(c) $\alpha = 10°$.

Figure 7. Concluded.

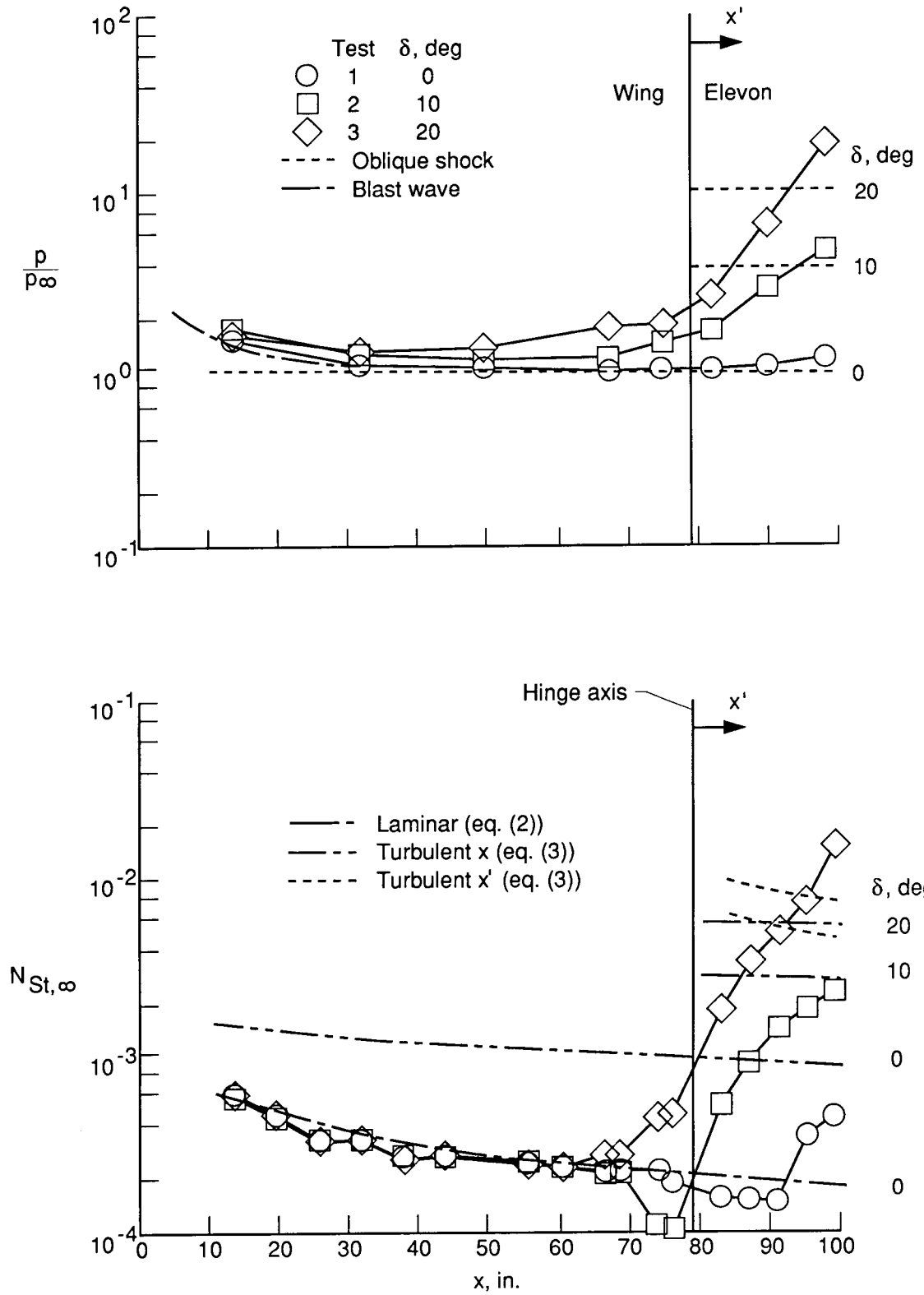

(a) $\alpha = 0°$; longitudinal.

Figure 8. Windward-surface-pressure and heat-transfer distributions for blunt leading edge without flow trips. $W = 2$ in.

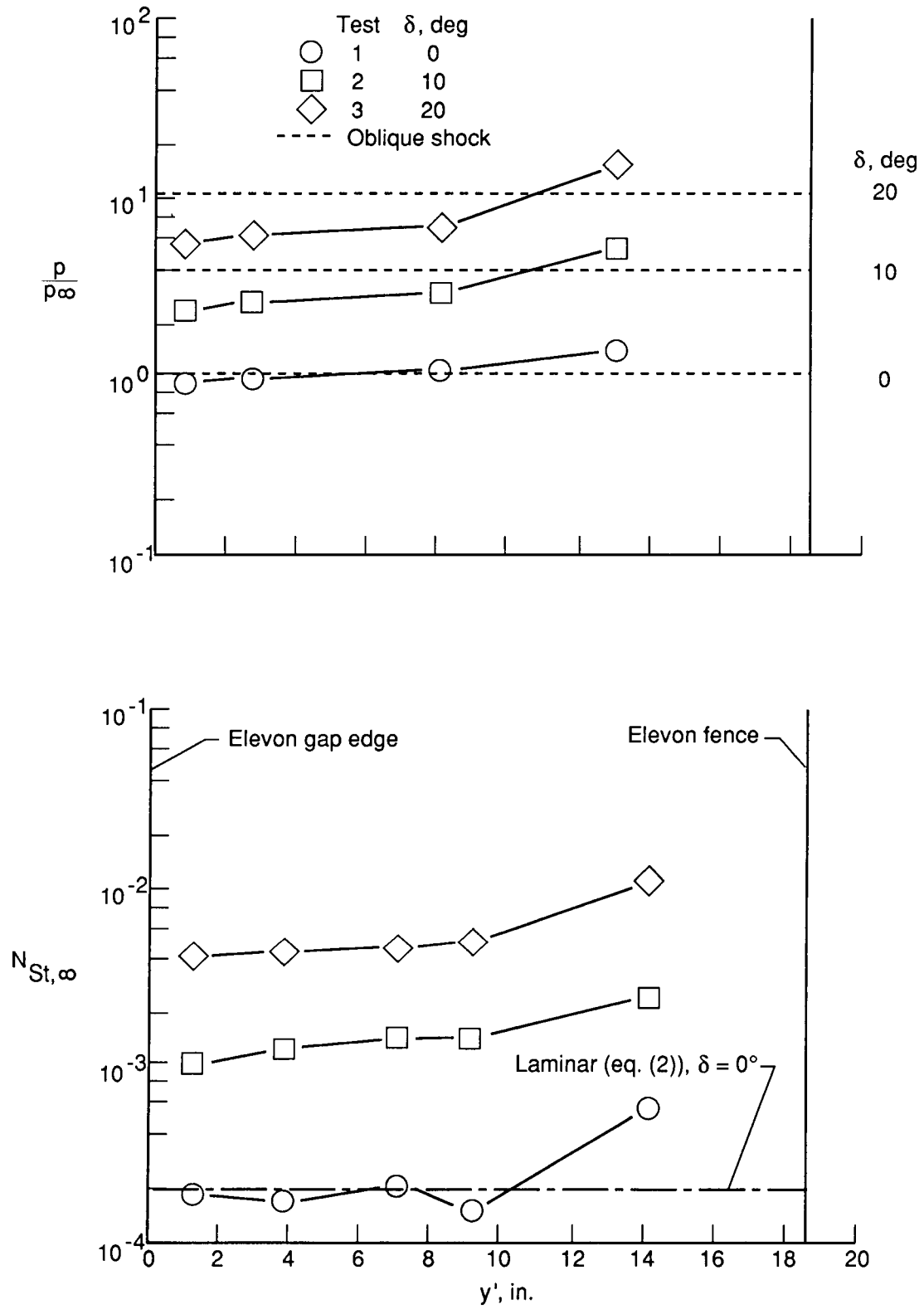

(a) $\alpha = 0°$; lateral; midchord.

Figure 8. Continued.

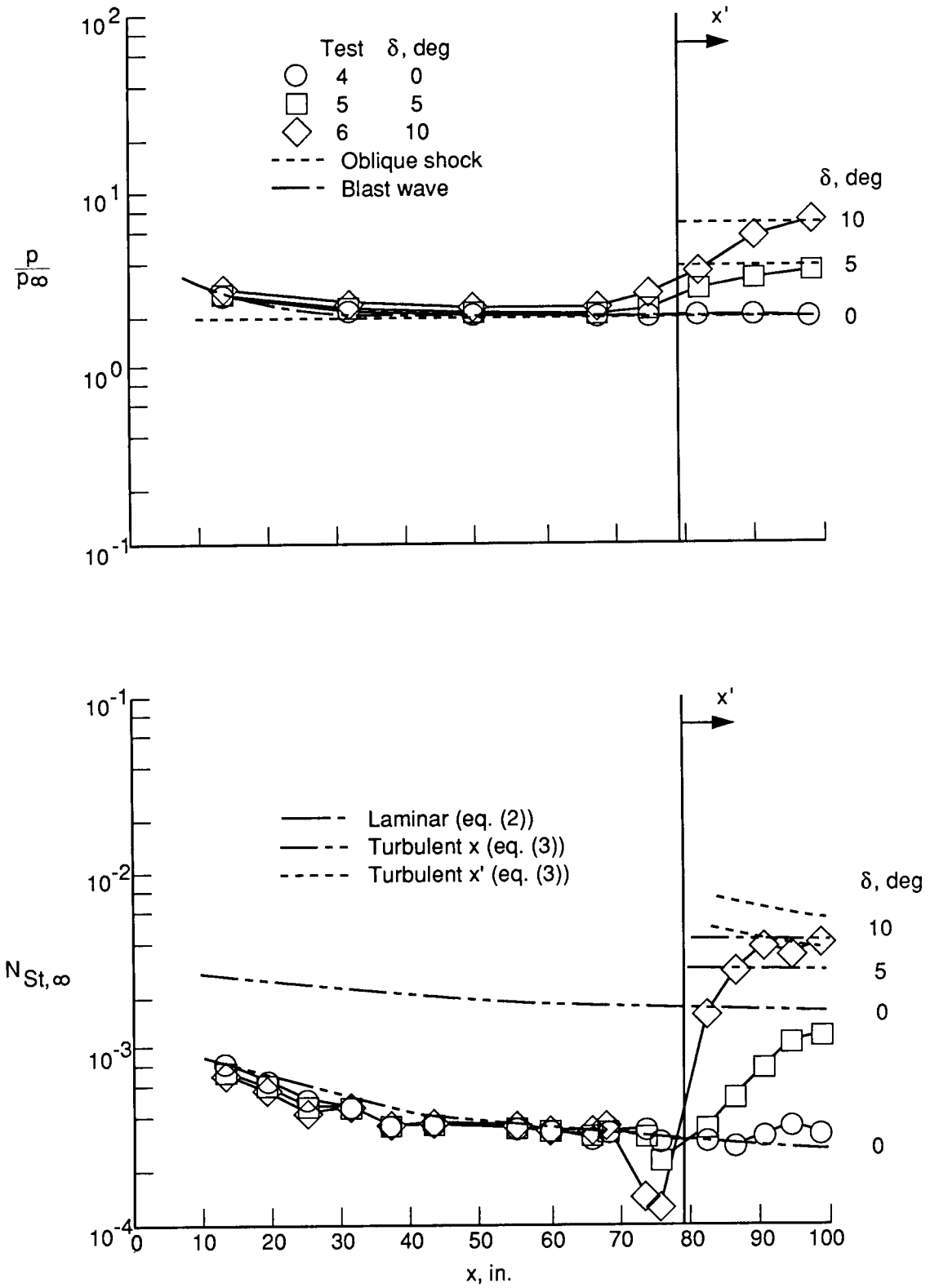

(b) $\alpha = 5°$; longitudinal.

Figure 8. Continued.

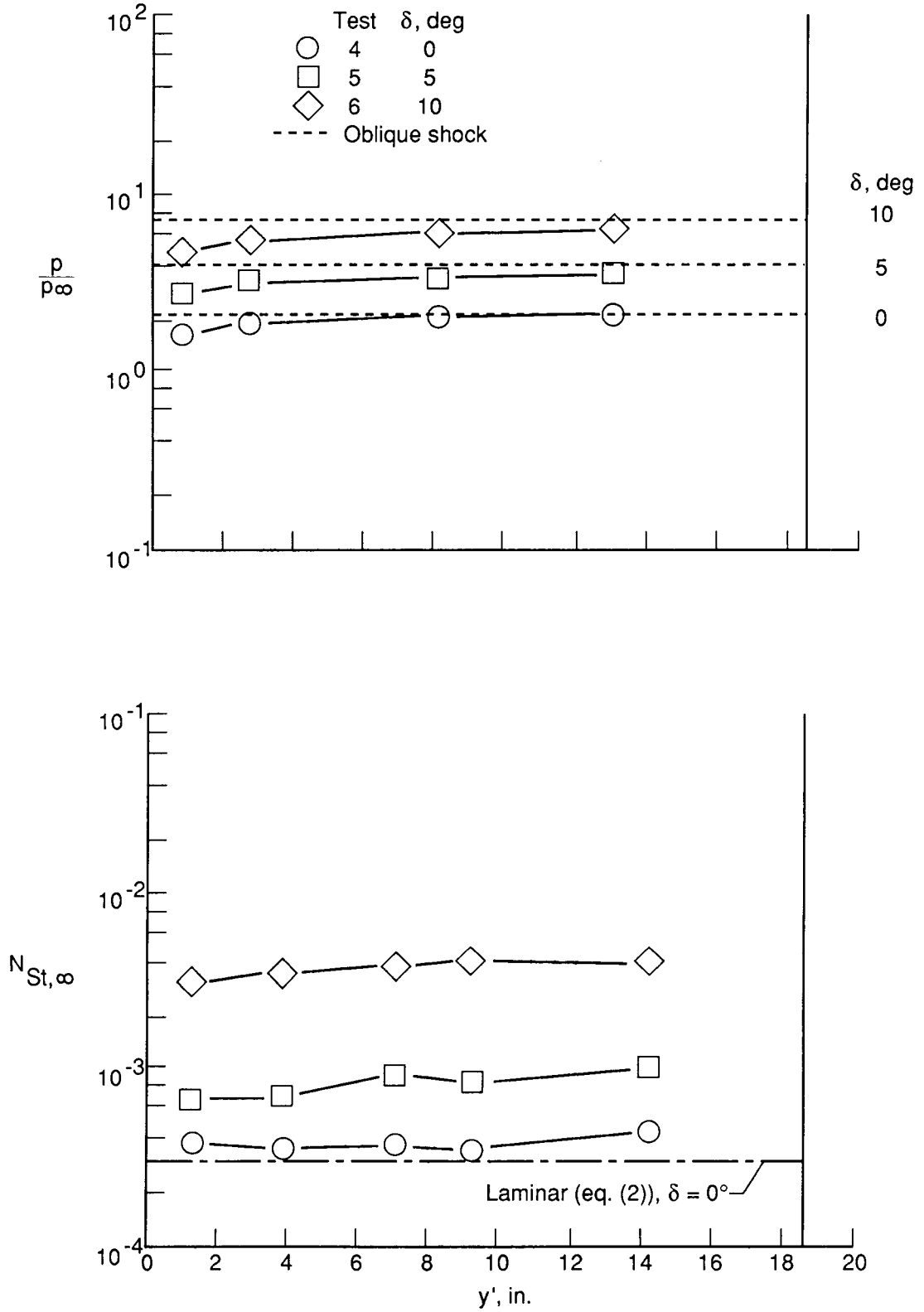

(b) $\alpha = 5°$; lateral; midchord.

Figure 8. Continued.

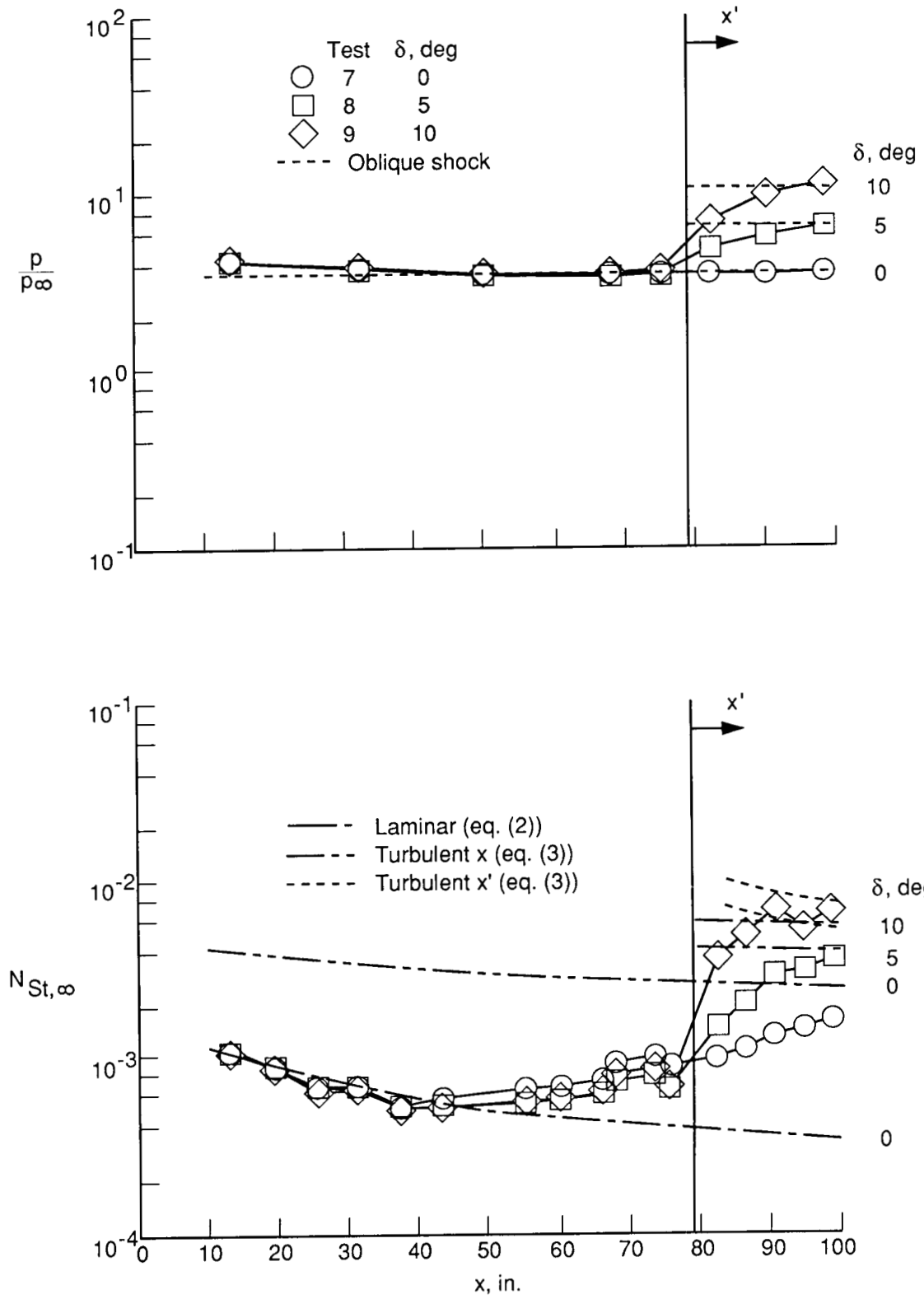

(c) $\alpha = 10°$; longitudinal.

Figure 8. Continued.

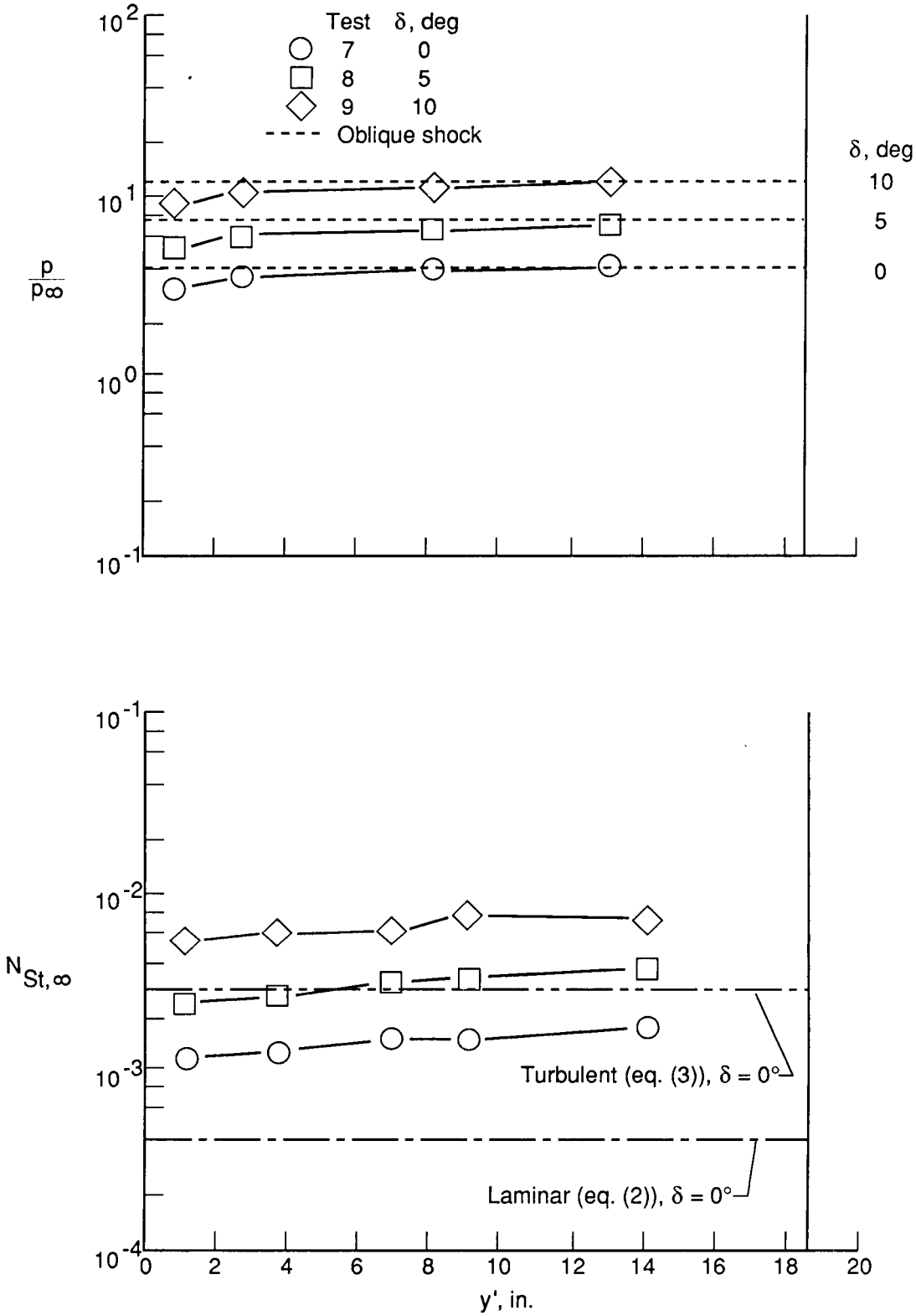

(c) $\alpha = 10°$; lateral; midchord.

Figure 8. Concluded.

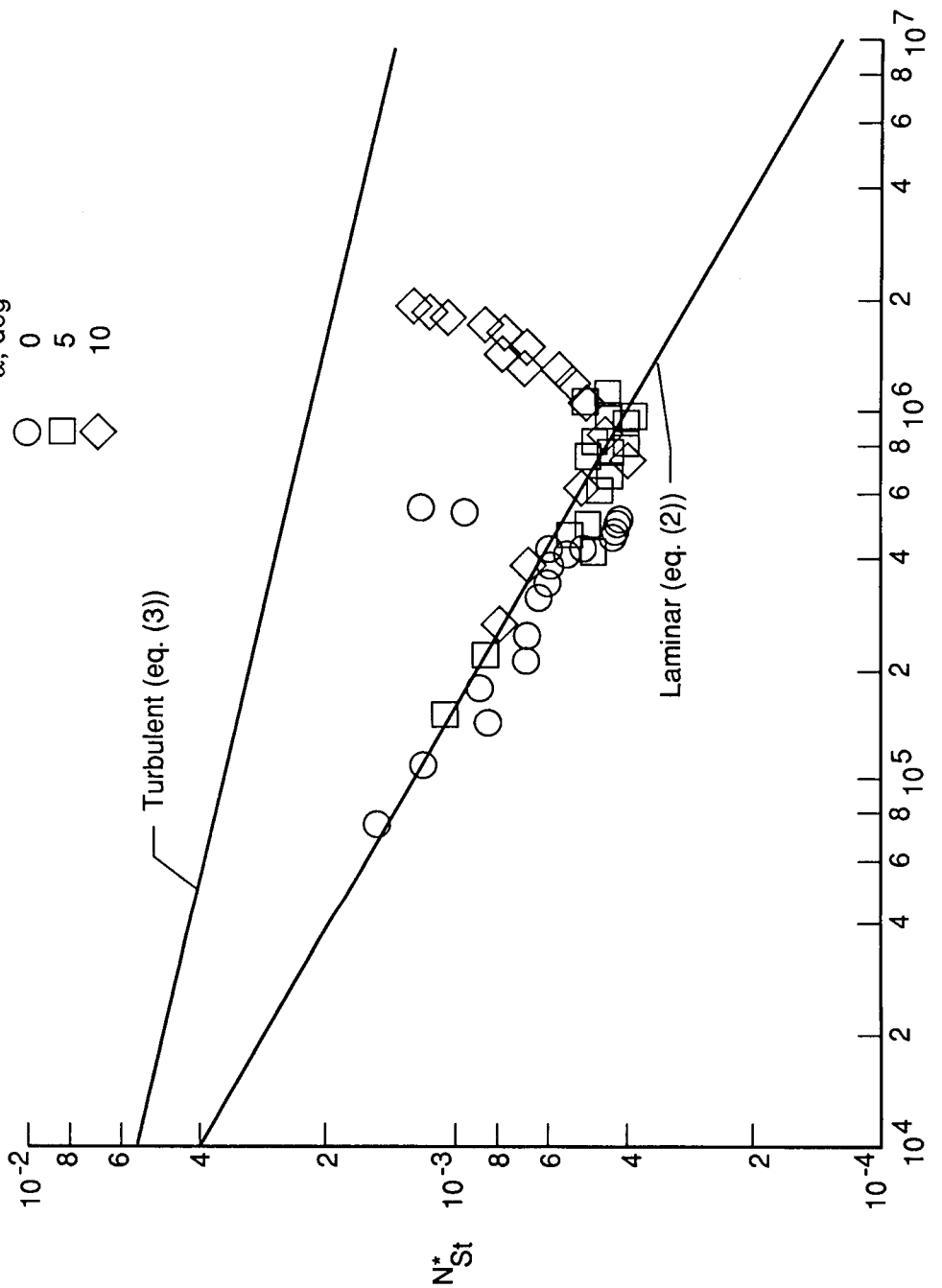

Figure 9. Correlation of wing-elevon heat transfer for blunt leading edge without flow trips. $\delta = 0°$.

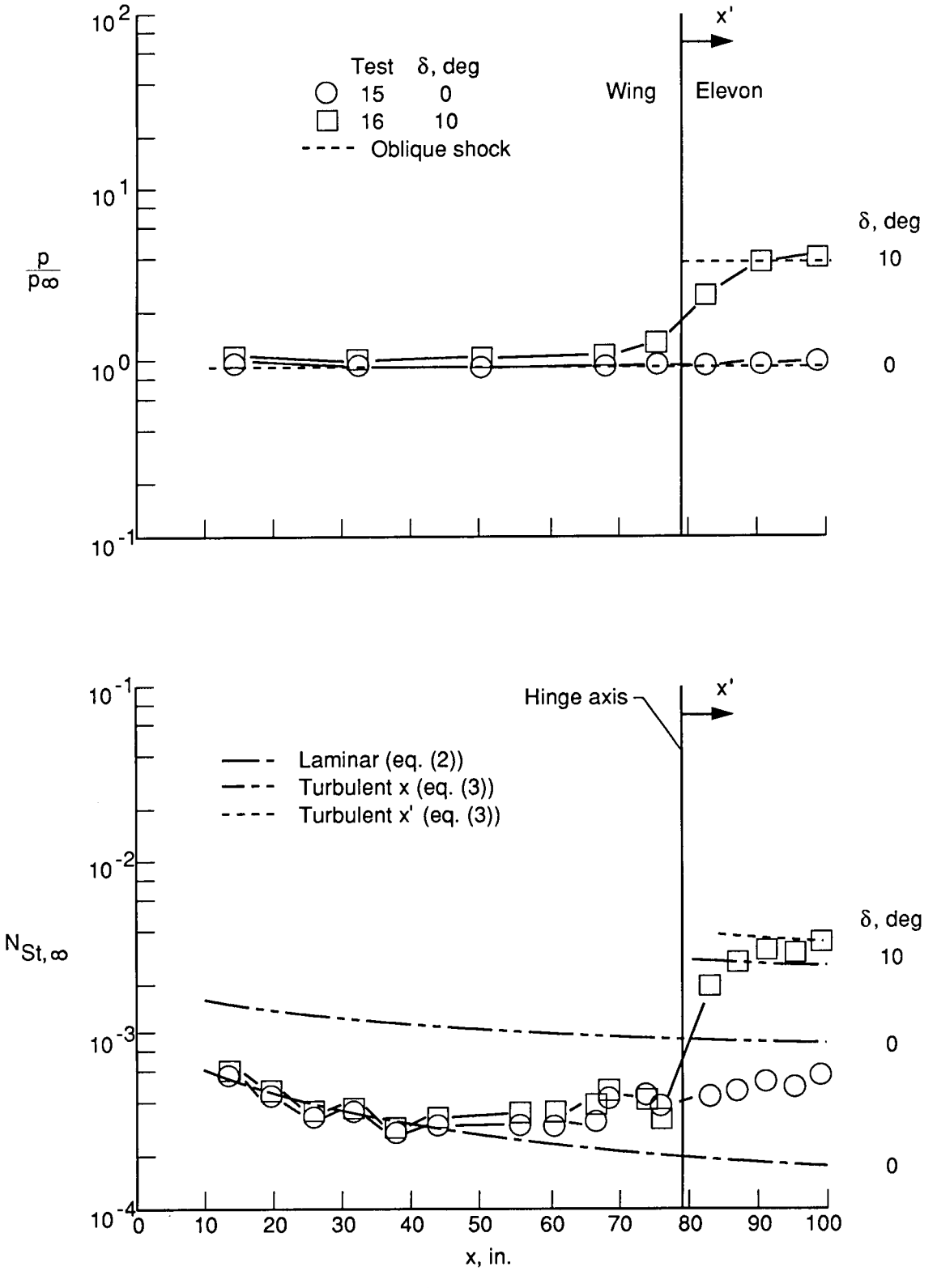

(a) $\alpha = 0°$; longitudinal.

Figure 10. Windward-surface pressure and heat-transfer distributions for sharp leading edge with flow trips. $W = 2$ in.

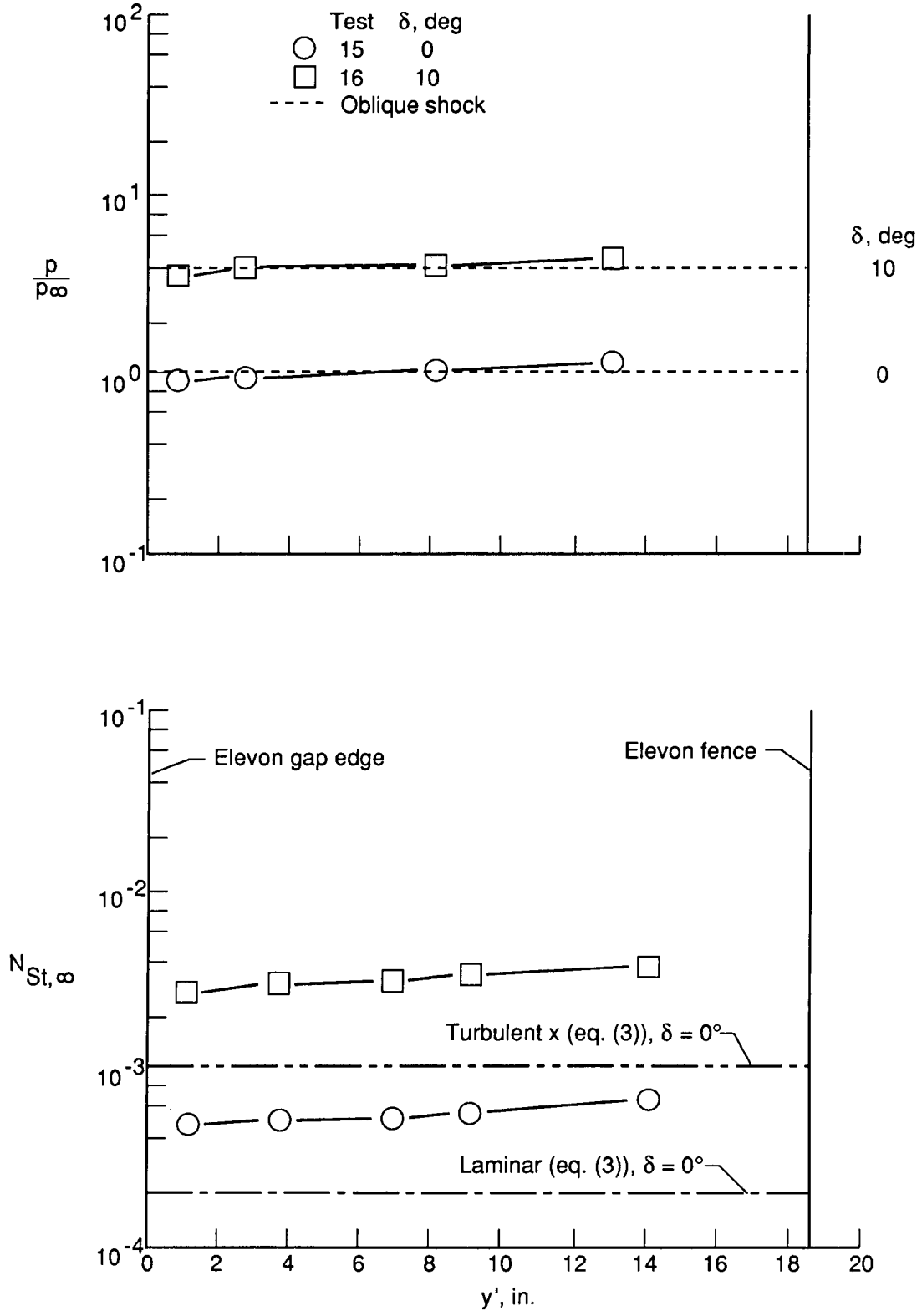

(a) $\alpha = 0°$; lateral; midchord.

Figure 10. Continued.

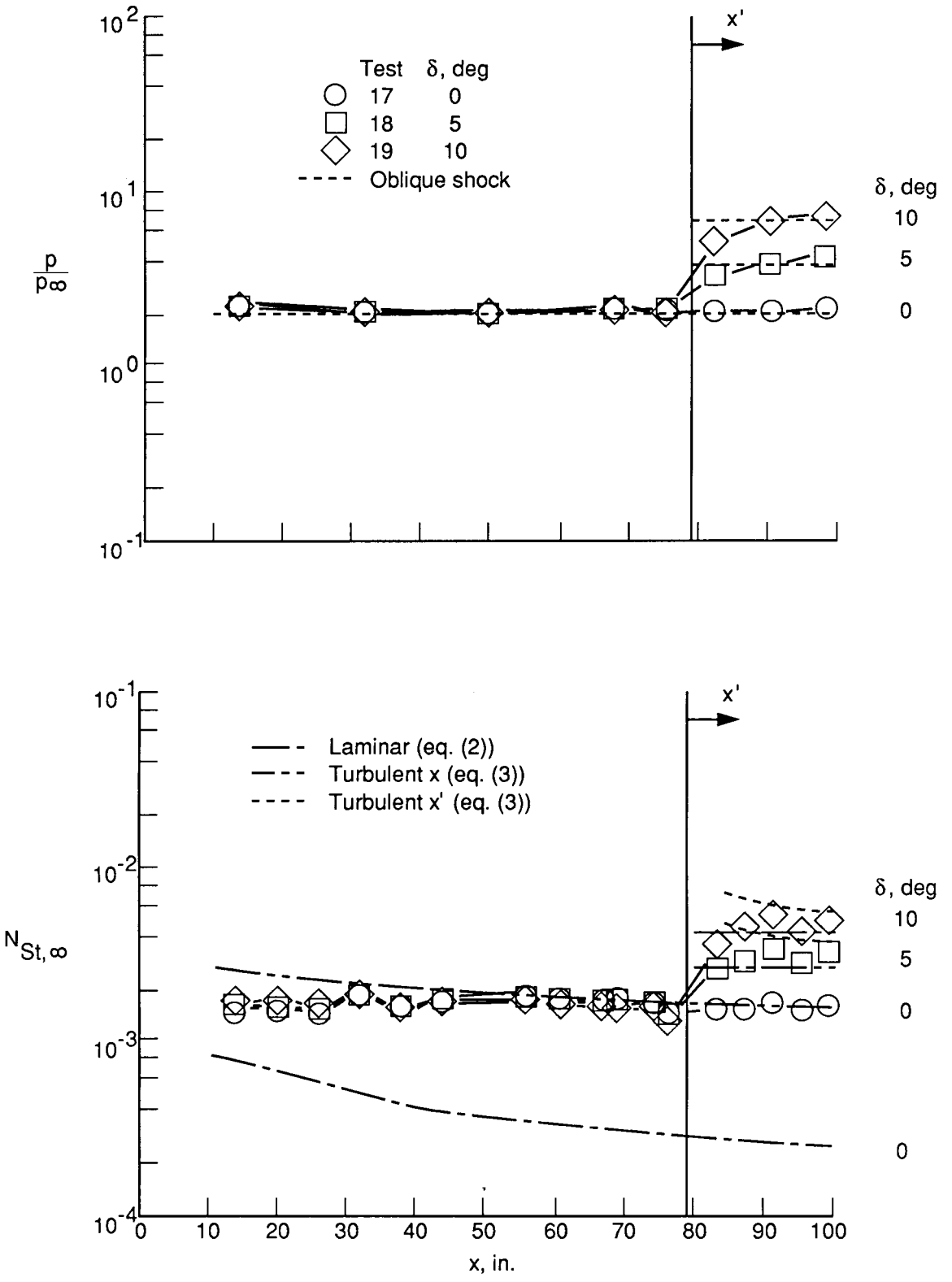

(b) $\alpha = 5°$; longitudinal.

Figure 10. Continued.

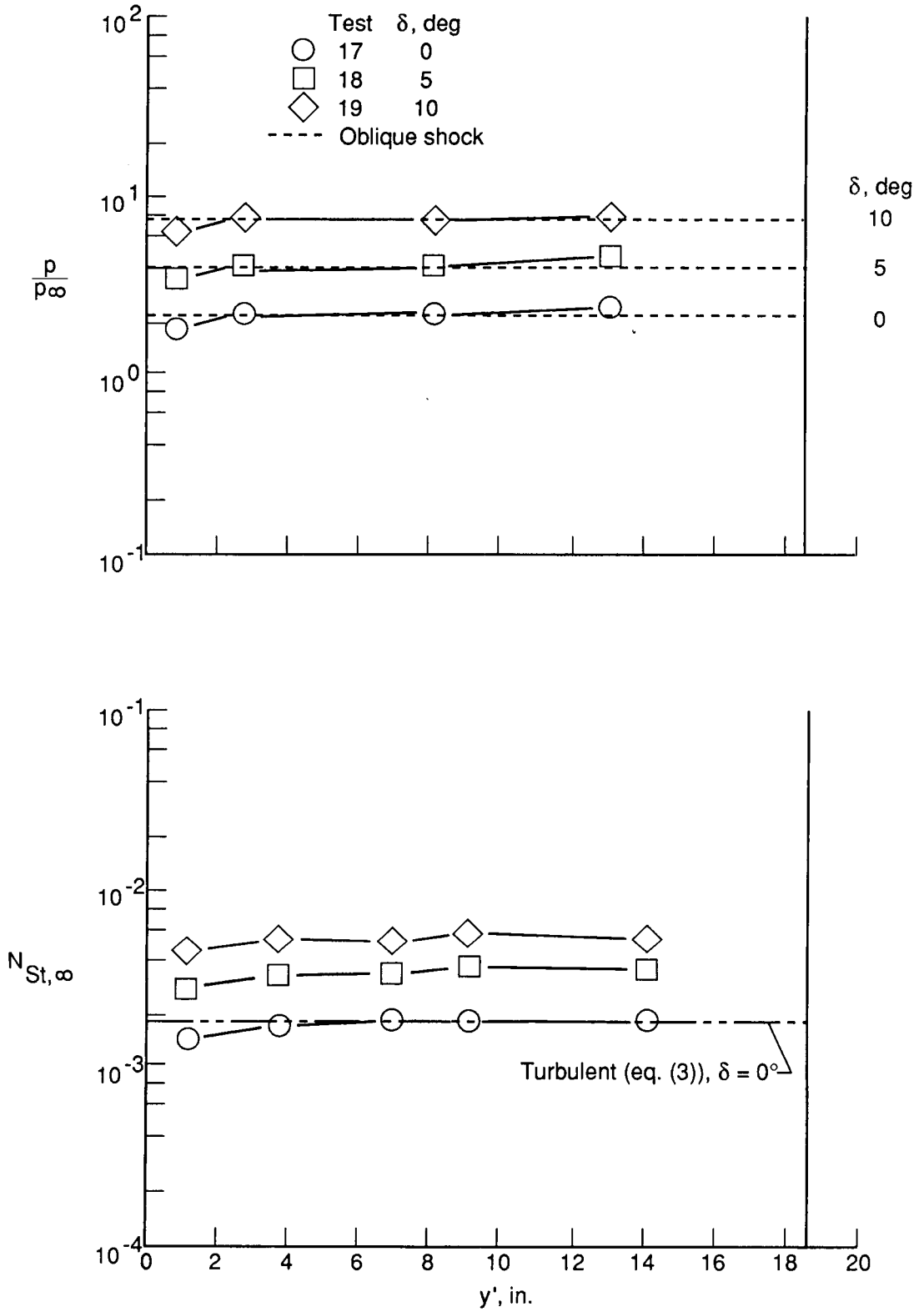

(b) $\alpha = 5°$; lateral; midchord.

Figure 10. Continued.

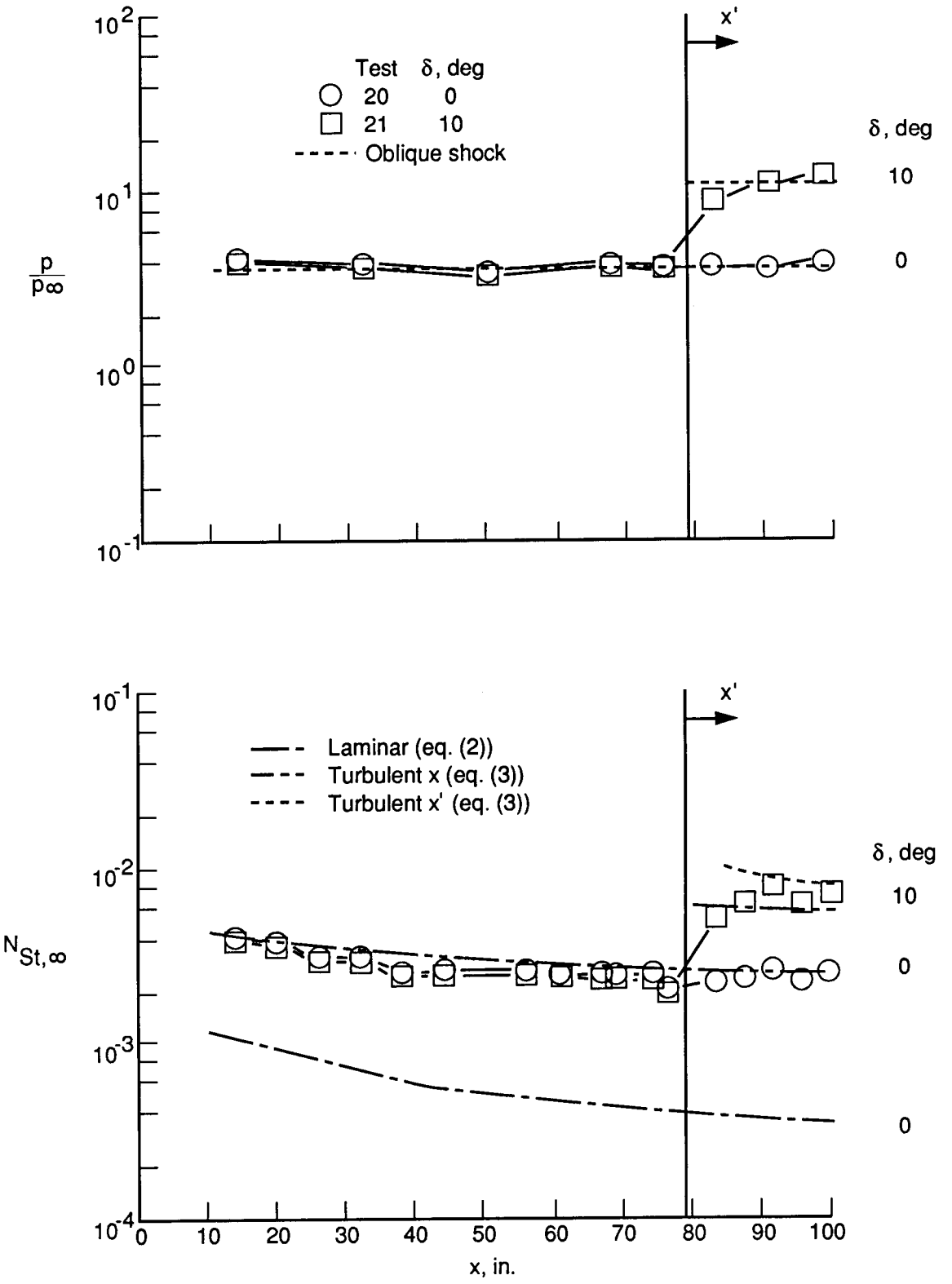

(c) $\alpha = 10°$; longitudinal.

Figure 10. Continued.

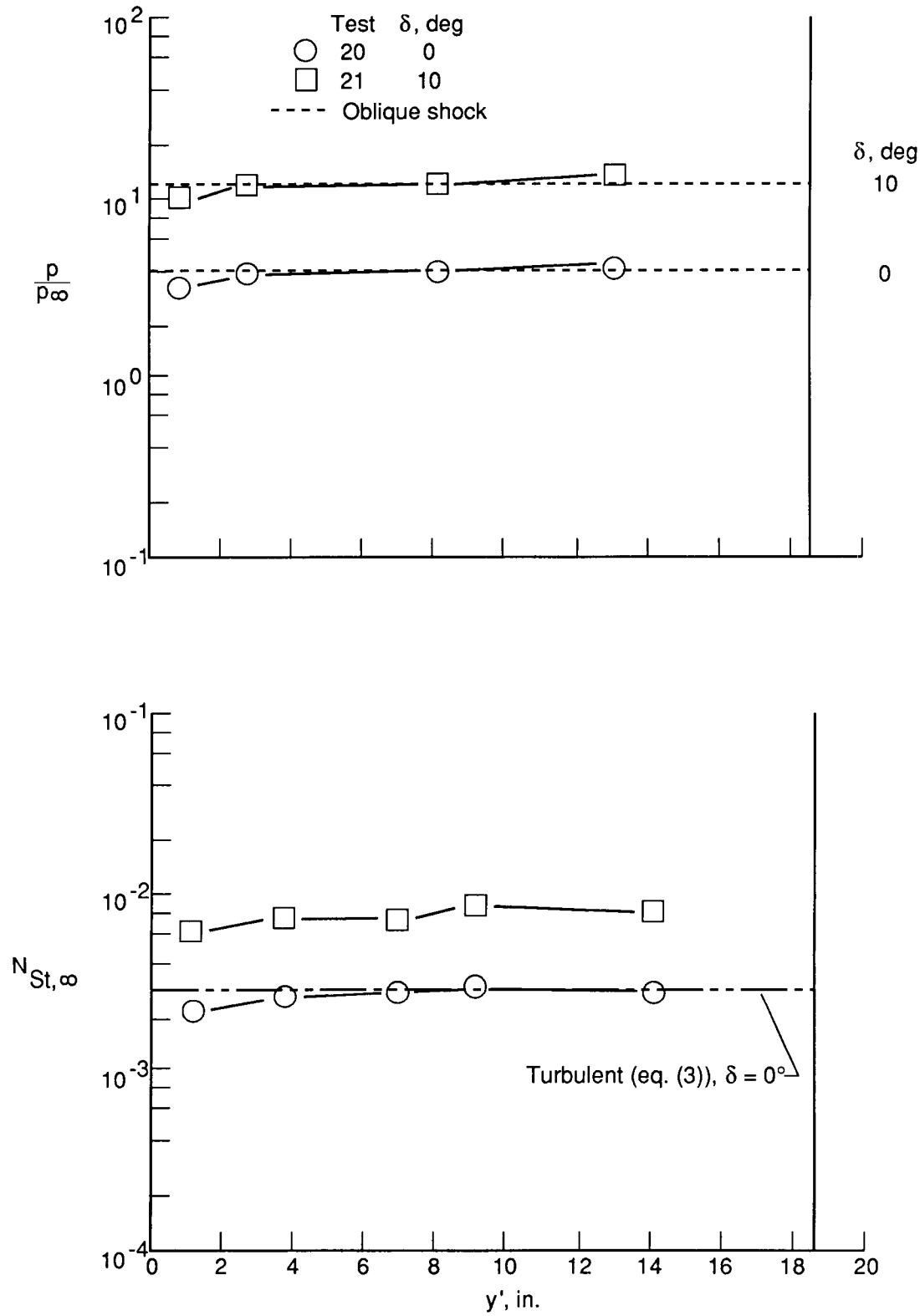

(c) $\alpha = 10°$; lateral; midchord.

Figure 10. Concluded.

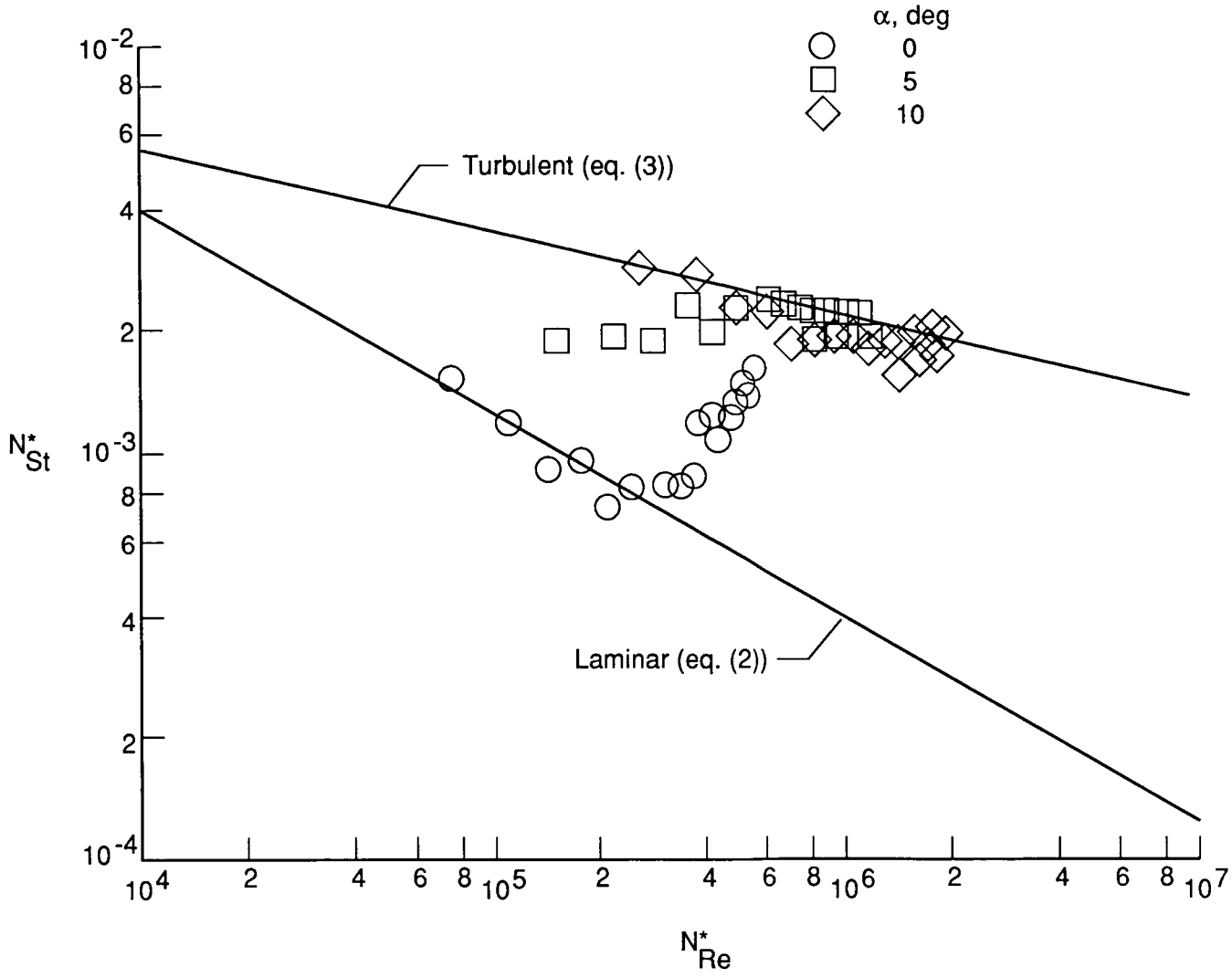

Figure 11. Correlation of wing-elevon heat transfer for sharp leading edge with flow trips. $\delta = 0°$.

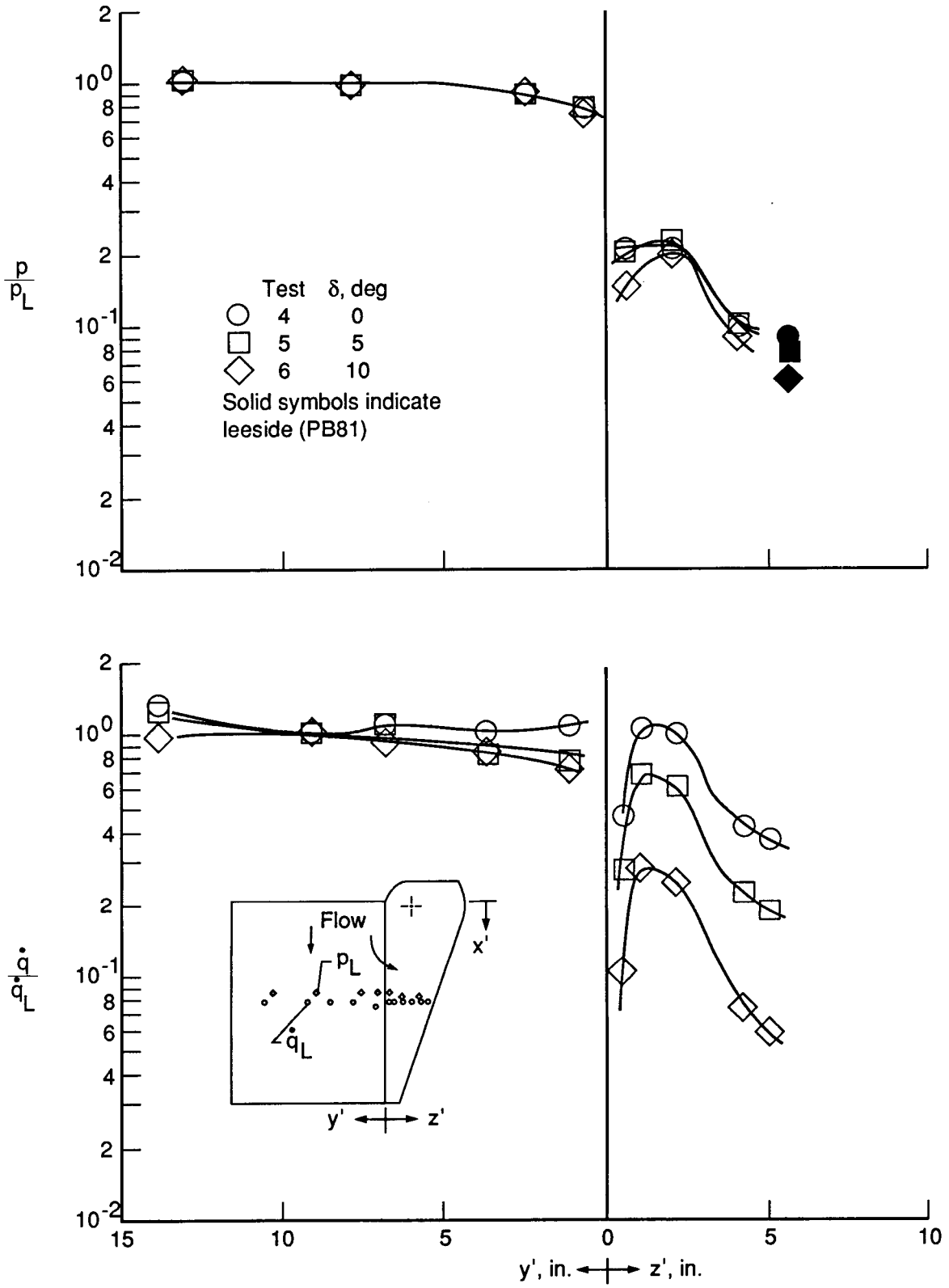

Figure 12. Lateral-pressure and heating-rate distributions at midchord around elevon at various deflection angles. $\alpha = 5°$; blunt leading edge without flow trips; $W = 2$ in.

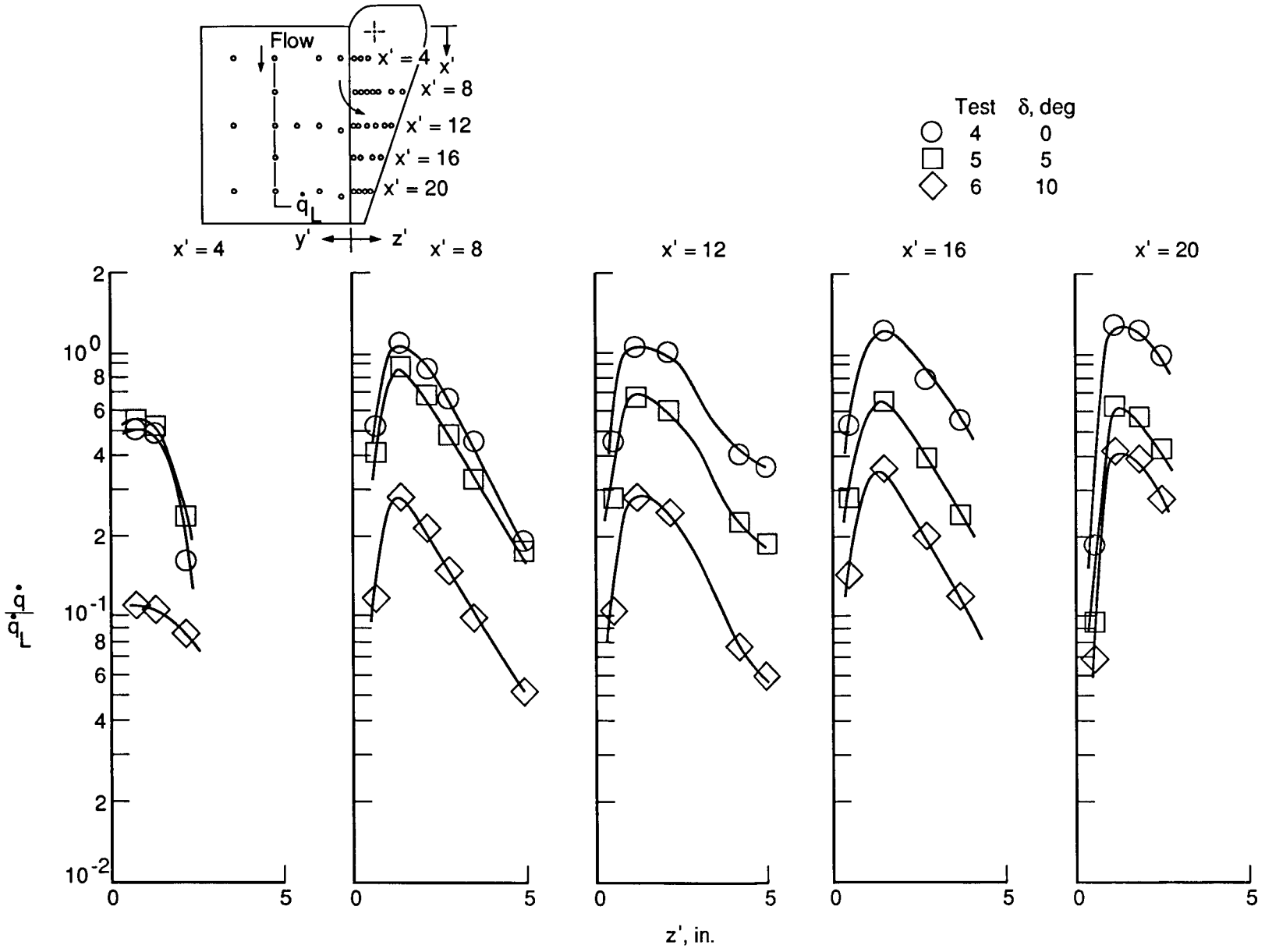

Figure 13. Elevon gap heating-rate distributions for various elevon deflection angles. $\alpha = 5°$; blunt leading edge without flow trips; $W = 2$ in.

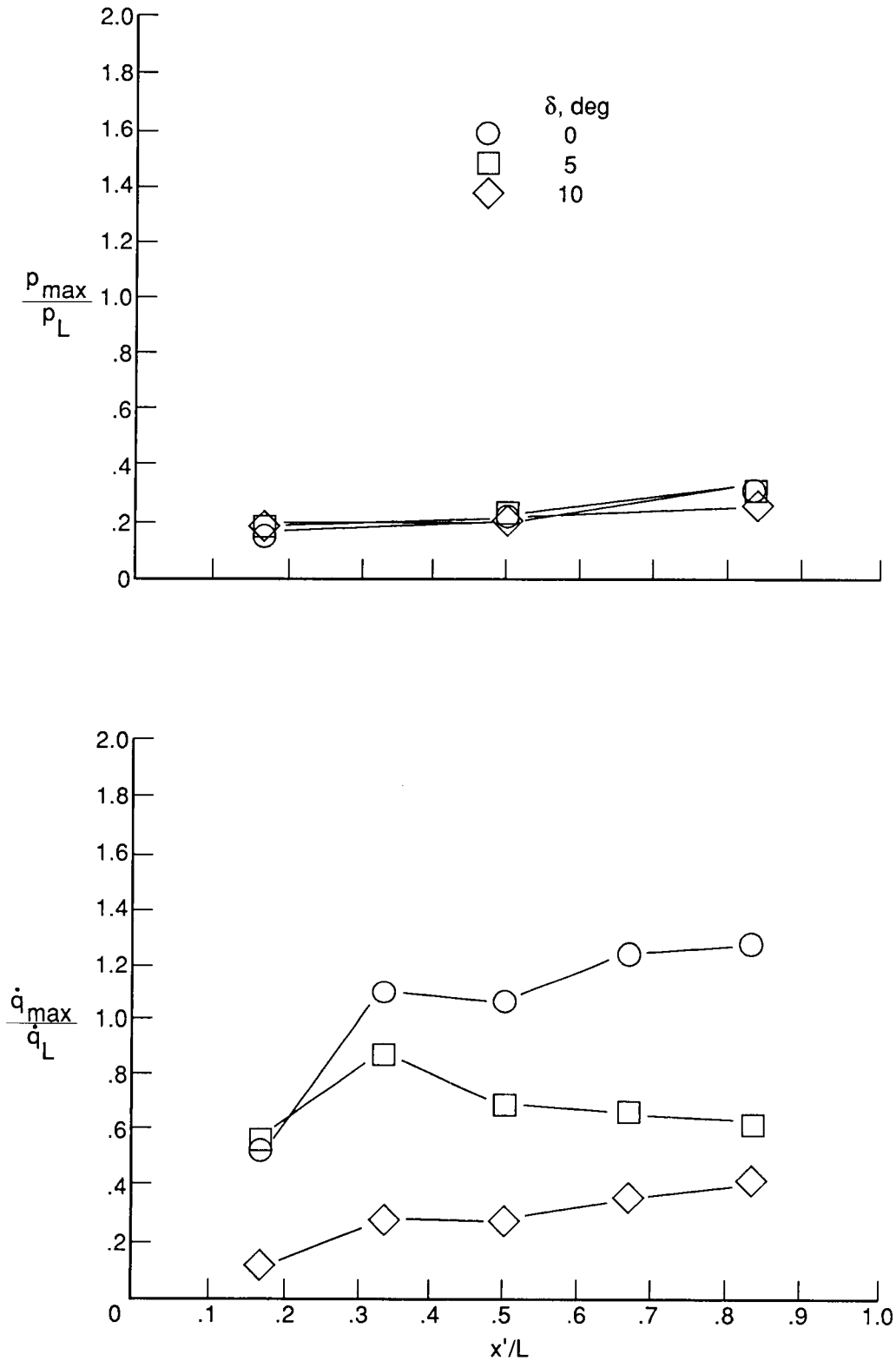

Figure 14. Longitudinal maximum gap pressure and heating rates along gap length for various deflection angles. $\alpha = 5°$; blunt leading edge without flow trips; $W = 2$ in.

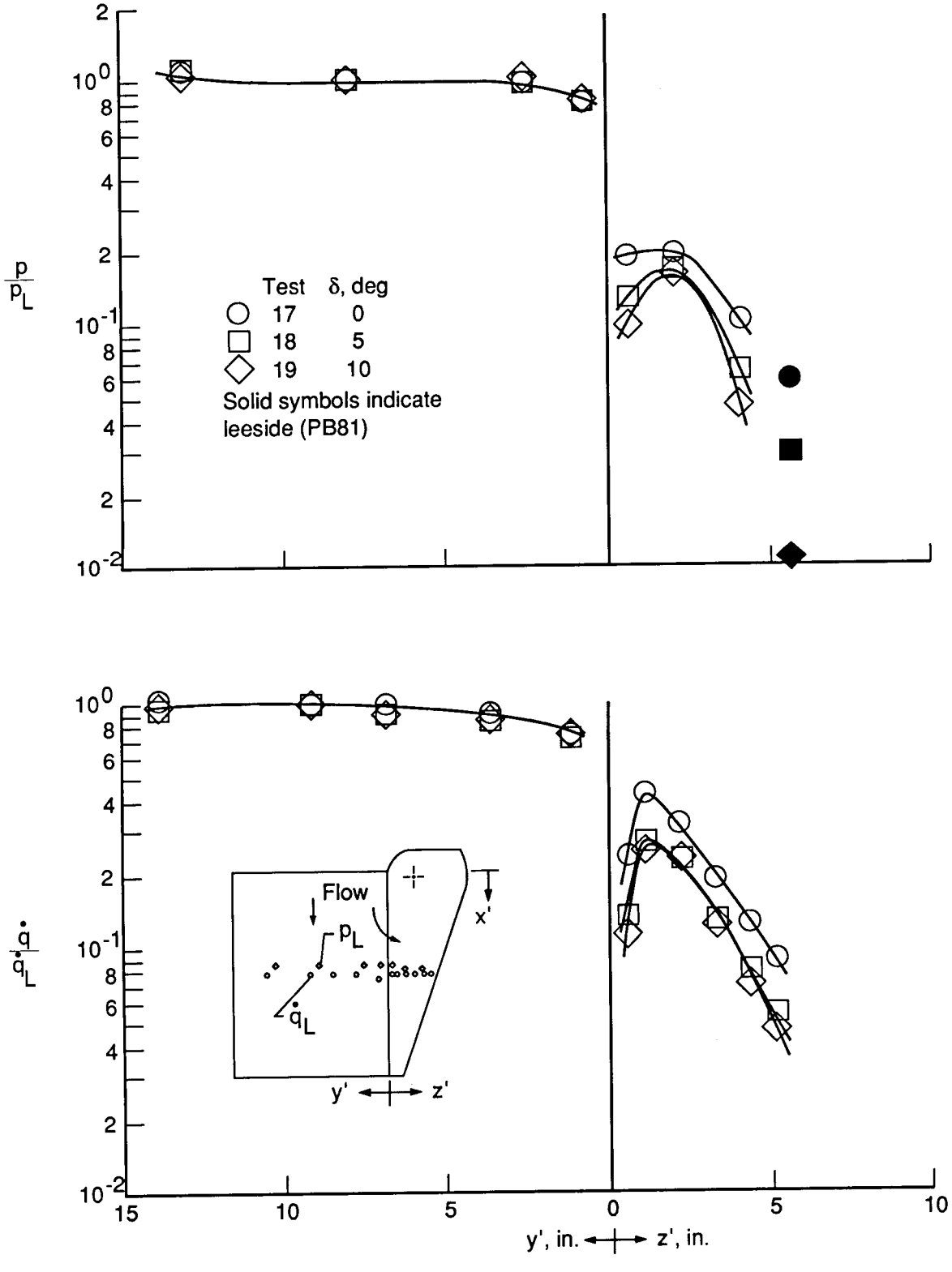

Figure 15. Lateral-pressure and heating-rate distributions at midchord around elevon at various deflection angles. $\alpha = 5°$; sharp leading edge with flow trips; $W = 2$ in.

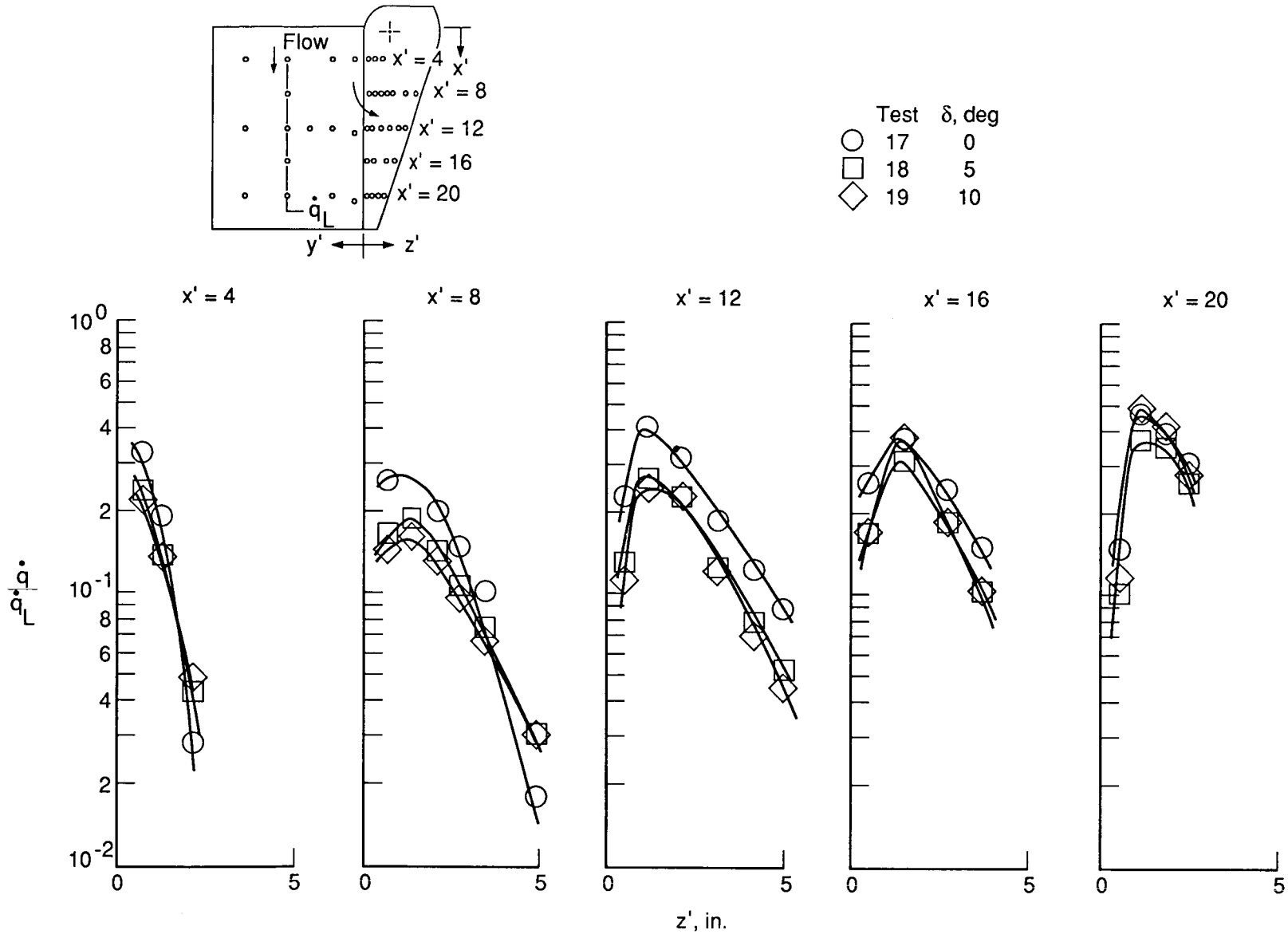

Figure 16. Elevon gap heating-rate distributions for various elevon deflection angles. $\alpha = 5°$; sharp leading edge with flow trips; $W = 2$ in.

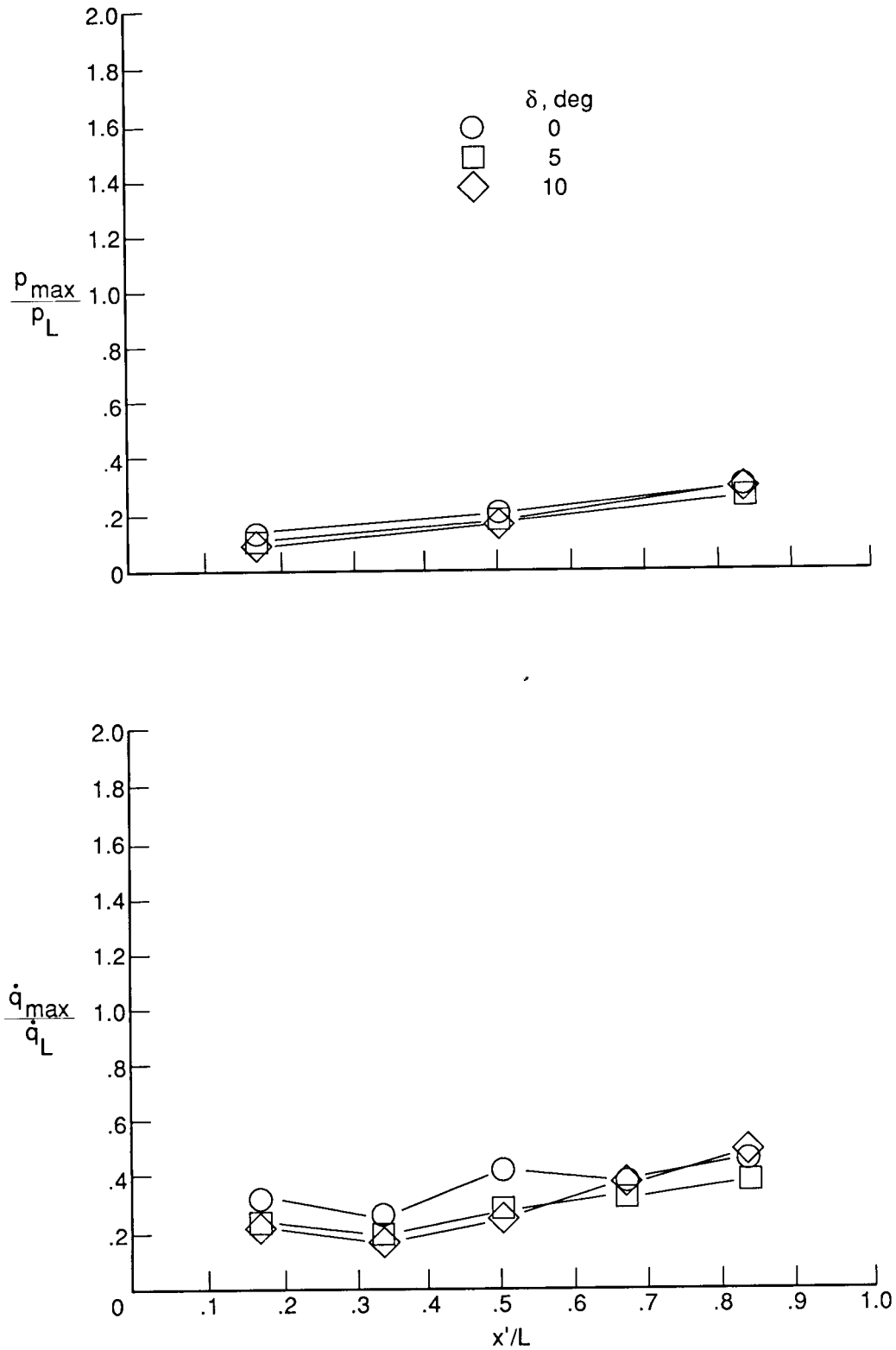

Figure 17. Longitudinal maximum gap pressure and heating rates along gap length for various deflection angles. $\alpha = 5°$; sharp leading edge with flow trips; $W = 2$ in.

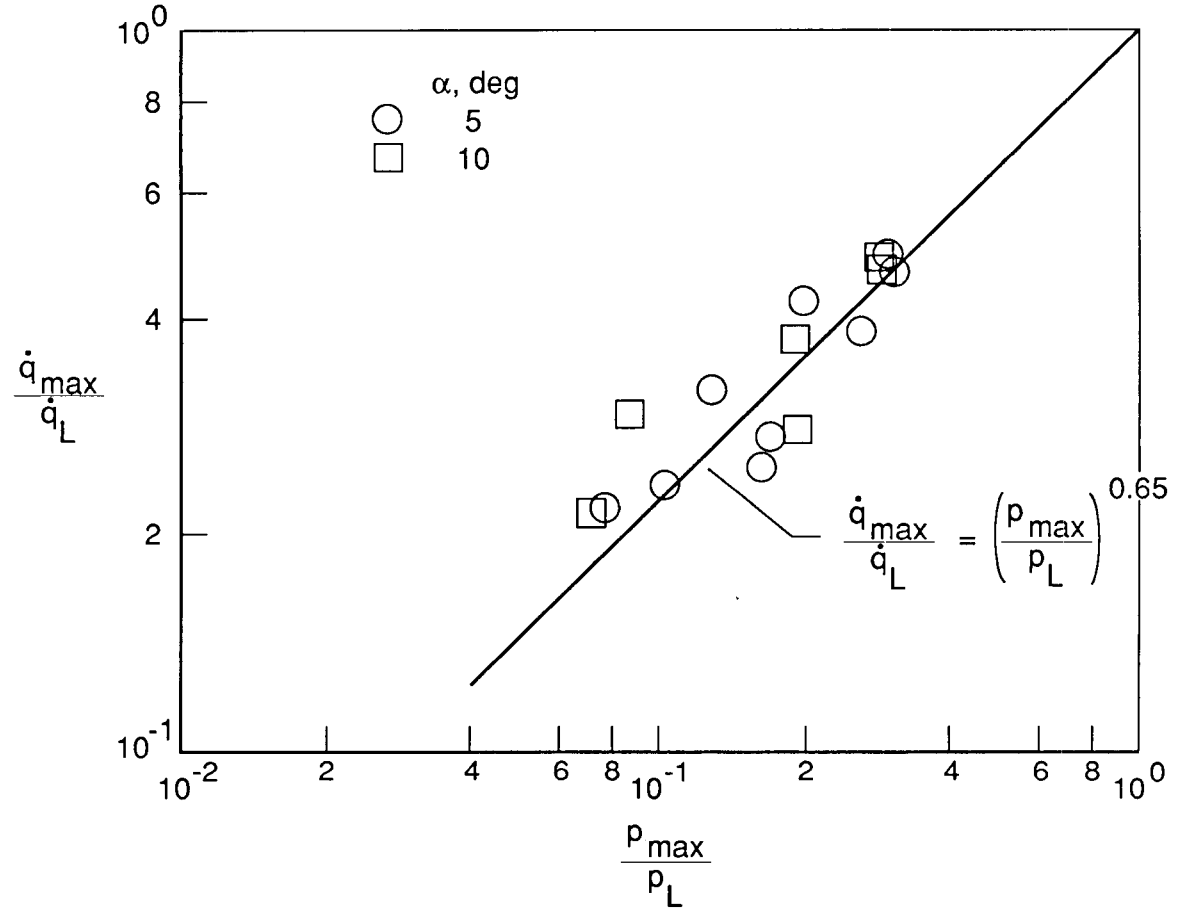

Figure 18. Correlation of maximum gap heat-transfer rate with pressure for turbulent boundary layer. $W = 2$ in.; $\delta = 0°$ to $10°$.

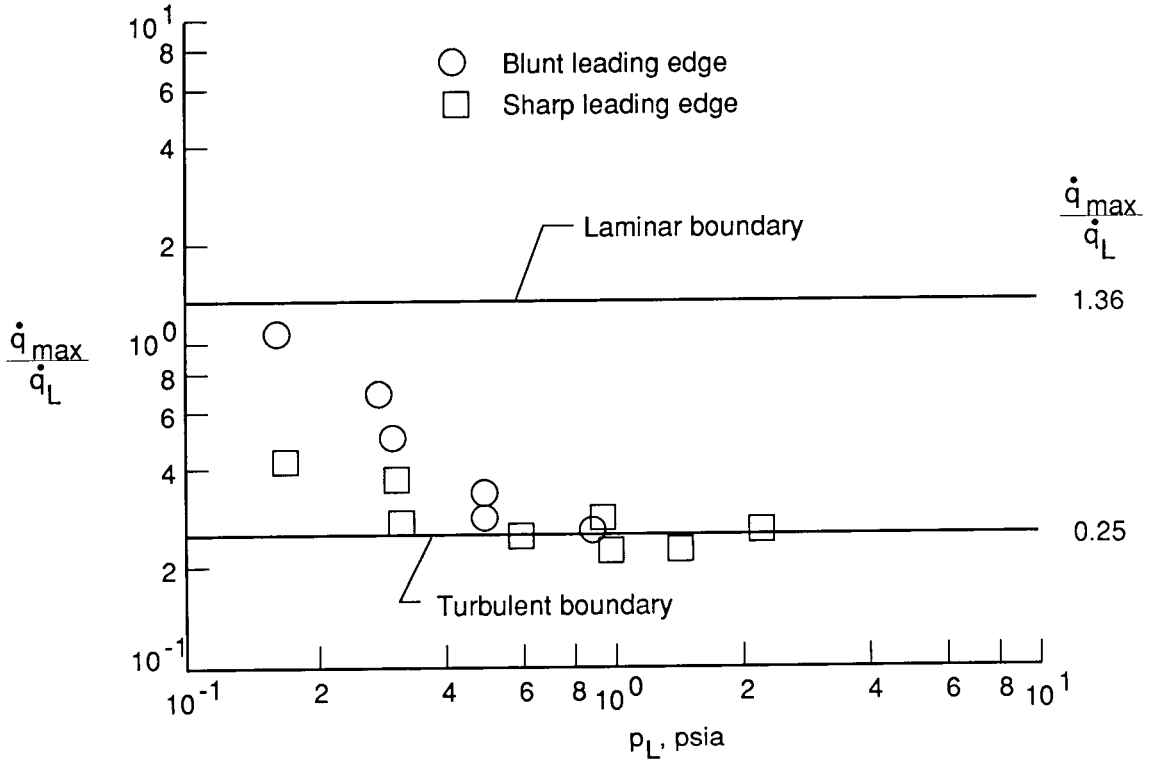

(a) Normalized heating rate.

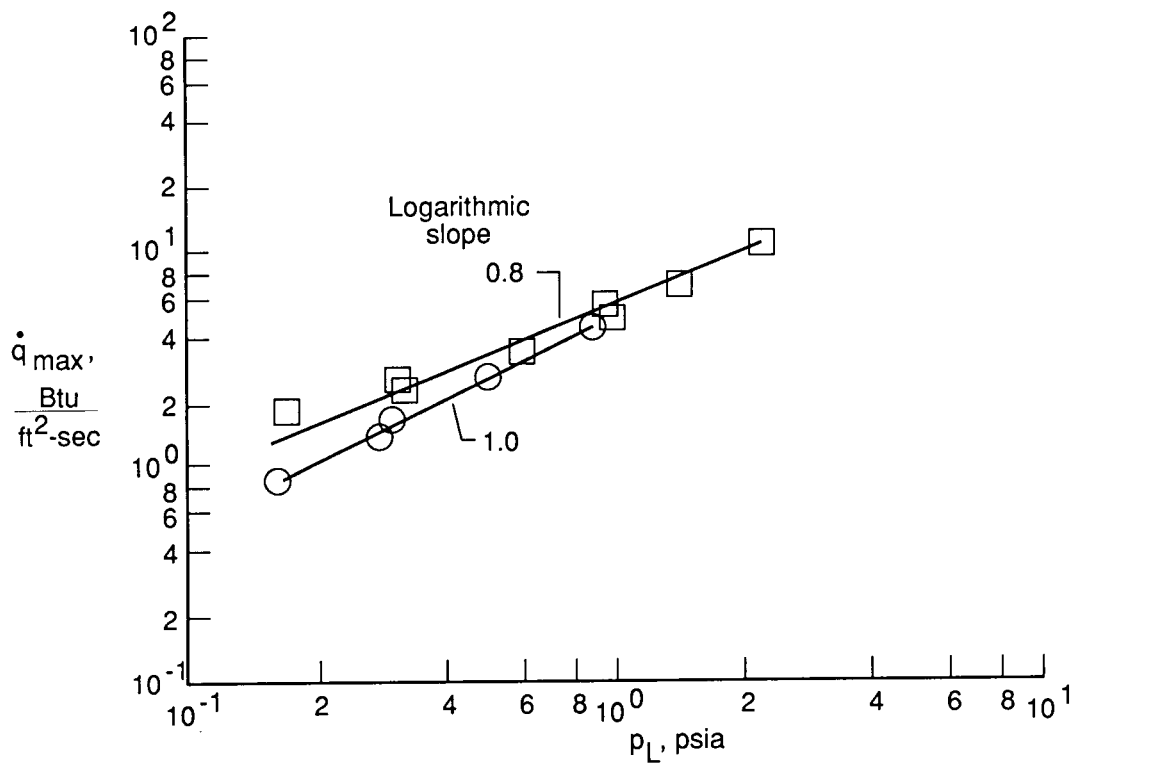

(b) Dimensional heating rate.

Figure 19. Correlations of maximum gap heating rate with windward elevon pressure. $W = 2$ in.; $R =$ (
$\alpha = 5°$ to $10°$; $\delta = 0°$ to $10°$.

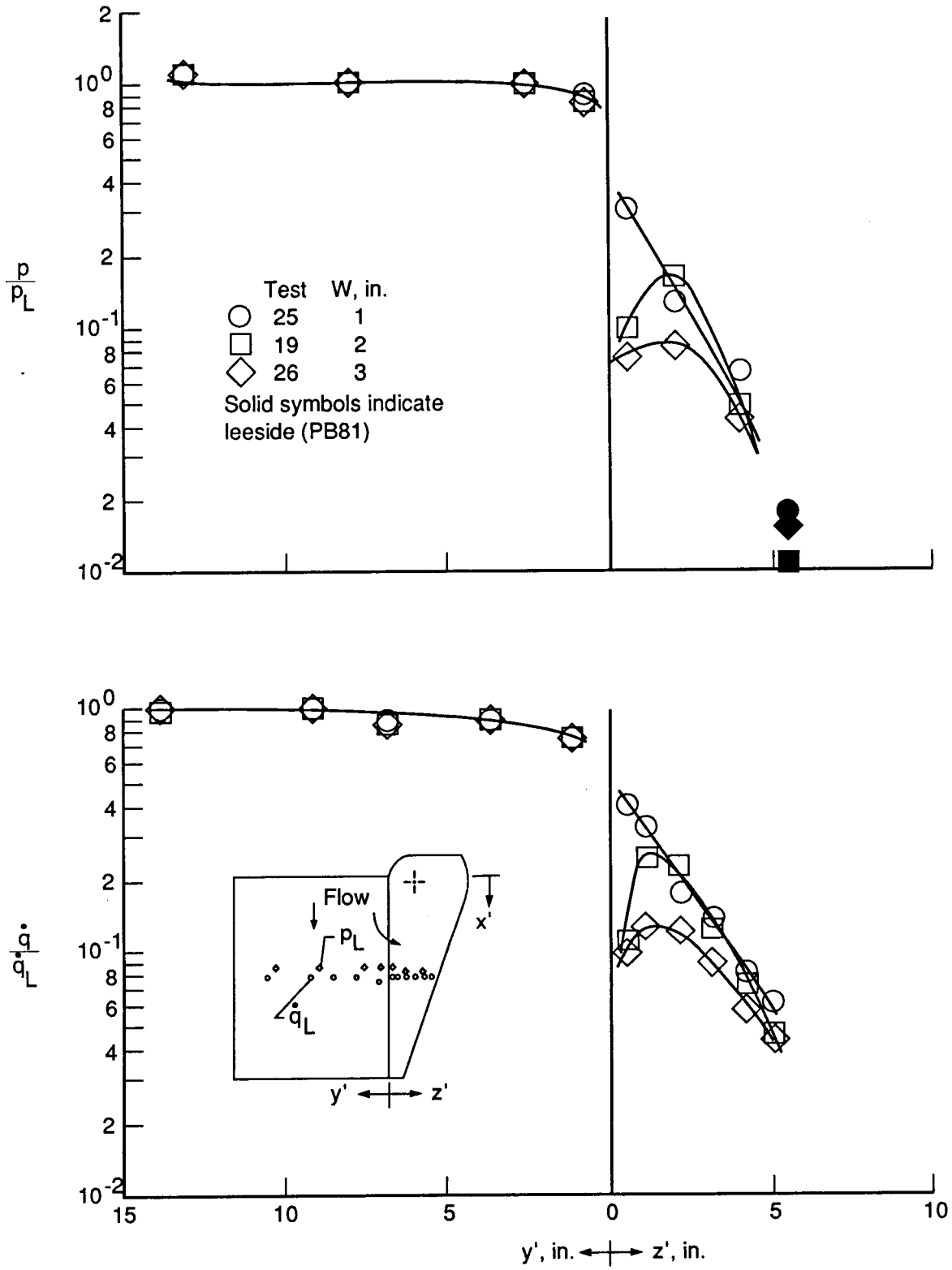

(a) Elevon edge radius = 0.

Figure 20. Lateral-pressure and heating-rate distributions at midchord around elevon for various gap widths and a sharp leading edge. $\alpha = 5°$; $\delta = 10°$.

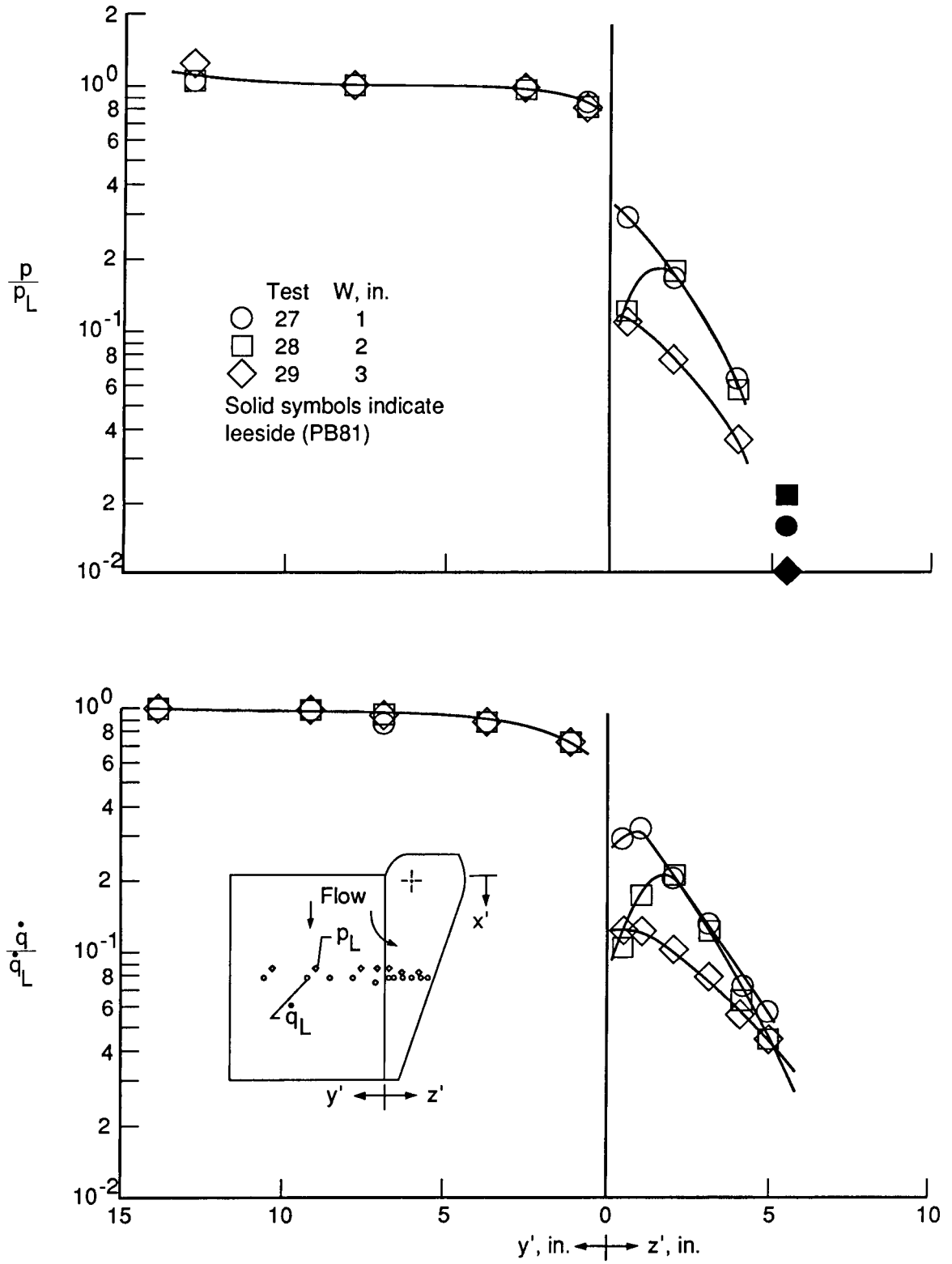

(b) Elevon edge radius = 0.25 in.

Figure 20. Concluded.

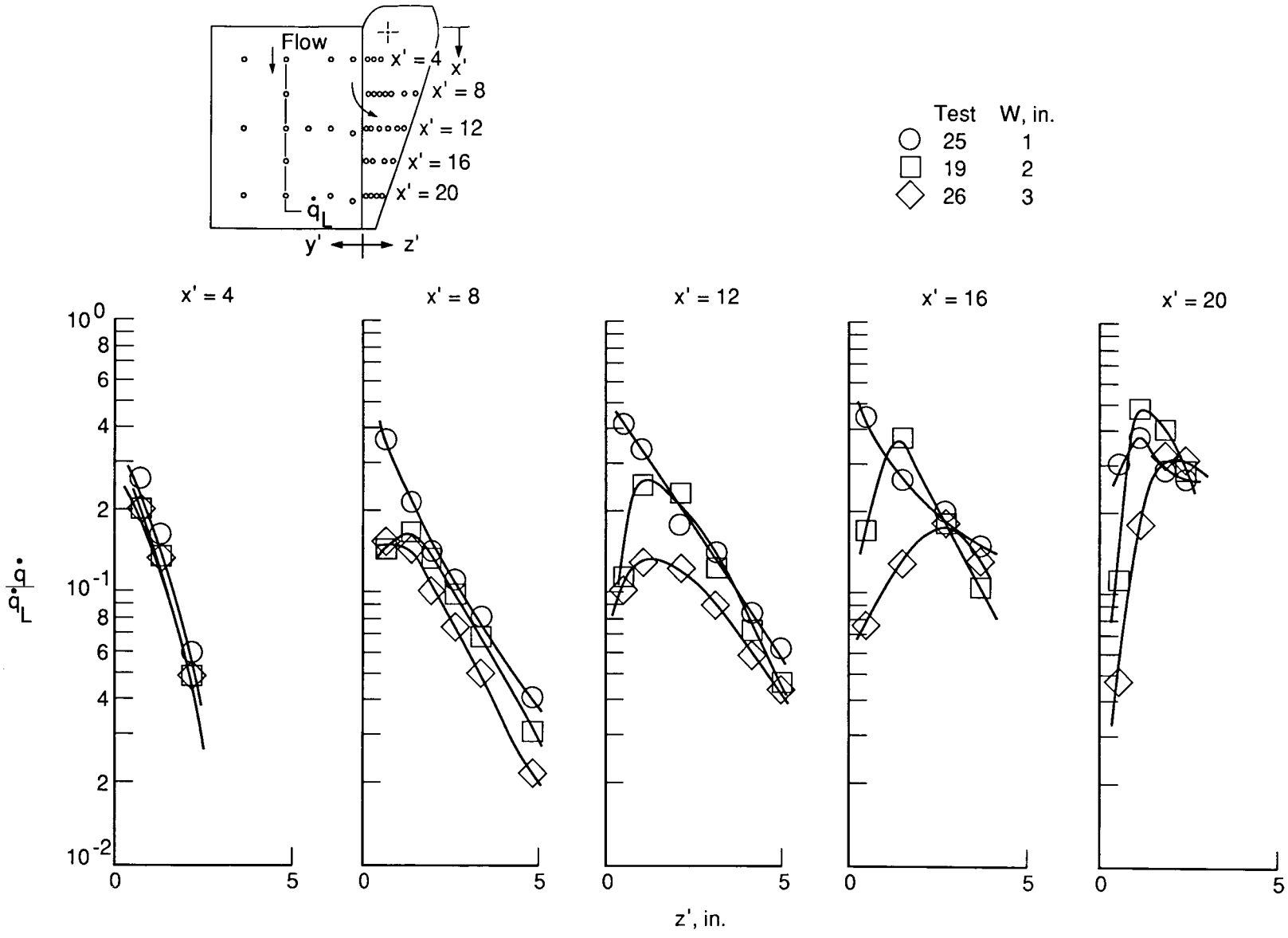

(a) Elevon edge radius = 0.

Figure 21. Elevon gap heating rate distributions for various gap widths and a sharp leading edge. $\alpha = 5°$; $\delta = 10°$.

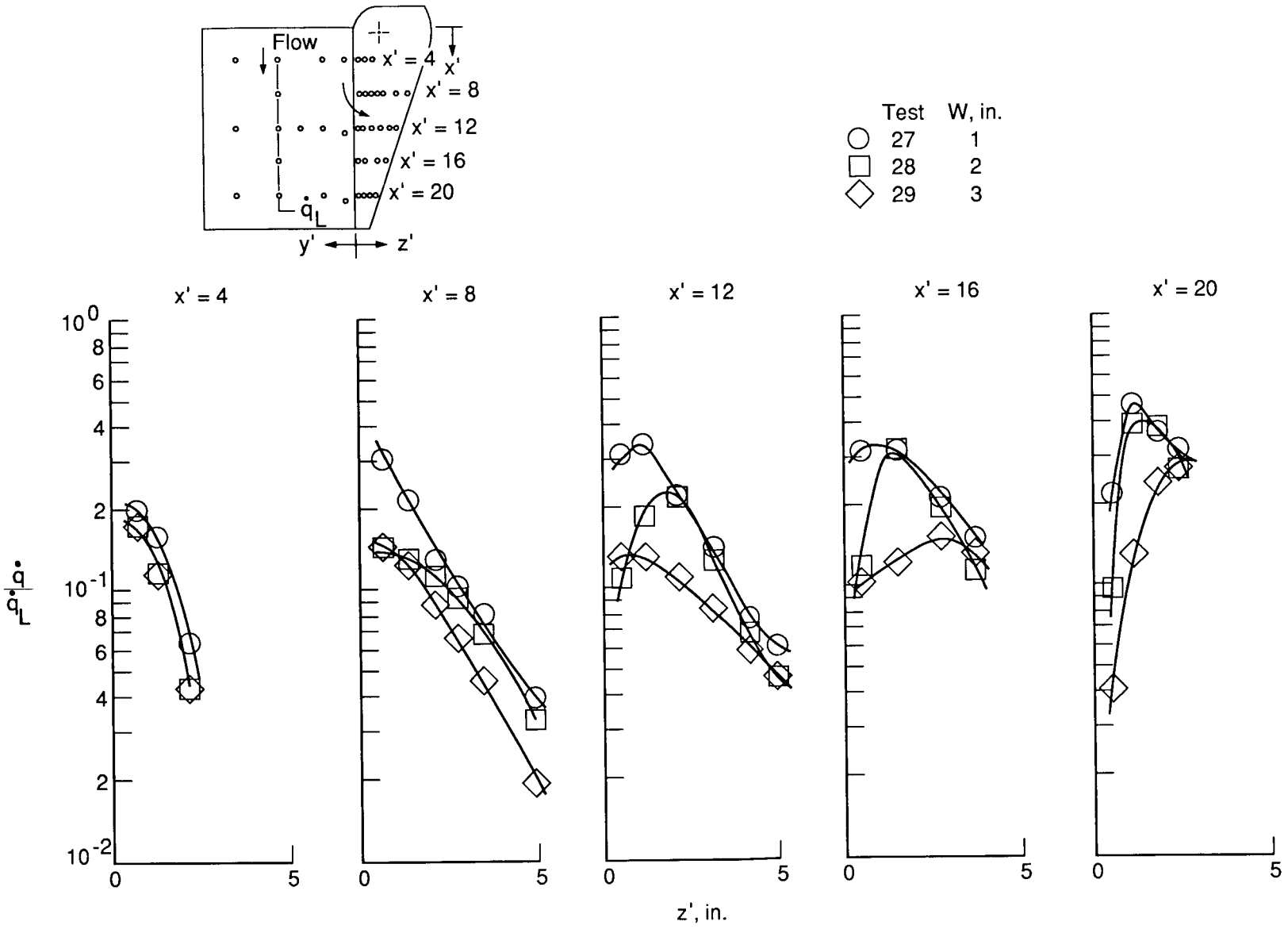

(b) Elevon edge radius = 0.25 in.

Figure 21. Concluded.

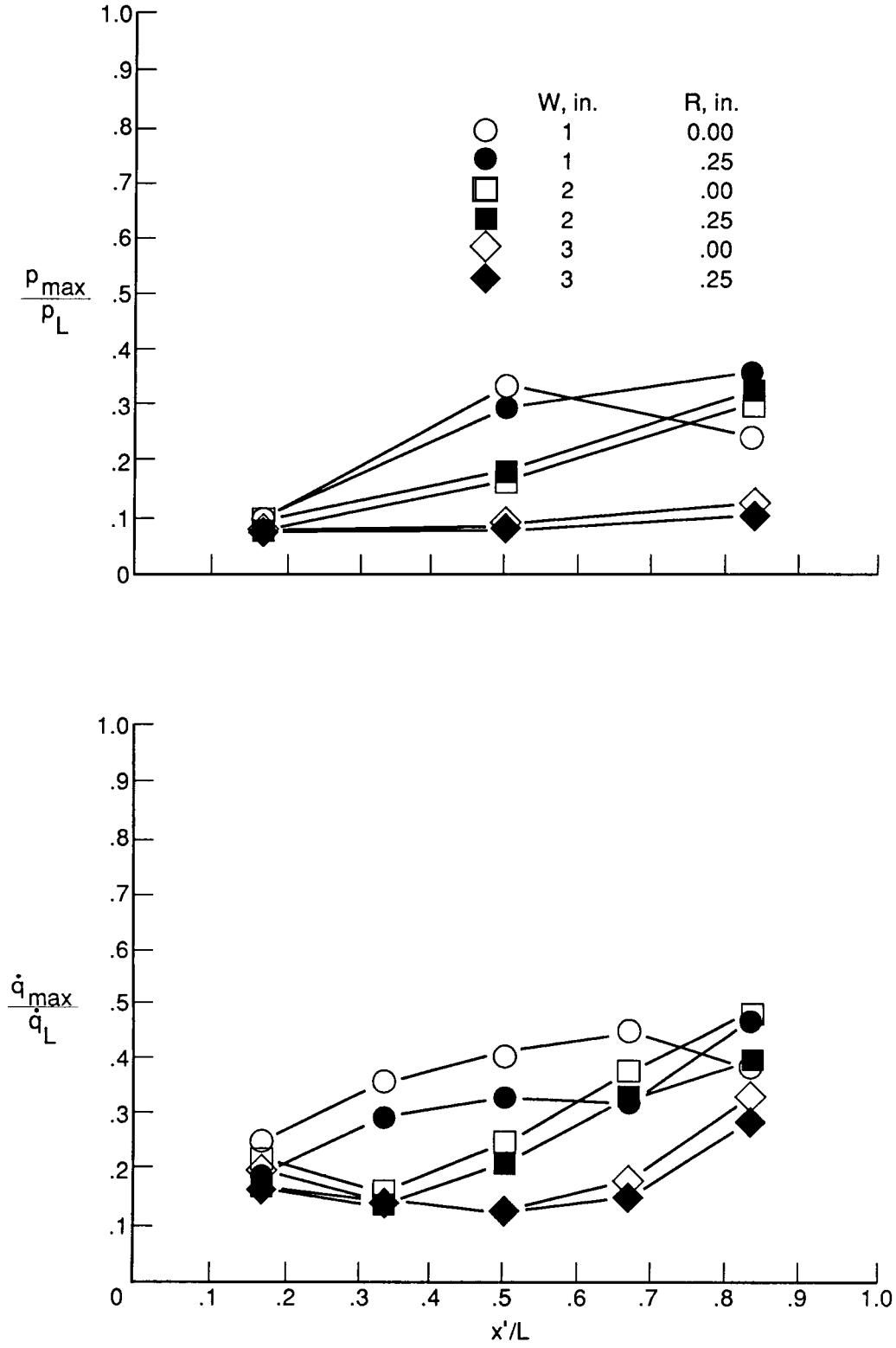

Figure 22. Longitudinal maximum gap pressure and heating rates along gap length for various deflection angles and edge radii. $\alpha = 5°$; $\delta = 10°$.

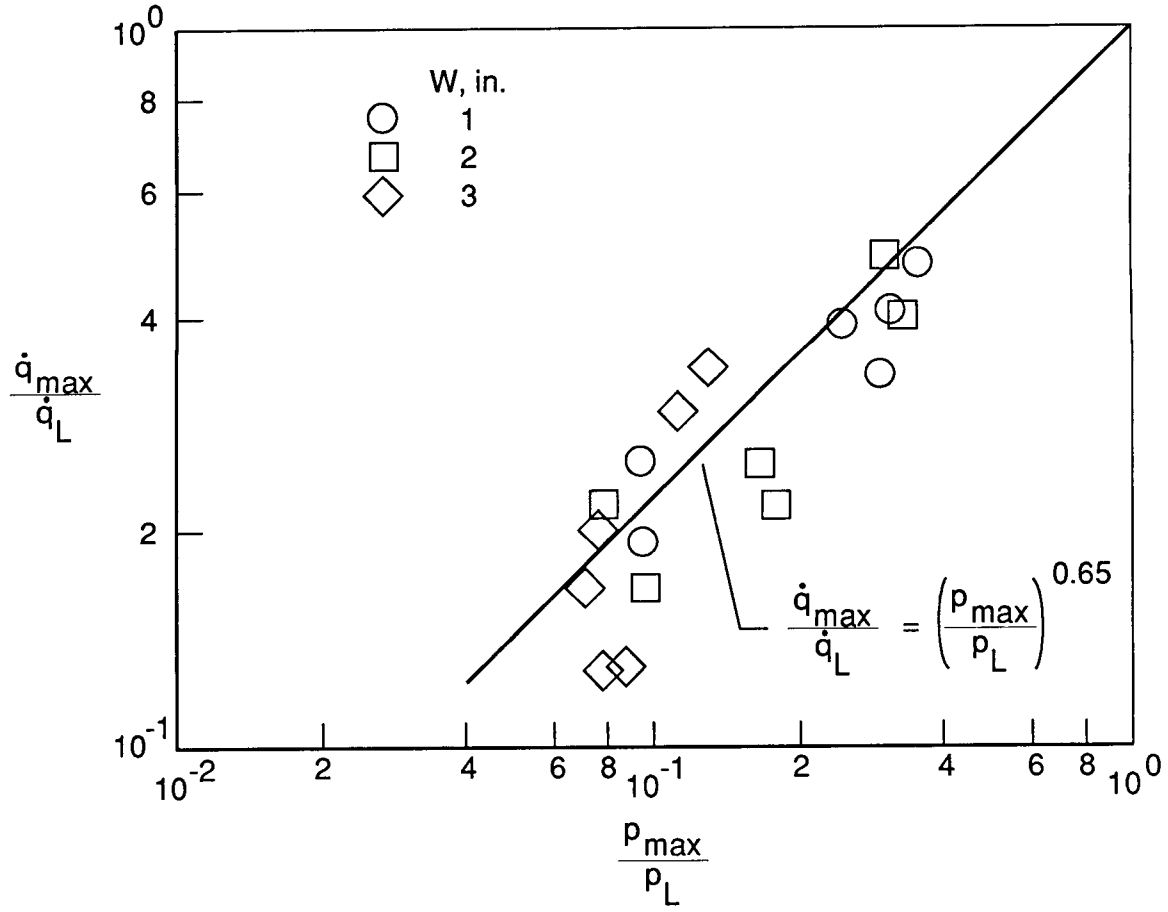

Figure 23. Correlation of maximum gap heat-transfer rate with pressure for various gap widths. $\alpha = 5°$ $\delta = 10°$; $R = 0$ and 0.25 in.

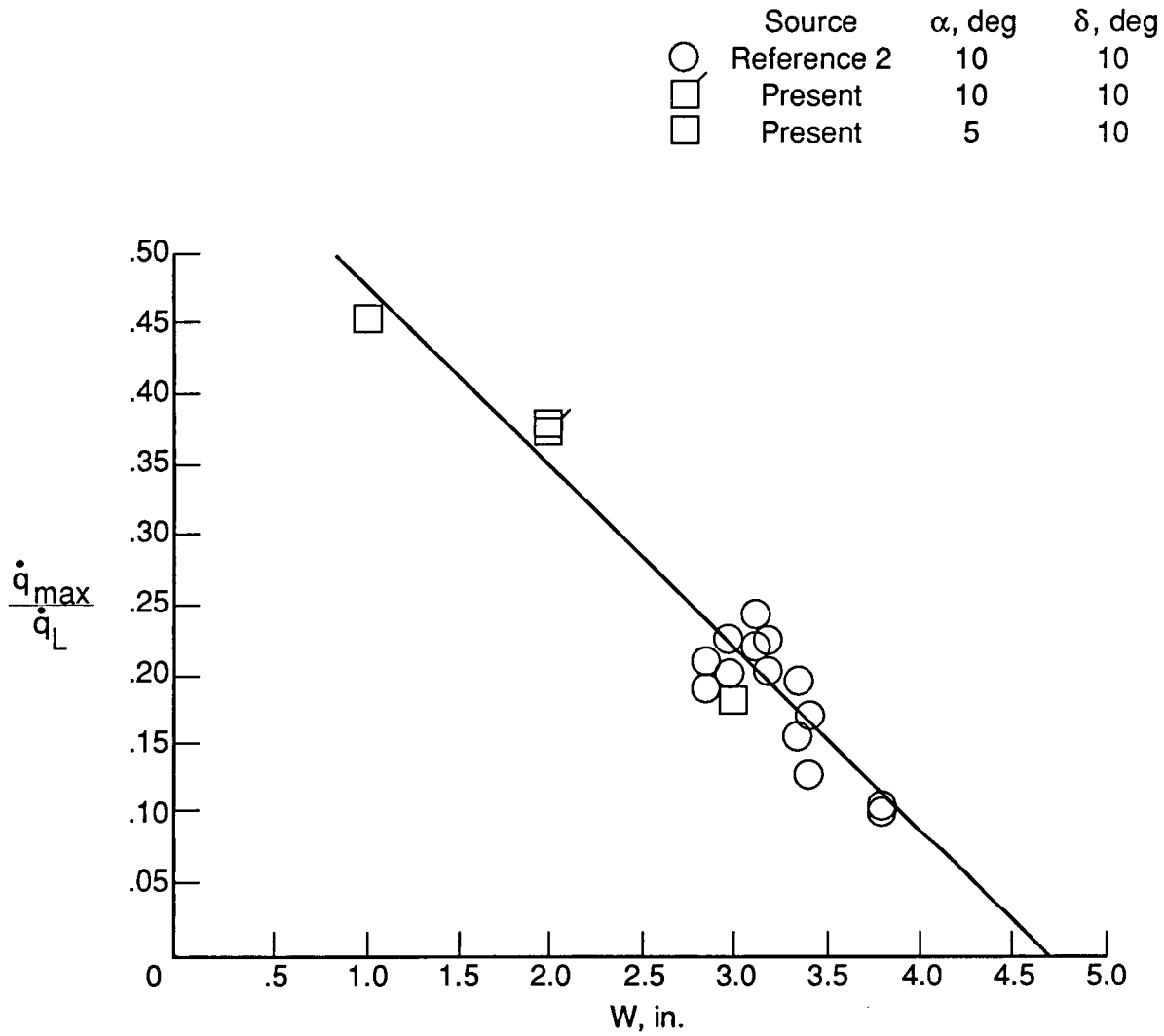

Figure 24. Effect of gap width on maximum gap heating rate at $x'/L = 0.67$.

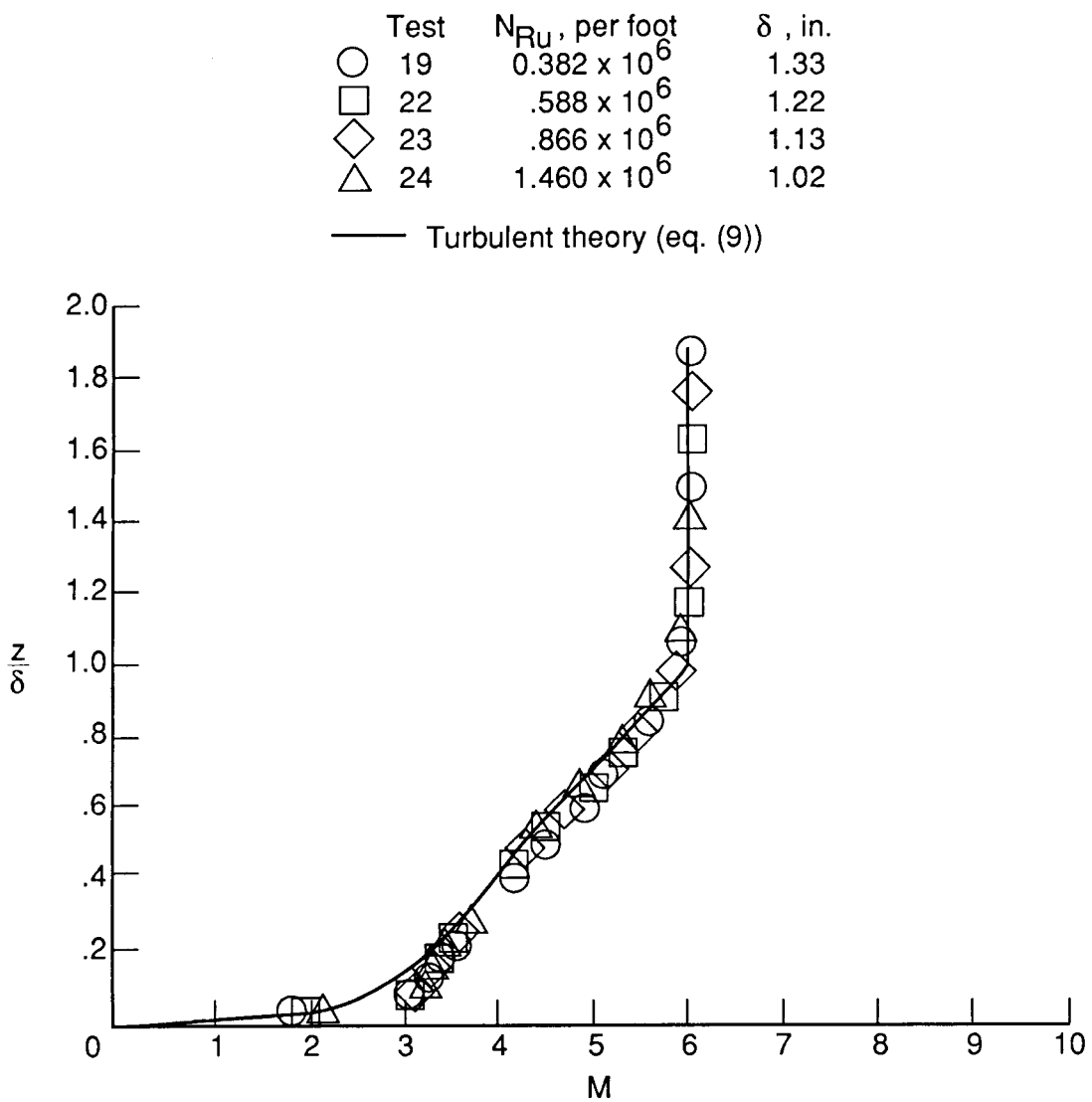

Figure 25. Boundary-layer Mach number profiles with sharp leading edge and flow trips at $\alpha = 5°$ for various free-stream Reynolds numbers.

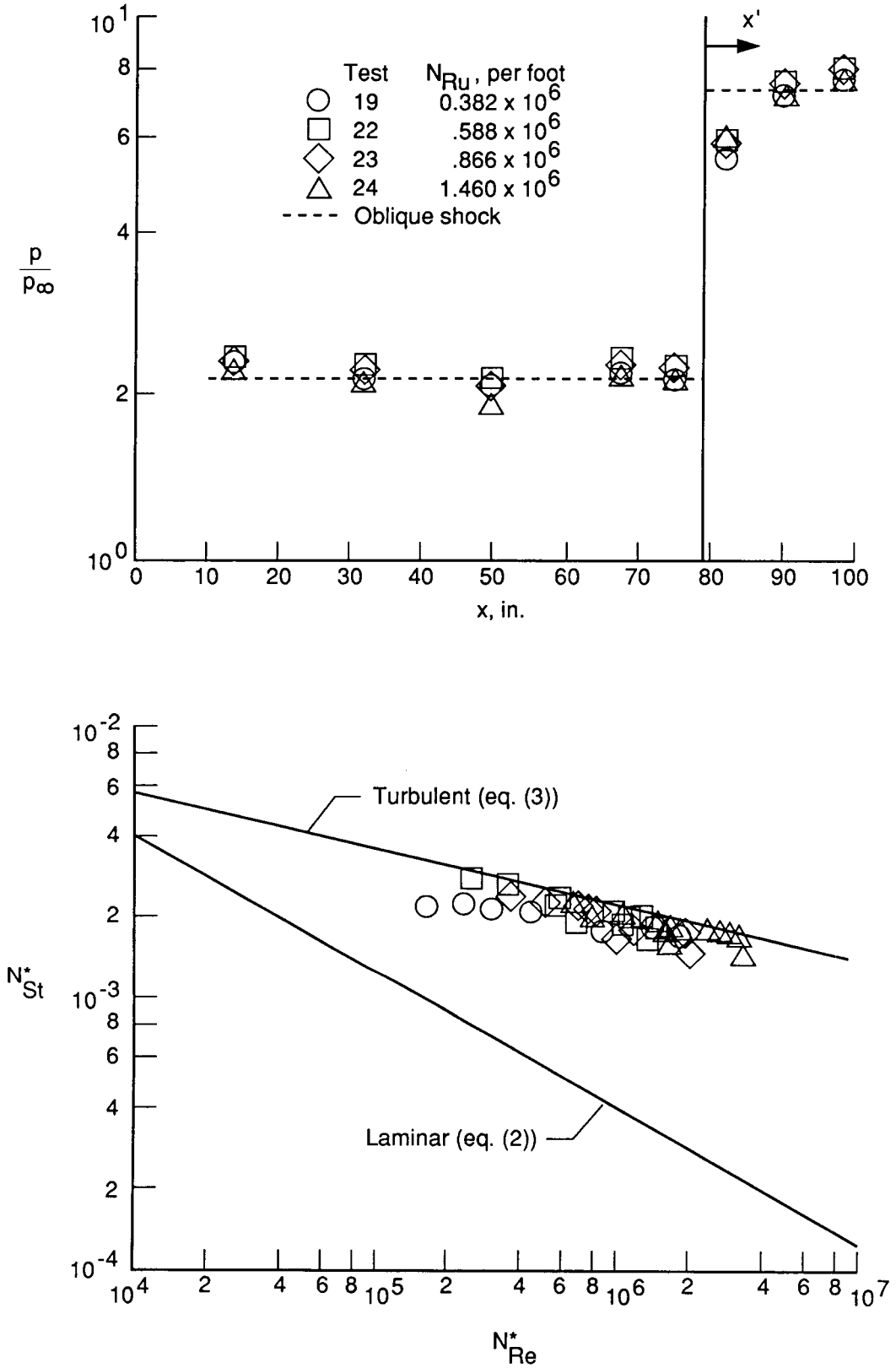

Figure 26. Longitudinal pressure and heat-transfer distributions for sharp leading edge at various Reynolds numbers. $\alpha = 5°; \delta = 10°$.

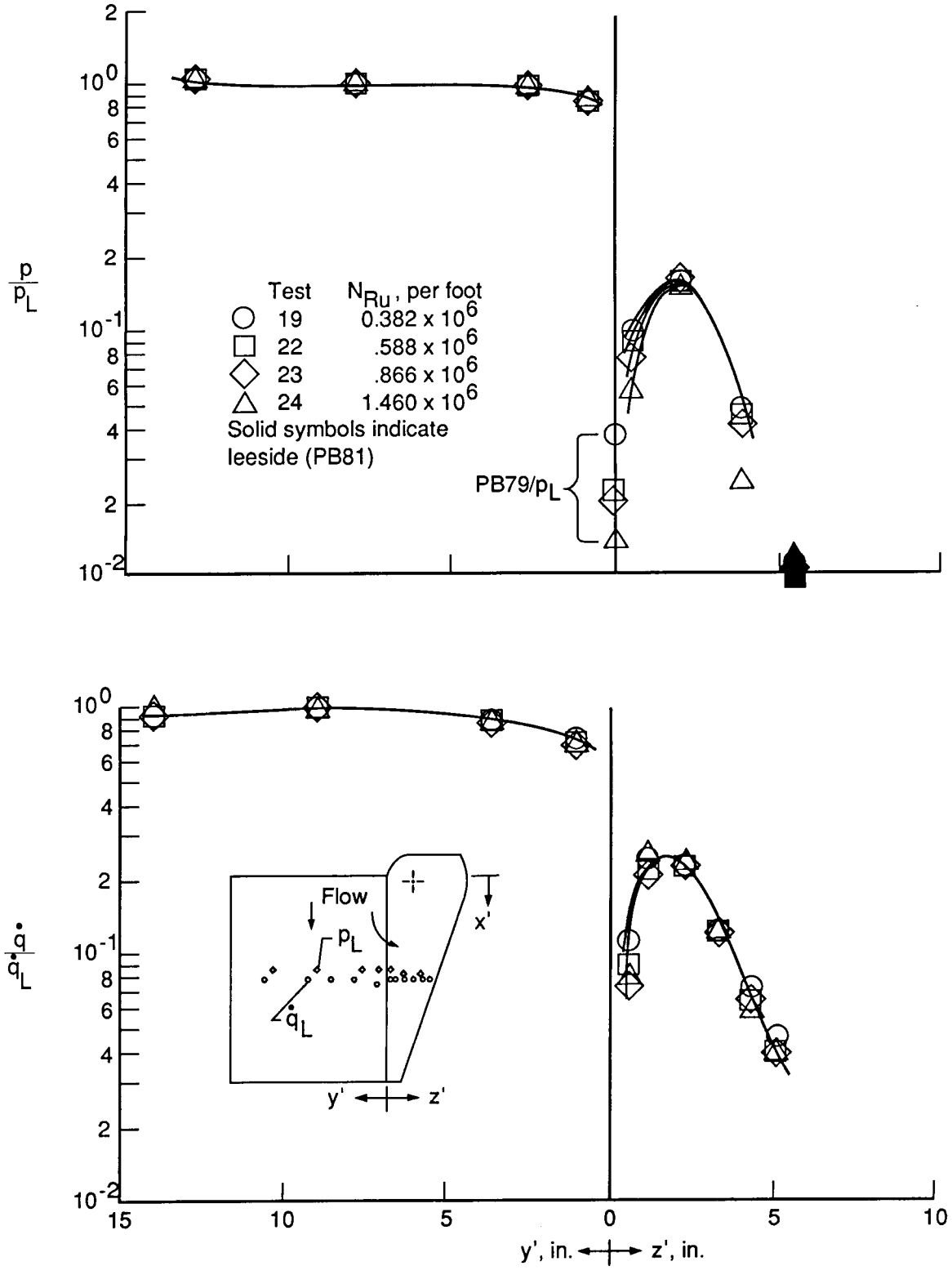

Figure 27. Lateral-pressure and heating-rate distributions at midchord around elevon for various free-stream Reynolds numbers. $\alpha = 5°; \delta = 10°$.

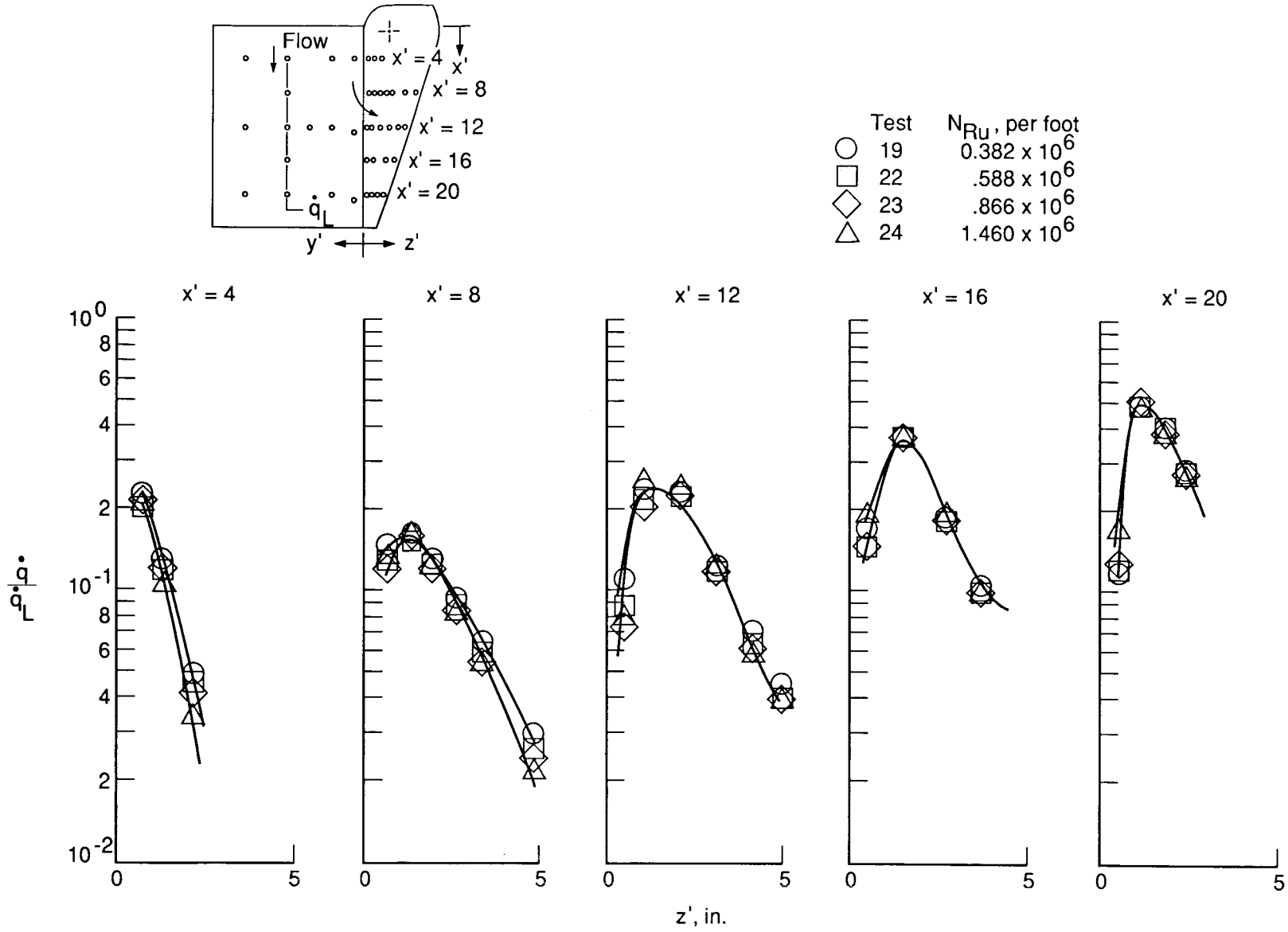

Figure 28. Elevon gap heating-rate distributions for various free-stream Reynolds numbers. $\alpha = 5°$; $\delta = 10°$; $W = 1$ in.

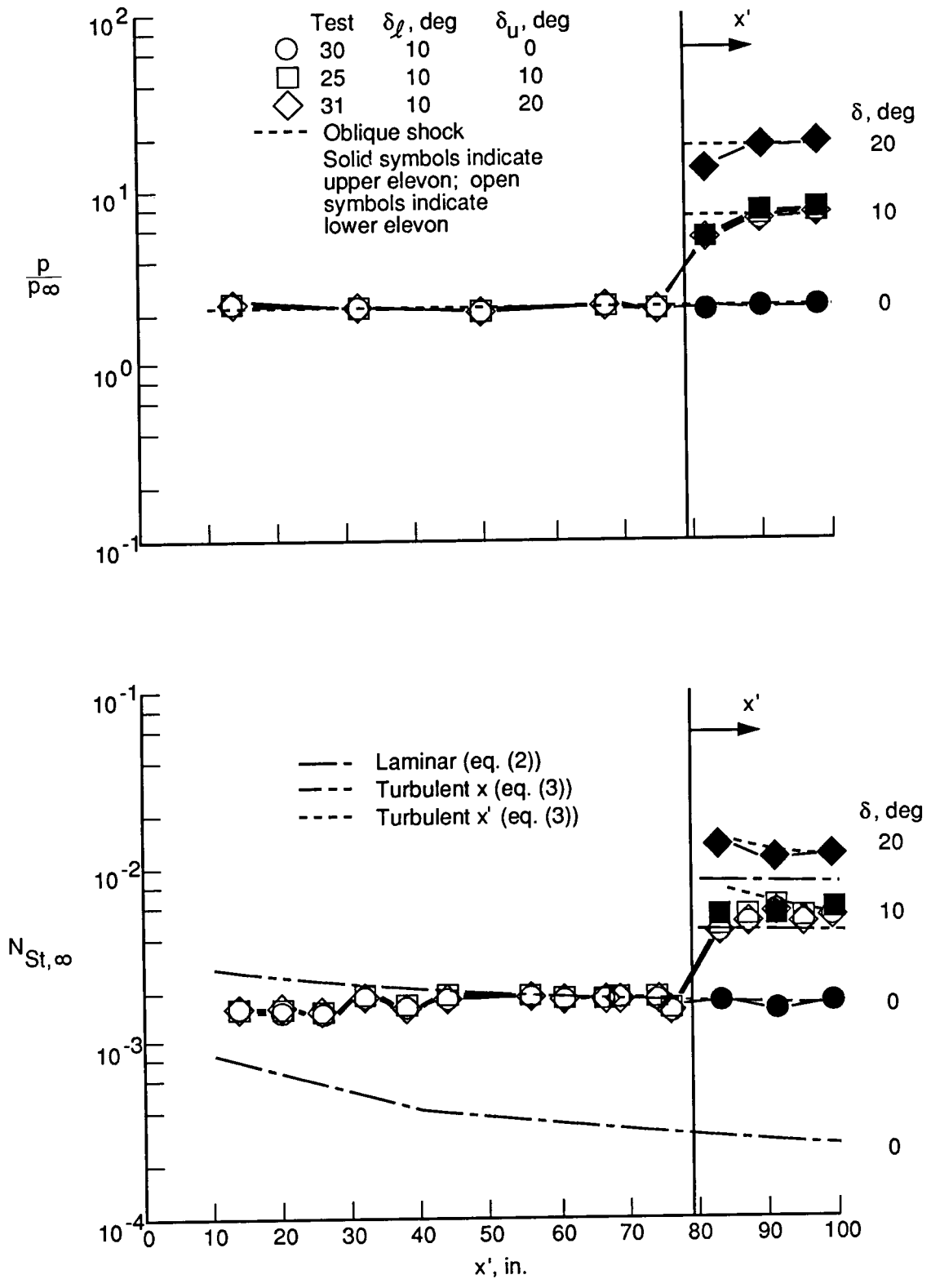

Figure 29. Longitudinal-pressure and heating-rate distributions with differential elevon angles. $\alpha = 5°$; $W = 1$ in.

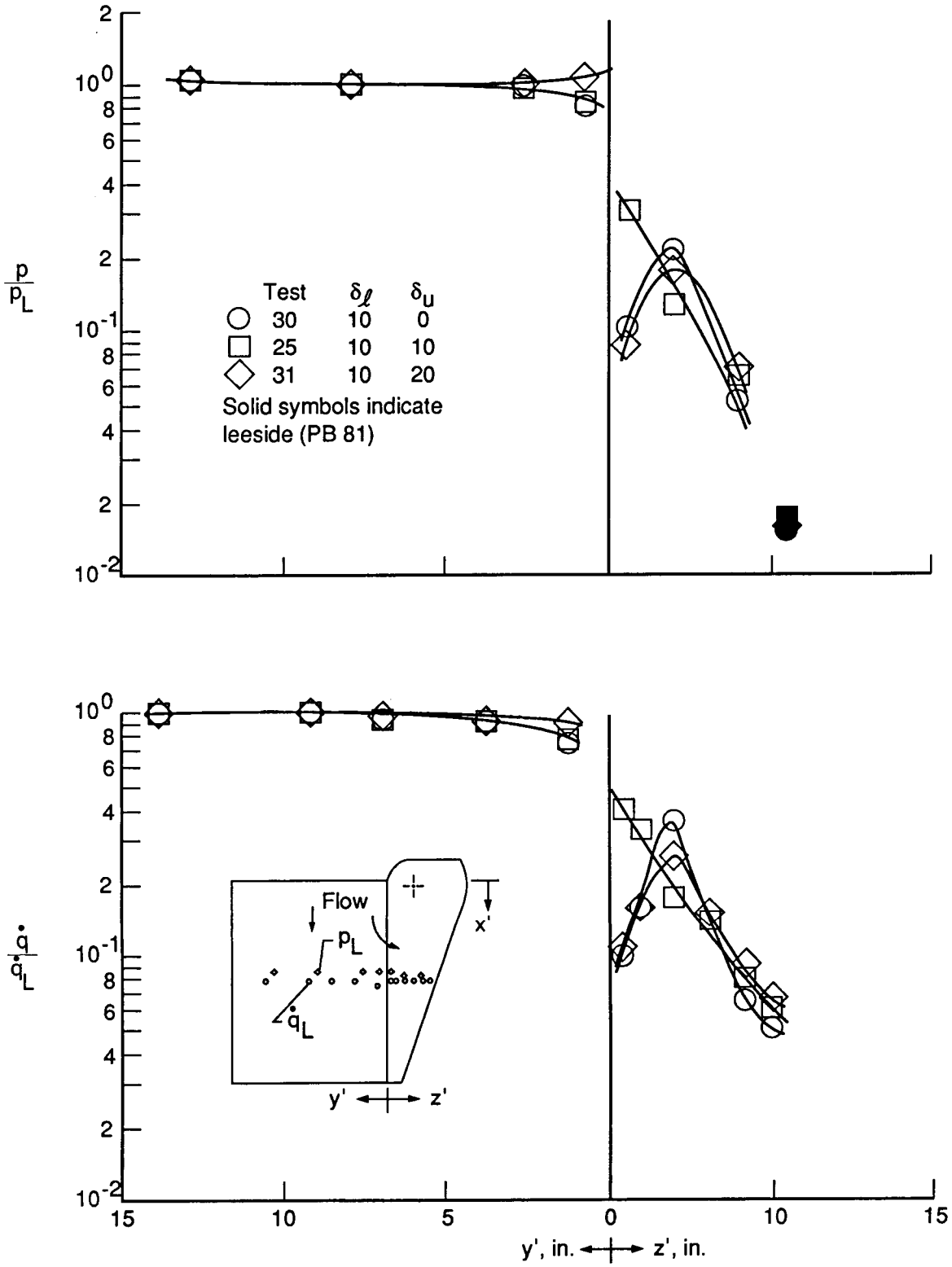

Figure 30. Lateral-pressure and heating-rate distributions at midchord around elevon with differential deflection angles. $\alpha = 5°; \delta = 10°; W = 1$ in.

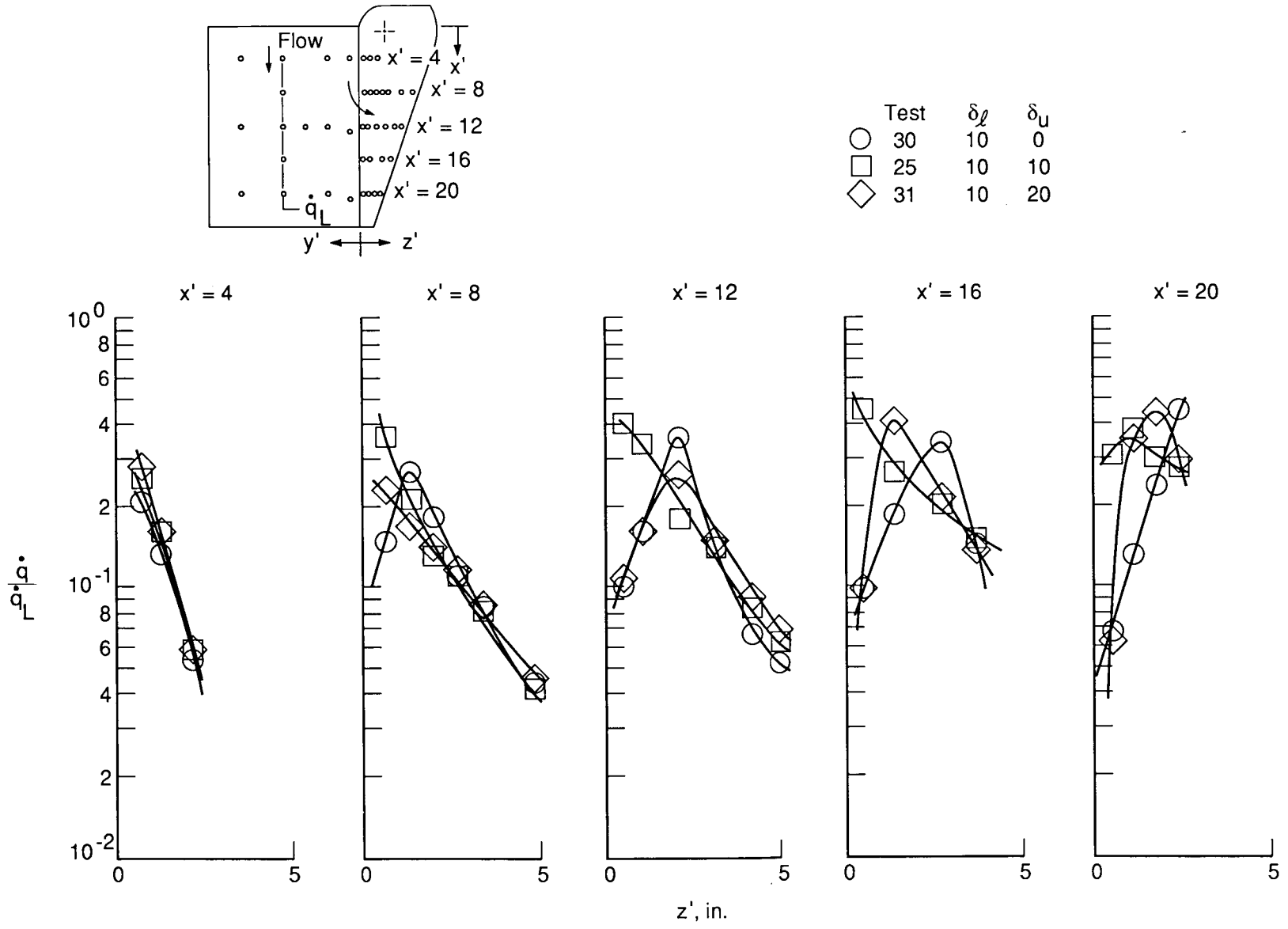

Figure 31. Elevon gap heating-rate distributions for differential elevon deflection angles. $\alpha = 5°; W = 1$ in.

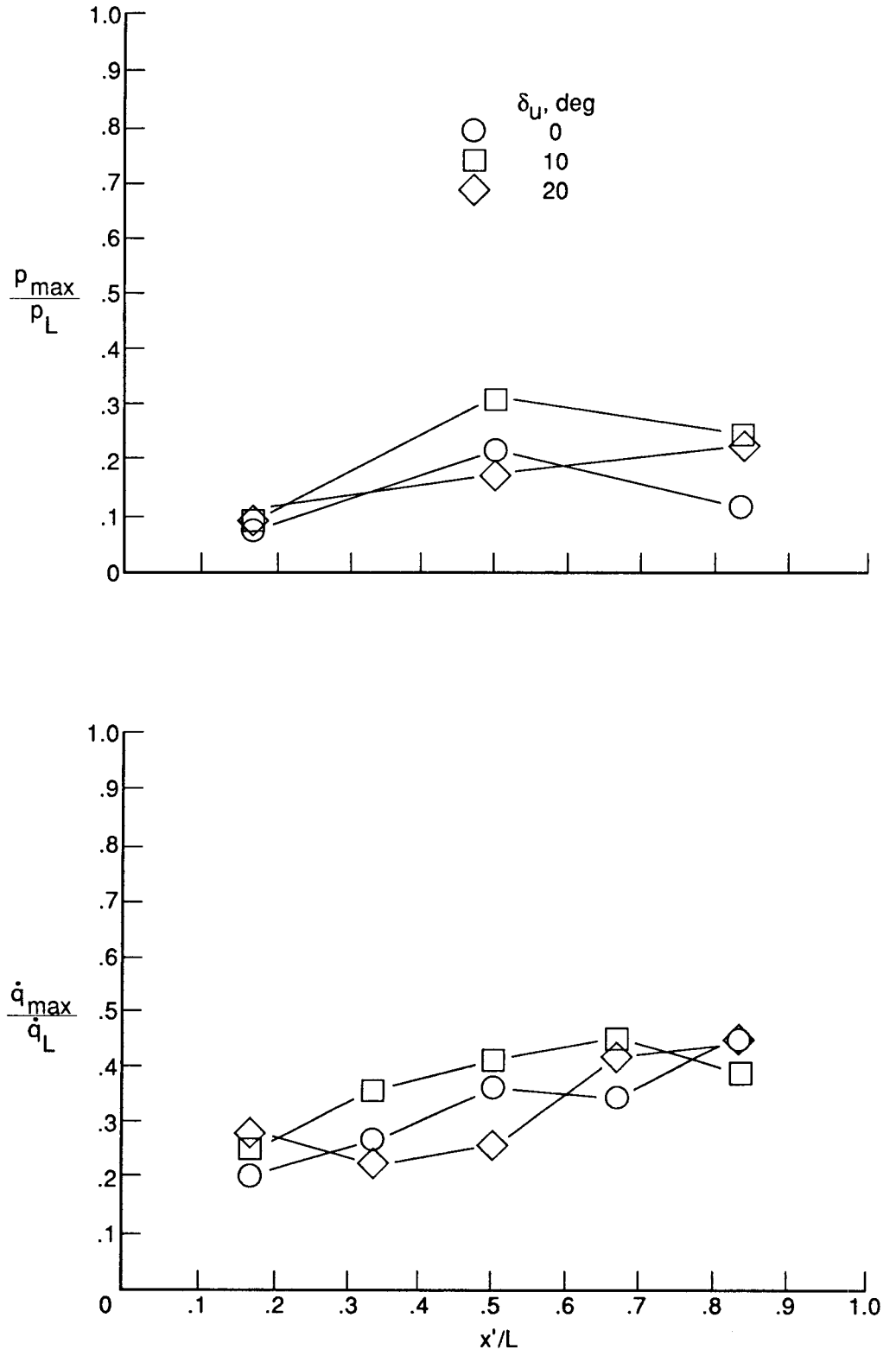

Figure 32. Longitudinal maximum gap pressure and heating rates along gap length on lower elevon for differential elevon deflection angles. $W = 1$ in.; $\alpha = 5°$; $\delta_\ell = 10°$.

NASA
National Aeronautics and Space Administration

Report Documentation Page

1. Report No.	2. Government Accession No.	3. Recipient's Catalog No.
NASA TP-2855		

4. Title and Subtitle	5. Report Date
Aerodynamic Pressures and Heating Rates on Surfaces Between Split Elevons at Mach 6.6	December 1988
	6. Performing Organization Code
7. Author(s)	8. Performing Organization Report No.
L. Roane Hunt	L-16460
9. Performing Organization Name and Address	10. Work Unit No.
NASA Langley Research Center Hampton, VA 23665-5225	506-40-21-01
	11. Contract or Grant No.
12. Sponsoring Agency Name and Address	13. Type of Report and Period Covered
National Aeronautics and Space Administration Washington, DC 20546-0001	Technical Paper
	14. Sponsoring Agency Code

15. Supplementary Notes

16. Abstract

An aerothermal study was performed in the Langley 8-Foot High-Temperature Tunnel at a Mach number of 6.6 to define the pressures and heating rates on the surfaces between split elevons similar to those used on the Space Shuttle. Tests were performed with both laminar and turbulent boundary layers on the wing surface upstream of the elevons. The flow in the chordwise gap between the elevons was characterized by flow separation at the gap entrance and flow reattachment at a depth inversely proportional to the gap width. The gap pressure and heating rate increased significantly with a decrease in elevon gap width, and the maximum gap heating rate was proportional to the maximum gap pressure. Correlation of the present results indicate that the gap heating was directly proportional to the elevon windward surface pressure and was not dependent upon whether the boundary layer on the windward elevon surface was laminar or turbulent.

17. Key Words (Suggested by Authors(s))	18. Distribution Statement
Hypersonic flight Pressure and heating-rate distributions Laminar and turbulent boundary layers Split elevons Chordwise gaps	Unclassified—Unlimited Subject Category 34

19. Security Classif.(of this report)	20. Security Classif.(of this page)	21. No. of Pages	22. Price
Unclassified	Unclassified	84	A05

For sale by the National Technical Information Service, Springfield, Virginia 22161-2171